



**US Army Corps
of Engineers**
Waterways Experiment
Station

AD-A271 540



Technical Report SL-93-16
September 1993

②

Two-Dimensional Finite Element Analysis of Porous Media at Multikilobar Stress Levels

by *Stephen A. Akers*
Structures Laboratory

DTIC
ELECTE
001281993
S A D

Approved For Public Release; Distribution Is Unlimited

93 10 27 057

93-26102

Prepared for Discretionary Research Program
U.S. Army Engineer Waterways Experiment Station

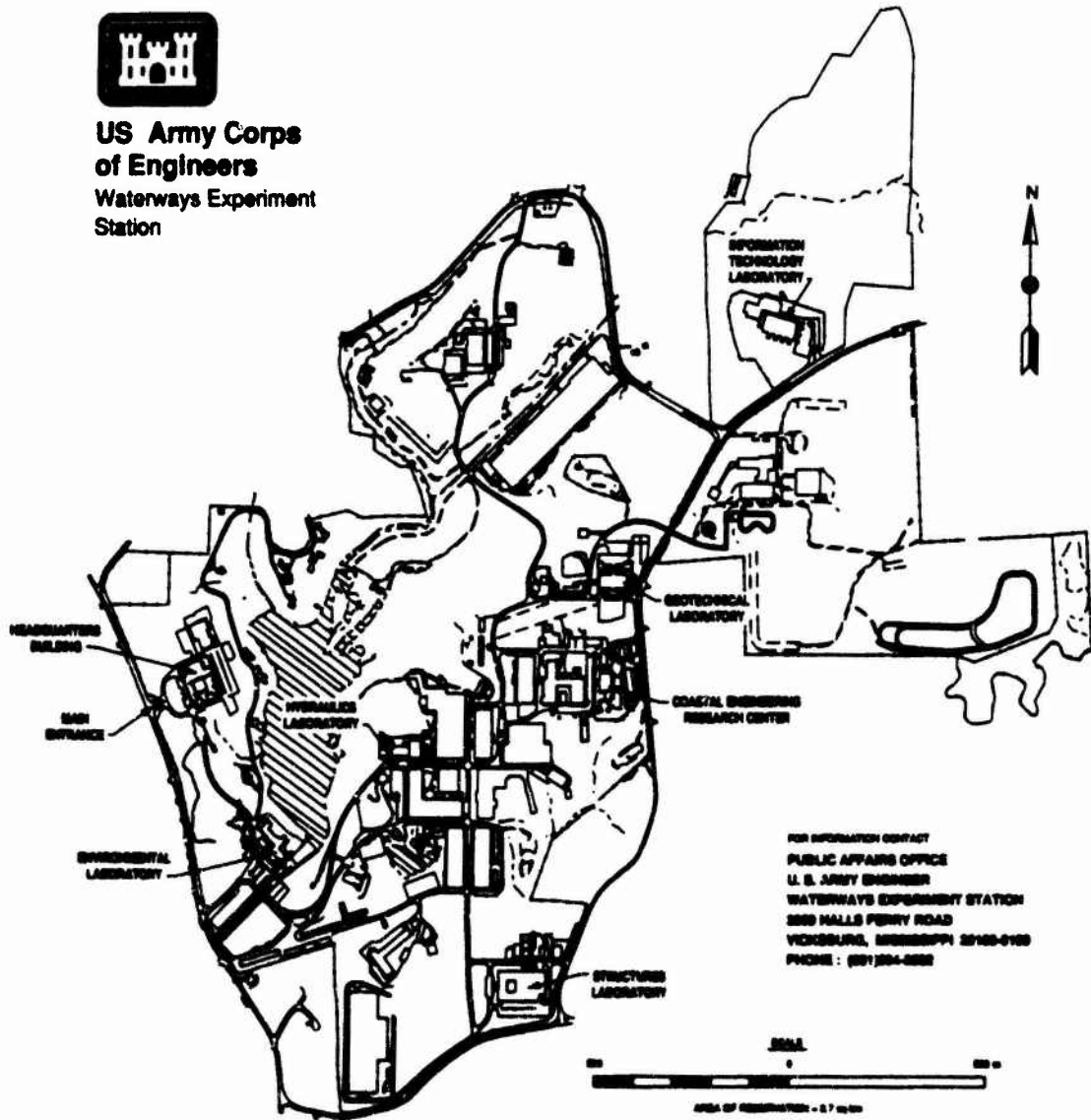
The contents of this report are not to be used for advertising, publication, or promotional purposes. Citation of trade names does not constitute an official endorsement or approval of the use of such commercial products.



PRINTED ON RECYCLED PAPER



**US Army Corps
of Engineers**
Waterways Experiment
Station



FOR INFORMATION CONTACT
PUBLIC AFFAIRS OFFICE
U. S. ARMY ENGINEER
WATERWAYS EXPERIMENT STATION
860 HALLS FERRY ROAD
VICKSBURG, MISSISSIPPI 39180-0160
PHONE: (601) 294-4882

Waterways Experiment Station Cataloging-In-Publication Data

Akers, Stephen A.

Two-dimensional finite element analysis of porous media at multikilobar stress levels / by Stephen A. Akers ; prepared for Discretionary Research Program, U.S. Army Engineer Waterways Experiment Station.

105 p. : ill. ; 28 cm. — (Technical report ; SL-93-16)

Includes bibliographical references.

1. Soils — Testing. 2. Porous materials — Testing. 3. Matter — Properties — Mathematical models. 4. Finite element method. I. U.S. Army Engineer Waterways Experiment Station. II. Discretionary Research Program (U.S. Army Engineer Waterways Experiment Station) III. Title. IV. Series: Technical report (U.S. Army Engineer Waterways Experiment Station) ; SL-93-16.

TA7 W34 no.SL-93-16

Contents

Preface	v
1-Introduction	1
Background	1
Approach	2
Purpose and Scope	3
2-Finite Element Model	4
Introduction	4
Background	4
Finite Element Formulation	6
Effective stresses and strains	6
Finite element equations	7
Equations for residual forces	11
Constitutive Models	15
Element Implemented into JAM	15
Summary	16
3-The Cap Model and Its Implementation	17
Introduction	17
Background	17
Loading Functions and Flow Rule	19
Derivation of Incremental	
Elastic-Plastic Stress-Strain Relations	21
Elastic-Plastic Constitutive Matrix	25
Plastic Hardening Modulus	27
Cap Model Implemented into JAM	28
Numerical Implementation of the Cap Model	33
Introduction	33
Elastic algorithm	34
Failure envelope algorithm	34
Cap algorithm	40
Tensile algorithm	42
Implementation of Cap Model into JAM	43
Verification	44

Summary	49
4-Equations of State for Air, Water, and Solids	50
Introduction	50
Equation of State for Water	50
Air-Water Compressibility	52
Background	52
Boyle's and Henry's laws	53
Derivation of equations	54
Equation of State for Solids	59
Summary	62
5-Features and Verification of FE Program	63
Introduction	63
Additional Features of FE Program	63
Restart feature	63
Postprocessing	64
Plane and Axisymmetric Verification	
Problems	64
Consolidation Problems	70
Cryer Problem	73
Summary	75
6-Numerical Simulations	76
Introduction	76
Salem Limestone	76
Simulations	76
Process	76
Drained limestone simulations	77
Undrained limestone simulations	79
Test Specimen Simulations	84
FE grid	84
Simulation of drained triaxial compression test	84
Simulation of consolidated undrained triaxial compression test	88
Summary	91
7-Summary	92
References	93

Preface

This investigation was sponsored by the U.S. Army Engineer Waterways Experiment Station (WES) under the Discretionary Research Program.

The work was conducted by Mr. Stephen A. Akers, Geomechanics Division (GD), Structures Laboratory (SL), WES, during the period January 1991 through March 1993, under the general direction of Dr. J. G. Jackson, Jr., Chief, GD, and Mr. J. Q. Ehrgott, Chief, Operations Group, GD. Mr. Bryant Mather is Director, SL.

At the time of publication of this report, Dr. Robert W. Whalin was the Director of WES. Commander was COL Bruce K. Howard, EN.

1 Introduction

Background

The personnel of the Geomechanics Division, Structures Laboratory, U.S. Army Engineer Waterways Experiment Station (WES) are responsible for research and development in the general field of soil and rock dynamics. Our primary interest is in the response of earth and earth-structure systems subjected to intense transient (blast-type) loadings. An analysis of these systems is typically conducted in three different phases. First, laboratory tests are conducted on the geologic materials of interest in order to develop a data base of composition and mechanical properties; then, based upon this data base, a set of recommended material properties is developed for the constitutive modelers. In the second phase, the modelers fit one or more constitutive models to the recommended material properties. Last, finite element (FE) or finite difference codes are used by the ground shock calculators to analyze the responses of these systems.

The Geomechanics Division is frequently asked to conduct mechanical property investigations. In performing these investigations, we have tested and characterized many types of materials. These materials generally fall into the following groups: moist and fully saturated cohesionless soils, desert alluviums, natural and remolded clays, clay shales, soil and rock "matching" grouts, and a variety of competent rocks. As basing and attack scenarios of the Department of Defense become more elaborate, and as the analysis techniques of modelers and ground shock calculators become more refined, greater demands are placed on the engineer who is asked to perform and analyze the laboratory mechanical property tests in order to provide recommended material properties. Modelers and calculators are now requesting total-stress mechanical property data at stress levels of several kilobars. Complicated stress- and strain-path tests are frequently included in their lists of desired material response tests. Greater emphasis in effective-stress material properties is now evident in the ground shock community.

Due to the unconventional nature of many of the requested tests, the engineer performing and analyzing the tests is sometimes uncertain about existing laboratory equipment, i.e., whether it restricts the types of tests that can be conducted. The engineer may question the measured laboratory

responses; are they theoretically realistic? An engineer may have specific questions such as: (a) what effect will small amounts of air-filled porosity have on material properties, (b) what loading rates are appropriate for conducting truly drained tests or undrained tests with meaningful pore pressure measurements, and (c) how does one calculate effective stresses at kilobar stress levels for rock-like materials? In some situations, an engineer responsible for recommending material properties may only have low pressure (less than a kilobar) total-stress and effective-stress data from which to extrapolate multikilobar material responses.

An engineer would have a tremendous advantage if a numerical tool were available with which to verify laboratory test results or to predict unavailable laboratory test data. The appropriate numerical tool should give an engineer the capability to calculate both total- and effective-stress material responses. This numerical tool would:

1. calculate strains, total and effective stresses, and pore fluid pressures for fully- and partially-saturated porous media,
2. calculate the time dependent flow of pore fluids in porous media,
3. model nonlinear irreversible stress-strain behavior, including coupled shear-induced volume change, and
4. simulate the effect of nonlinear pore fluid compressibility and the contribution of the compressibility of the grain solids for stresses up to several kilobars.

The FE code JAM incorporates all of the above features. The code simulates quasi-static, axisymmetric, laboratory mechanical property tests, i.e., the laboratory tests are analyzed as boundary value problems. Features 1 and 2 were incorporated into the code using modified formulations of Biot's coupled theory as advanced by investigators such as Zienkiewicz (1985a) and Lewis and Schrefler (1987). An elastic-plastic strain-hardening cap model calculates the time-independent skeletal responses of the porous solids. This enables the code to model nonlinear irreversible stress-strain behavior and shear-induced volume changes. In order to accurately model the total- and effective-stress responses of multikilobar laboratory tests, fluid and solid compressibilities were incorporated into the code. Following the concept used by Chang and Duncan (1983), partially-saturated materials were simulated with a "homogenized" compressible pore fluid.

Approach

To develop the FE code, four major tasks were completed. They were:

- 1) a cap model was incorporated into an existing two-dimensional finite element code PLAST and numerical experiments were conducted to verify its implementation;

- 2) a modified version of Biot's coupled theory was implemented into the code produced in step 1 above;
- 3) a data base of drained and undrained mechanical properties was obtained for a limestone with a porosity of 13.5%; it included mechanical properties from tests conducted at stress levels of up to 6 kilobars and recommended properties;
- 4) using the recommended properties from step 3, a cap model was fit to the drained properties; the undrained stress-strain and pore pressure responses of the material were calculated with the FE code and then compared to the undrained material responses.

Purpose and Scope

The purpose of this report is to document the features and algorithms implemented into the FE code JAM. Chapter 2 describes the FE model implemented into JAM and briefly documents the constitutive models available in the code. The essential features of the cap model are reviewed and the steps required to implement the cap model into the FE code JAM are summarized in Chapter 3. The equations of state for air, water, and grain solids are documented in Chapter 4, and the equations for compressibility of an air-water mixture are developed. Chapter 5 describes features in the FE program not introduced in earlier chapters and presents solutions from several verification problems as proof that the program works correctly. Numerical simulations of limestone behavior under drained and undrained boundary conditions are presented in Chapter 6. The final chapter summarizes the results of this research effort.

2 Finite Element Model

Introduction

This chapter describes the FE model implemented into JAM and briefly documents the constitutive models available in the code. The work of Biot and other investigators is described, followed by a discussion of the equations implemented by Lewis and Schrefler and modifications that must be made to those equations. In addition, the equations are derived for the residuals. Finally, the five constitutive models available in JAM for modelling skeletal behavior are described.

Background

In 1941, Biot published his three-dimensional theory of consolidation for static loading. In his theory, Biot coupled the solution of the equations of pore fluid diffusion with the equations of deformation for the porous solids. He was thus able to calculate time-dependent displacements, strains, pore fluid pressures, and effective stresses. Biot made the following assumptions in his formulation: (1) the material was isotropic, (2) the material was linear elastic, (3) small strains were applicable, (4) the pore water was incompressible, (5) the pore water could contain air bubbles, and (6) flow of the pore water obeyed Darcy's Law. In subsequent papers, Biot extended his theory to include anisotropic materials, viscoelastic materials, and dynamic processes (Biot 1955; 1962).

With the rapid development of digital computers and advances in numerical techniques such as the finite element method, many investigators expanded Biot's theory in attempts to model more realistic and more complex problems. Sandhu and Wilson (1969) were the first to use finite element techniques with Biot's original formulation to solve initial boundary value problems. They applied variational principles to the field equations of fluid flow in a fully saturated porous elastic continuum, and then used the finite element method to numerically solve the resulting coupled equations.

Ghaboussi and Wilson (1972, 1973) developed a variational formulation of Biot's dynamic field equations for saturated porous elastic solids. Their finite element formulation allowed for the compressibilities of both the fluid and solid phases. Their methods were applicable to dynamic soil-structure interaction and wave propagation problems in saturated geologic media.

Zienkiewicz and his colleagues have written extensively about their use of modified versions of Biot's formulation to solve consolidation, liquefaction, and wave propagation problems in fluid saturated porous materials (Simon *et al.* 1986a and 1986b; Zienkiewicz 1985a; Zienkiewicz *et al.* 1980; Zienkiewicz and Shiomi 1984). They have incorporated several different nonlinear constitutive models into their numerical codes. For example, Lewis *et al.* (1976), used a hyperbolic constitutive relationship to model the skeletal response of the solids. They incorporated fluid and solid compressibilities, creep, and void ratio dependent permeability into their code. Zienkiewicz and his colleagues have also demonstrated a capability to solve dynamic problems such as ground motions due to earthquakes. For example, Zienkiewicz *et al.* (1982), modified the Critical State model to include a Coulomb-type failure surface and incorporated a "cumulative densification" feature into the constitutive model that allowed pore fluid pressures to increase with increasing numbers of load-unload cycles. They then demonstrated the utility of their approach when they used their code to approximate the earthquake induced displacements and pore pressures within the Lower San Fernando Dam.

Other investigators have also expanded Biot's formulation with nonlinear constitutive models. Oka *et al.* (1986) developed an elasto-viscoplastic constitutive model for clay and used Biot's theory to study the two-dimensional consolidation response of sensitive and aged clay deposits. They demonstrated the capability of their code to simulate the consolidation response of clay deposits during the construction phase of embankments. Chang and Duncan (1983) used a modified Cam Clay constitutive model in their analyses of earth structures constructed of compacted, partially saturated clay soils. They also applied the concept of a "homogenized pore fluid" to Biot's formulation in order to model partially saturated clay soils. With this implementation, they were able to treat partially saturated soils as two-phase materials, i.e., solids and compressible pore fluid, instead of using a more theoretically rigorous approach involving three-phase materials.

Lewis and Schrefler (1987) extended Biot's formulation to include the governing equations for single phase, multiphase, and saturated-unsaturated flow in a deforming porous solid. They discussed finite element procedures for both the space and time discretization aspects of consolidation problems. They also presented linear elastic and nonlinear constitutive relationships; the nonlinear models included the hyperbolic model and incremental elastic-plastic models such as the Critical State models.

Finite Element Formulation

Effective stresses and strains

For a nonlinear material not susceptible to creep strains, a general stress-strain relation can be written as

$$\begin{aligned} d\sigma_{ij}' &= D_{ijkl} (d\epsilon_{kl} - d\epsilon_{kl}^g) \\ &= D_{ijkl} d\epsilon_{kl}' \end{aligned} \quad 2.1$$

where σ_{ij}' is the matrix of effective stresses, D_{ijkl} is the tangential stiffness matrix or constitutive matrix, $d\epsilon_{kl}$ is the matrix of total strains, $d\epsilon_{kl}^g$ is a matrix of strains due to the compression of the grains by the pore fluid and $d\epsilon_{kl}'$ is a matrix of effective strains. The matrix $d\epsilon_{kl}^g$ is evaluated as:

$$d\epsilon_{kl}^g = - \frac{d\pi}{3K_g} \delta_{kl} \quad 2.2$$

where K_g is the bulk modulus of the grains, π is the pore fluid pressure, δ_{kl} is the Kronecker delta defined by

$$\delta_{ij} = \begin{cases} = 1 & \text{if } i=j \\ = 0 & \text{if } i \neq j \end{cases}$$

and an engineering mechanics sign convention is used in which compression is negative.

The purpose of the term $d\epsilon_{kl}^g$ is illustrated in the following example. If a porous specimen surrounded by a pervious membrane was placed into a pressure vessel and a pressure of several hundred megapascals was applied, a volume decrease would be measured in the specimen due to the compression of the grains. However, since the total strain $d\epsilon_{kl}$ is equal to the volume strain due to grain compressibility, i.e., $d\epsilon_{kl} = d\epsilon_{kl}^g$, the effective strains and therefore the effective stresses within the specimen are zero. With the term $d\epsilon_{kl}^g$ included in the general stress-strain relation, effective stresses can simply be calculated as:

$$d\sigma_{ij}' = d\sigma_{ij} + \pi \delta_{ij} \quad 2.3$$

Under drained boundary conditions, the total and effective strains are equal, and the total and effective stresses are equal.

In Equation 2.3, no factor need be applied to the pore pressure term to account for grain compressibility, which was a method proposed by Skempton (1960). After appropriate manipulation, the above equations will yield Skempton's equation

$$\Delta p' = \Delta p - \left[1 - \frac{K}{K_g} \right] \Delta \pi \quad 2.4$$

where p is pressure, K and K_g are the bulk modulus of the skeleton and grain solids, respectively.

Finite element equations

The general equations developed from the spacial discretization of the equilibrium and continuity equations have been documented by a large number of investigators (Lewis and Schrefler 1987; Zienkiewicz 1985a). Lewis and Schrefler developed the following equations:

$$[K] \dot{u} - [L] \dot{\pi} - \dot{R} = 0 \quad 2.5$$

and

$$[H] \pi - [S] \dot{\pi} - [L]^T \dot{u} - Q = 0 \quad 2.6$$

where $[K]$ is the tangent stiffness matrix of the solid phase,

$$K = \int_{\Omega} B^T D_T B d\Omega \quad 2.7$$

$[L]$ is the coupling matrix between the solid and fluid phases,

$$L = \int_{\Omega} B^T m \bar{N} d\Omega - \int_{\Omega} B^T D_T \frac{m}{3K_g} \bar{N} d\Omega \quad 2.8$$

$[H]$ is the permeability matrix of the porous skeleton,

$$H = \int_{\Omega} (\nabla \bar{N})^T \frac{k}{\mu} \nabla \bar{N} d\Omega \quad 2.9$$

$[S]$ is the compressibility matrix,

$$S = \int_{\Omega} \bar{N}^T s \bar{N} d\Omega \quad 2.10$$

in which the scalar s is evaluated as

$$s = \frac{1 - \phi}{K_g} + \frac{\phi}{K_f} - \frac{1}{(3K_g)^2} m^T D_T m \quad 2.11$$

R is the external force vector,

$$R = \int_{\Omega} N^T db d\Omega + \int_{\Gamma} N^T dt d\Gamma \quad 2.12$$

Q is the vector of boundary flows,

$$Q = \int_{\Gamma} \bar{N}^T q d\Gamma + \int_{\Omega} (\nabla \bar{N})^T \frac{k}{\mu} \nabla \rho g h d\Omega \quad 2.13$$

and the superimposed dot indicates a time derivative. In the above equations, u is the vector of displacement increments, π is the vector of pore pressure increments, D_T is the elastic-plastic constitutive matrix, m is the matrix equivalent of the Kronecker delta, B is the strain-displacement matrix, N is the matrix of displacement shape functions, \bar{N} is the matrix of pore pressure shape functions, b is a vector of body forces, t is a vector of surface tractions, k is the absolute permeability matrix of the material, μ is the dynamic viscosity of the pore fluid, K_g and K_f are the bulk modulus of the grain solids and pore fluid, respectively, ϕ is the porosity of the material, q is the vector of applied fluid flux, and ρ , g and h are fluid density, gravity, and elevation head, respectively.

Lewis and Schrefler (1987) describe in detail the components that contribute to the rate of fluid accumulation. However, one of the terms in their formulation is misleading if not incorrect. The following discussion expands on their analysis and then shows why their formulation requires modification. For the material and conditions of interest, Lewis and Schrefler specify that four volumetric strain components must be evaluated; they are the volume strain of the porous matrix ϵ_v^m , the volume strains of the grain solids ϵ_v^g and the pore fluid ϵ_v^f , and a component of solid volume strain $\epsilon_v^{g^c}$ due to the applied effective stresses. To simplify the discussion of fluid accumulation, consider the following test conditions. A fully saturated porous material is contained in a sample chamber, which has frictionless sides, and is loaded by a frictionless piston with area A . A flow meter attached to the piston indicates the direction of fluid flow into (positive flow) or out of (negative flow) the sample. The top surface of the piston is loaded by a chamber pressure P_1 and a second fluid pressure P_2 is applied through the flow meter to the pore fluid within the sample. The fluid pressures P_1 and P_2 control the total and effective stresses within the sample. Recall that for a porous material with a

volume of unity, the volume of the voids is n , and the volume of the solids is $1-n$.

If P_1 is increased and P_2 held constant, the effective stress in the specimen will increase, the material will compress, and pore fluid will flow out of the specimen. Since the specimen is fully saturated with fluid, the rate of change in fluid accumulation is equal to the volumetric strain of the porous matrix and may be written as:

$$\frac{\partial \epsilon_v^m}{\partial t} = \frac{\partial \epsilon_{kk}}{\partial t} = \frac{\partial \epsilon_{ij}}{\partial t} \delta_{ij} \quad 2.14$$

If P_1 and P_2 are increased at the same rate, the effective stress within the specimen will not change. However, both the grain solids and the pore fluid will compress due to the change in pore fluid pressure. For these conditions, fluid will flow into the specimen. Let us evaluate the solid and fluid components separately. The volume strain in the solids due to an applied pressure is expressed as:

$$d\epsilon_s = \frac{dV}{V_s} = \frac{-dP}{K_g} \quad 2.15$$

where K_g is the bulk modulus of the grains and V_s is the volume of the solids. From this equation, we can express the volume change within the unit volume due to the compression of the grains as:

$$d\epsilon_v^g = (1-n)d\epsilon_s = (1-n) \frac{-d\pi}{K_g} \quad 2.16$$

where dP has been replaced by the pore fluid pressure $d\pi$.

In the same manner, the volume change within the unit volume due to the compression of the pore fluid is written as:

$$d\epsilon_v^f = -n \frac{d\pi}{K_f} \quad 2.17$$

where K_f is the bulk modulus of the pore fluid.

Lewis and Schrefler also evaluate the component of volume strain due to the compression of the grains caused by the increase in effective stress. A similar analysis was developed by Bishop (1973). Refer again to the test configuration and the example in which P_1 was increased and P_2 held constant. For a statistically random distribution of pore space within the

specimen, the area of solids (A_s) on any plane through the specimen will be

$$A_s = (1 - n)A \quad 2.18$$

where n is the porosity of the specimen as previously defined. If $d\sigma_{ij}'$ is the average normal effective stress on any surface, then $d\sigma_{ij}' / (1 - n)$ is the average normal stress in the solids. Using the concept implied by Equation 2.15, the pressure applied to the solids can be expressed as:

$$dP = \frac{-d\sigma_{ij}'}{3(1-n)} \delta_{ij} = \frac{-d\sigma_{kk}'}{3(1-n)} \quad 2.19$$

which when substituted into Equation 2.16 gives:

$$d\epsilon_s = \frac{dV}{V_s} = \frac{dV}{(1-n)V} = \frac{d\sigma_{kk}'}{3K_g(1-n)} \quad 2.20$$

The component of volume strain due to the applied effective stresses for the unit volume is then:

$$d\epsilon_v^{ge} = \frac{dV}{V} = \frac{d\sigma_{kk}'}{3K_g} \quad 2.21$$

The components of the volume strain are now:

$$\frac{\partial \epsilon_{kk}}{\partial t} = \frac{\partial \epsilon_v^m}{\partial t} - \frac{\partial \epsilon_v^{ge}}{\partial t} - \frac{\partial \epsilon_v^g}{\partial t} - \frac{\partial \epsilon_v^f}{\partial t} \quad 2.22$$

and the expressions for each component when substituted gives:

$$\frac{\partial \epsilon_{kk}^{total}}{\partial t} = \frac{\partial \epsilon_{kk}^{matrix}}{\partial t} - \frac{1}{3K_g} \frac{\partial \sigma_{kk}'}{\partial t} + \left[\frac{1-n}{K_g} + \frac{n}{K_f} \right] \frac{\partial \pi}{\partial t} \quad 2.23$$

The term in dispute is the component of volume strain due to the applied effective stresses. Grain compression due to changes in effective pressure is already incorporated into all skeletal constitutive models by default. In an analysis of drained test data, the skeletal strains are not decoupled from the grain strains, and the sum of the two is always measured by strain gauges or deformeters. Therefore, both components are included when a constitutive model is fit to drained hydrostatic loading data. A similar argument can be made by examining Equation 2.23. During a drained test, Equation 2.23 would reduce to the following

$$\frac{\partial \epsilon_{kk}}{\partial t} = \frac{\partial \epsilon_{ij}}{\partial t} \delta_{ij} - \frac{1}{3K_g} \frac{\partial \sigma_{kk}'}{\partial t} \quad 2.24$$

Clearly, this is in error; the only strains included in the above expression should be the skeletal strains. Therefore, one should only include grain compression due to changing pore pressures in the final formulation. The necessary modifications were made to Equations 2.8 and 2.11, which are rewritten below

$$L = \int_{\Omega} B^T m \bar{N} d\Omega \quad 2.25$$

and

$$s = \frac{1 - \phi}{K_g} + \frac{\phi}{K_f} \quad 2.26$$

Equations for residual forces

Although numerous papers pertaining to the FE equations governing pore fluid flow in a deforming porous solid are available, none outline the equations required to calculate the residual forces. In this section, these equations are developed for a nonlinear incremental finite element program that employs a modified Newton-Raphson solution scheme.

The time integration of Equations 2.5 and 2.6 is performed using the following approximation:

$$\int_t^{t+\Delta t} \chi dt = \alpha \Delta t {}^{t+\Delta t} \chi + (1 - \alpha) \Delta t {}^t \chi \quad 2.27$$

for $0 \leq \alpha \leq 1$. From Equation 2.27, the following are developed:

$${}^{t+\alpha\Delta t} \dot{\chi} = \frac{{}^{t+\Delta t} \chi - {}^t \chi}{\Delta t} \quad 2.28$$

and

$${}^{t+\alpha\Delta t} \chi = (1 - \alpha) {}^t \chi + \alpha {}^{t+\Delta t} \chi \quad 2.29$$

Table 2.1 gives the most common difference schemes adopted by the selection of a given value of α . Equation 2.5 may be written for a given time

Table 2.1.
Time Integration Parameters

Value α	Difference Scheme	Stability
0	Forward or Euler	Conditionally
1/2	Crank-Nicolson	Unconditionally
1/4	Galerkin	Unconditionally
1	Backward	Conditionally

$t + \alpha \Delta t$ as:

$${}^{t+\alpha\Delta t}[K] {}^{t+\alpha\Delta t}\dot{u} - {}^{t+\alpha\Delta t}[L] {}^{t+\alpha\Delta t}\dot{\pi} = {}^{t+\alpha\Delta t}\dot{R} \quad 2.30$$

Equations 2.28 and 2.29 are introduced into Equation 2.30 to produce the following

$${}^{t+\Delta t}[K] \left\{ \frac{{}^{t+\Delta t}u - {}^t u}{\Delta t} \right\} - {}^{t+\Delta t}[L] \left\{ \frac{{}^{t+\Delta t}\pi - {}^t \pi}{\Delta t} \right\} \quad 2.31$$

$$= \frac{{}^{t+\Delta t}R - {}^t R}{\Delta t}$$

Multiplying by Δt and collecting terms, one obtains

$${}^{t+\Delta t}[K] \{ {}^{t+\Delta t}u - {}^t u \} - {}^{t+\Delta t}[L] \{ {}^{t+\Delta t}\pi - {}^t \pi \} \quad 2.32$$

$$= {}^{t+\Delta t}R - {}^t R$$

In general, Equation 2.32 represents nonlinear behavior. The relationship may be linearized with the following expressions:

$${}^{t+\Delta t}u^{(i)} = {}^{t+\Delta t}u^{(i-1)} + \delta u^{(i)} \quad 2.33$$

$${}^{t+\Delta t}\pi^{(i)} = {}^{t+\Delta t}\pi^{(i-1)} + \delta \pi^{(i)} \quad 2.34$$

where i represents the current iteration, and the initial conditions are

${}^{t+\Delta t}u^{(0)} = {}^t u$ and ${}^{t+\Delta t}\pi^{(0)} = {}^t \pi$. This linearization can be used as the first step in a Newton-Raphson iteration (Bathe 1982). If Equations 2.33

and 2.34 are substituted into Equation 2.32 and the terms for iterations ($i-1$) and (0) are brought to the right hand side of the equation, then one obtains:

$$\begin{aligned} {}^{t+\Delta t}[K]\delta u^{(i)} - {}^{t+\Delta t}[L]\delta \pi^{(i)} &= {}^{t+\Delta t}R - {}^tR \\ &- {}^{t+\Delta t}[K]\{ {}^{t+\Delta t}u^{(i-1)} - {}^{t+\Delta t}u^{(0)} \} \\ &+ {}^{t+\Delta t}[L]\{ {}^{t+\Delta t}\pi^{(i-1)} - {}^{t+\Delta t}\pi^{(0)} \} \end{aligned} \quad 2.35$$

Recognizing that

$${}^tR = {}^{t+\Delta t}[K] {}^{t+\Delta t}u^{(0)} - {}^{t+\Delta t}[L] {}^{t+\Delta t}\pi^{(0)} \quad 2.36$$

Equation 2.35 may be written in terms of the incremental or accumulative stresses and pore pressures as

$$\begin{aligned} {}^{t+\Delta t}[K]\delta u^{(i)} - {}^{t+\Delta t}[L]\delta \pi^{(i)} &= \\ &{}^{t+\Delta t}R - {}^{t+\Delta t}F^{(i-1)} + {}^{t+\Delta t}C^{(i-1)} \end{aligned} \quad 2.37$$

where ${}^{t+\Delta t}F^{(i-1)} = \int_V B^T {}^{t+\Delta t}\sigma^{(i-1)} dV$ and

$${}^{t+\Delta t}C^{(i-1)} = {}^{t+\Delta t}[L]^{(i-1)} {}^{t+\Delta t}\pi^{(i-1)}$$

Equation 2.37 is one of the two equations required to solve for pore fluid flow in a deforming nonlinear porous solid. The second equation is developed from Equation 2.6 and is written at time $t+\alpha\Delta t$ as:

$$[H] {}^{t+\alpha\Delta t}\pi - [S] {}^{t+\alpha\Delta t}\dot{\pi} - [L]^T {}^{t+\alpha\Delta t}\dot{u} = {}^{t+\alpha\Delta t}Q \quad 2.38$$

Equations 2.28 and 2.29 are introduced into Equation 2.38 to produce

$$\begin{aligned} [H]\{(1-\alpha) {}^t\pi + \alpha {}^{t+\Delta t}\pi\} - [S] \left\{ \frac{{}^{t+\Delta t}\pi - {}^t\pi}{\Delta t} \right\} \\ - [L]^T \left\{ \frac{{}^{t+\Delta t}u - {}^tu}{\Delta t} \right\} \\ = (1-\alpha) {}^tQ + \alpha {}^{t+\Delta t}Q \end{aligned} \quad 2.39$$

Collecting terms and multiplying by Δt one obtains:

$$\begin{aligned} \{ -[S] + \alpha \Delta t [H] \} {}^{i+\Delta t} \pi - [L]^T \{ {}^{i+\Delta t} u - {}^i u \} \\ + \{ [S] + (1-\alpha) \Delta t [H] \} {}^i \pi = P \end{aligned} \quad 2.40$$

where $P = \Delta t \{ (1-\alpha) {}^i Q + \alpha {}^{i+\Delta t} Q \}$. If the following equations

$$\hat{S} = -[S] + \alpha \Delta t [H] \quad 2.41$$

and

$$\hat{H} = [S] + (1-\alpha) \Delta t [H] = \Delta t [H] - \hat{S} \quad 2.42$$

are substituted into Equation 2.40 for simplification, then one obtains

$$\hat{S} {}^{i+\Delta t} \pi - [L]^T {}^{i+\Delta t} u = P - \hat{H} {}^i \pi - [L]^T {}^i u \quad 2.43$$

Equation 2.43 must now be formulated for general nonlinear behavior using the same linearization process applied to Equation 2.32, i.e., Equations 2.33 and 2.34 must be substituted. This operation produces

$$\begin{aligned} {}^{i+\Delta t} \hat{S} \{ {}^{i+\Delta t} \pi^{(i-1)} + \delta \pi^{(i)} \} - {}^{i+\Delta t} [L]^T \{ {}^{i+\Delta t} u^{(i-1)} + \delta u^{(i)} \} \\ = {}^{i+\Delta t} P - {}^{i+\Delta t} \hat{H} {}^{i+\Delta t} \pi^{(0)} - {}^{i+\Delta t} [L]^T {}^{i+\Delta t} u^{(0)} \end{aligned} \quad 2.44$$

Collecting the δu and $\delta \pi$ terms on the left hand side of the equation, one gets

$$\begin{aligned} {}^{i+\Delta t} \hat{S} \delta \pi^{(i)} - {}^{i+\Delta t} [L]^T \delta u^{(i)} = {}^{i+\Delta t} P - {}^{i+\Delta t} \hat{H} {}^{i+\Delta t} \pi^{(0)} \\ - {}^{i+\Delta t} \hat{S} {}^{i+\Delta t} \pi^{(i-1)} + {}^{i+\Delta t} [L]^T \{ {}^{i+\Delta t} u^{(i-1)} - {}^{i+\Delta t} u^{(0)} \} \end{aligned} \quad 2.45$$

Equations 2.41 and 2.42 can be used to eliminate the terms \hat{H} and \hat{S} from the right hand side of Equation 2.45 to produce

$$\begin{aligned} {}^{i+\Delta t} \hat{S} \delta \pi^{(i)} - {}^{i+\Delta t} [L]^T \delta u^{(i)} = {}^{i+\Delta t} P \\ - \Delta t {}^{i+\Delta t} H {}^{i+\Delta t} \pi^{(0)} - {}^{i+\Delta t} G^{(i-1)} + {}^{i+\Delta t} M^{(i-1)} \end{aligned} \quad 2.46$$

where ${}^{i+\Delta t} G^{(i-1)} = \{ - {}^{i+\Delta t} [S]^{(i-1)} + \alpha \Delta t {}^{i+\Delta t} [H]^{(i-1)} \} {}^{i+\Delta t} \Delta \pi^{(i-1)}$,
 ${}^{i+\Delta t} M^{(i-1)} = {}^{i+\Delta t} [L]^T {}^{(i-1)} {}^{i+\Delta t} \Delta u^{(i-1)}$,
 ${}^{i+\Delta t} \Delta \pi^{(i-1)} = {}^{i+\Delta t} \pi^{(i-1)} - {}^{i+\Delta t} \pi^{(0)}$,
 ${}^{i+\Delta t} \Delta u^{(i-1)} = {}^{i+\Delta t} u^{(i-1)} - {}^{i+\Delta t} u^{(0)}$,
 ${}^{i+\Delta t} \Delta u^{(0)} = 0$ and ${}^{i+\Delta t} \Delta \pi^{(0)} = 0$.

Equations 2.37 and 2.46 are written in matrix form for increment $t + \Delta t$ as:

$$\begin{bmatrix} K & -L \\ -L^T & -S + \alpha \Delta t H \end{bmatrix} \begin{Bmatrix} \delta u^{(i)} \\ \delta \pi^{(i)} \end{Bmatrix} = \begin{Bmatrix} R - F^{(i-1)} + C^{(i-1)} \\ P - \Delta t [H] \pi^{(0)} - G^{(i-1)} + M^{(i-1)} \end{Bmatrix}$$

2.47

This is the system of equations that must be solved to calculate displacements and pore fluid pressures in a deforming porous solid.

Constitutive Models

Four of the five constitutive models available in the FE code JAM were developed by Owen and Hinton (1980). These models were implemented by Owen and Hinton in the FE code PLAST, which was the original FE code on which JAM was built. Each of the four models were implemented as elastic-plastic models with linear strain hardening, and each has a different yield criteria. The four models include the Tresca and von Mises criteria, which are suitable for metal plasticity, and the Coulomb and Drucker-Prager criteria, which are more suitable for the simulation of soil, rock, and concrete.

The yield stresses in both the Tresca and von Mises criteria are independent of pressure, which makes these models unsuitable for simulating the pressure dependent material behavior exhibited by soil, rock and concrete. In contrast, yield stresses in the Coulomb and Drucker-Prager criteria are pressure dependent. For more information on these models, the reader should refer to Chapter 7 in Owen and Hinton (1980).

An elastic-plastic strain-hardening cap model was implemented into JAM to calculate the time-independent skeletal response of the porous solids. The cap model enables the FE code to model nonlinear irreversible stress-strain behavior and shear-induced volume changes. Chapter 3 contains extensive documentation on the cap model.

Element Implemented into JAM

A new element was implemented into JAM to calculate both the displacement and pore fluid pressures. JAM uses an eight-node isoparametric element with 16 displacement and four pore fluid degrees of freedom. Similar elements were used by Lewis and Schrefler (1987), Simon *et al.* (1986a; 1986b), Zienkiewicz (1985a), Zienkiewicz *et al.* (1980), and Zienkiewicz and Shiomi (1984). Four Gauss integration points are utilized in each element.

Summary

In this chapter, the work of Biot and other investigators was briefly described, followed by a discussion of the modified Biot equations implemented by Lewis and Schrefler and modifications that were made to those equations. In addition, equations were derived for the residual forces. Finally, the five constitutive models available in JAM and the element implemented into JAM were described.

3 The Cap Model and Its Implementation

Introduction

The "cap model falls within the framework of the classical incremental theory of work-hardening plasticity for materials that have time- and temperature-independent properties" (Chen and Baladi 1985). When modelling geologic materials subjected to stresses ranging from one to several hundred megapascals, the cap model has several desirable features. Of primary importance is its ability to model volumetric hysteresis through the use of a strain-hardening yield surface or cap.

In this chapter, the essential features of the cap model are reviewed, and the steps required to implement the cap model into the finite element code JAM are summarized. After a brief evaluation of the loading function and flow rule, the incremental elastic-plastic stress-strain relations are outlined. In addition, the cap model implemented into JAM is described, and the equations are developed for the elastic-plastic constitutive matrix and the plastic hardening modulus. Finally, the numerical implementation of the cap model itself is described. The reader should note that an engineering mechanics sign convention is used in which compression is negative.

Background

The cap model has been used by researchers in the ground shock community for approximately 20 years to simulate the responses of a wide variety of geologic materials. It is "predicated on the fact that the volumetric hysteresis exhibited by many geologic materials can also be described by a plasticity model, if the model is based on a hardening yield surface which includes conditions of hydrostatic stress" (Sandler et al. 1976). The model was first described in the open literature by DiMaggio and Sandler (1971). The FORTRAN source code for the model was published by Sandler and Rubin (1979).

As stated above, the cap model has several desirable features. Of primary importance is its ability to model volumetric hysteresis through the use of a strain-hardening yield surface or cap. The cap model may also be formulated with a nonlinear failure surface, with linear or nonlinear elastic moduli, or as a function of the third stress invariant. With the appropriate selection of material parameters, it can be used as a linear elastic or linear elastic-perfectly plastic material model. Sandler and Rubin (1979) demonstrated notable foresight with their use of function statements within the model, which allow substantial changes to be made to the cap model's potential functions with little programming effort.

Modifications and expansions of the original model were made by several researchers. Effective-stress versions of the cap model are reported in Baladi (1979), Baladi and Akers (1981), and Baladi and Rohani (1977, 1978, 1979). A transverse-isotropic cap was developed by Baladi (1978) and an elastic-viscoplastic cap model by Baladi and Rohani (1982). Rubin and Sandler (1977) developed a high-pressure cap model for ground shock calculations due to subsurface explosions. Baladi (1986) developed a "complex" strain-dependent cap model, which required 39 model parameters, for ground shock calculations of a dry cemented sand. In addition, several versions of the cap model are described in the text by Chen and Baladi (1985).

In formulating the cap model, DiMaggio and Sandler (1971) complied with the constraints imposed by Drucker's stability postulate. Drucker's stability postulate is sufficient, although not necessary, to satisfy all thermodynamic and continuity requirements for continuum models (Sandler et al. 1976). Satisfying Drucker's stability postulate insures uniqueness, continuity, and stability of a solution and provides a mathematical problem that is properly posed. Rubin and Sandler (1977) state that "...the numerical solution to a properly posed problem can proceed without the fear that the results will be strongly dependent on errors of approximation of initial and boundary conditions, round off error, etc." Drucker (1951) defines a work-hardening material as one that remains in equilibrium under an added set of stresses applied by an external agency. It also means that "(a) positive work is done by the external agency during the application of the added set of stresses and (b) the net work performed by the external agency over the cycle of application and removal is positive if plastic deformation has occurred in the cycle" (Drucker 1951). Drucker (1950) states these two conditions in a mathematical format as

$$d\sigma_{ij} de_{ij} > 0 \quad \text{and} \quad d\sigma_{ij} de_{ij}^p \geq 0$$

The first statement constrains a model such that strain-softening may not occur. The second statement implies (a) the loading function or yield surface must be convex and (b) the plastic strain increment vector must be normal to the yield surface, which means that an associated flow rule must be used. These are the constraints imposed by Drucker's stability postulate.

Loading Functions and Flow Rule

Drucker's criteria for stability permits considerable flexibility in the functional forms of the loading function f . Since Drucker's stability postulate requires the yield surface and plastic potential surface to coincide, the loading function f implicitly represents both the yield and potential surfaces. For a perfectly plastic material, a general form of the loading function may be written as

$$f(\sigma_{ij}) = 0 \quad 3.1$$

and as

$$f(\sigma_{ij}, \kappa) = 0 \quad 3.2$$

for a strain- or work-hardening material, where κ is a hardening parameter that acts as an "internal state variable that measures hardening as a function of the history of plastic volumetric strain" (Sandler and Rubin 1979). For isotropic materials, the loading function may be expressed in terms of stress invariants, e.g.,

$$f(J_1, \sqrt{J_{2D}}, \kappa) = 0 \quad 3.3$$

where $J_1 = \sigma_{kk}$ = the trace of the stress tensor and

$J_{2D} = \frac{1}{2} s_{ij} s_{ij}$ = the second invariant of the deviatoric stress tensor.

This is the form of the loading function used in most versions of the cap model. The loading function is assumed to be isotropic and is comprised of two surfaces, an ultimate failure envelope and a strain-hardening surface or cap. The failure envelope, which is fixed in space and symmetric about the hydrostatic axis, limits the maximum shear stresses in the material and is expressed as

$$f = h(J_1, \sqrt{J_{2D}}) = \sqrt{J_{2D}} - Q(J_1) = 0 \quad 3.4$$

The cap, which moves as plastic deformations occur, is represented as

$$f = H(J_1, \sqrt{J_{2D}}, \kappa) = \sqrt{J_{2D}} - F(J_1, \kappa) = 0 \quad 3.5$$

The hardening parameter κ is generally taken to be a function of the plastic volume strain (Chen and Baladi 1985)

$$\kappa = g_1 (\epsilon_{kk}^p) \quad 3.6$$

Equation 3.6 allows the cap to expand and contract. By allowing the cap to contract, one can limit the amount of dilation that a material may develop when its stress path moves along the failure envelope h . This form of the hardening parameter is typically used for soil-like materials that do not exhibit significant dilation during failure. For rock-like materials, the hardening parameter may be written as

$$\kappa = g_2 [(\epsilon_{kk}^p)_{\max}] \quad 3.7$$

In this form, the cap is only permitted to expand, thus allowing a material to dilate while its stress path moves along the failure envelope, i.e., when $h = 0$. Both Equations 3.6 and 3.7 produce hysteresis during an imposed hydrostatic load-unload cycle (Baladi and Akers 1981).

The plastic loading criteria for the loading function f are given by

$$\frac{\partial f}{\partial \sigma_{ij}} d\sigma_{ij} \begin{cases} > 0 & \text{loading} \\ = 0 & \text{neutral loading} \\ < 0 & \text{unloading} \end{cases} \quad 3.8$$

(Baladi and Akers 1981). These criteria imply that during loading from a point on a given yield surface a stress increment tensor $d\sigma_{ij}$ (when viewed as a vector) will point outward (Rohani 1977). Plastic strains will only occur under this condition. During unloading, the stress vector points inward, and the material will behave elastically. Neutral loading occurs when the stress vector is tangent to the yield surface. During neutral loading, no plastic strains are produced in the case of a work-hardening material (Rohani 1977). This is referred to as the "continuity condition", and its satisfaction leads to the coincidence of elastic and plastic constitutive equations (Chen and Baladi 1985).

Drucker (1951) has shown that the plastic strain increment tensor for a work-hardening material may be written as

$$d\epsilon_{ij}^p = \begin{cases} d\lambda \frac{\partial f}{\partial \sigma_{ij}} & \text{if } f = 0 \text{ and } \frac{\partial f}{\partial \sigma_{ij}} d\sigma_{ij} > 0 \\ 0 & \text{if } f < 0, \text{ or } f = 0 \text{ and } \frac{\partial f}{\partial \sigma_{ij}} d\sigma_{ij} \leq 0 \end{cases} \quad 3.9$$

which is identical to the expression used for elastic-perfectly plastic materials. The term $d\lambda$ is a positive factor of proportionality that is nonzero only when

plastic deformations occur (Baladi and Akers 1981). For the cap model, the loading function f may take the form of either Equation 3.4 or 3.5.

Derivation of Incremental Elastic-Plastic Stress-Strain Relations

The basic premise in the formulation of the cap model and all elastic-plastic constitutive models is that certain materials are capable of undergoing small plastic (permanent) strains as well as small elastic (recoverable) strains during each loading increment (Baladi and Akers 1981). This may be expressed mathematically as

$$d\epsilon_{ij} = d\epsilon_{ij}^e + d\epsilon_{ij}^p \quad 3.10$$

where $d\epsilon_{ij}$ = components of the total strain increment tensor,
 $d\epsilon_{ij}^e$ = components of the elastic strain increment tensor, and
 $d\epsilon_{ij}^p$ = components of the plastic strain increment tensor.

This equation simply states that the total strain increment is equal to the sum of the elastic and plastic strain increments. In its most general form, the elastic strain increment tensor may be expressed as

$$d\epsilon_{ij}^e = C_{ijkl} d\sigma_{kl} \quad 3.11$$

where $C_{ijkl}(\sigma_{mn})$ = the material response function, which may be a function of stress. For isotropic materials, the elastic strain increment tensor may be expressed as

$$d\epsilon_{ij}^e = \frac{dJ_1}{9K} \delta_{ij} + \frac{ds_{ij}}{2G} \quad 3.12$$

where $s_{ij} = \sigma_{ij} - (J_1/3)\delta_{ij}$ = the deviatoric stress tensor,

δ_{ij} = the Kronecker delta, and

K and G are the elastic bulk and shear moduli, respectively.

The elastic bulk and shear moduli may be constants or functions of stress or strain invariants, e.g.,

$$\begin{aligned} K &= K(J_1, J_{2D}, J_{3D}) \\ G &= G(J_1, J_{2D}, J_{3D}) \end{aligned} \quad 3.13$$

where $J_{3D} = \frac{1}{3}s_{ij}s_{jk}s_{ki}$ = the third invariant of the deviatoric stress tensor.

Chen and Baladi (1985) discuss the thermodynamic restrictions to the possible forms of the above equations. Permissible functional forms of K and G must not generate energy or hysteresis and must maintain the path-independent behavior of elastic materials. Thus, the bulk and shear moduli should be limited to the following forms (Chen and Baladi 1985)

$$\begin{aligned} K &= K(J_1, \epsilon_{ij}^p) \\ G &= G(J_{2D}, \epsilon_{ij}^p) \end{aligned} \quad 3.14$$

Inclusion of the plastic strain tensor into the functional forms of K and G is permitted since plastic strains are constant during periods of elastic deformation. Under these restrictions, the hydrostatic and deviatoric components of the elastic strain increment tensor (Equation 3.12) may be written as

$$d\epsilon_{kk}^e = \frac{dJ_1}{3K(J_1, \epsilon_{ij}^p)} \quad 3.15$$

and

$$d\epsilon_{ij}^e = \frac{ds_{ij}}{2G(J_{2D}, \epsilon_{ij}^p)} \quad 3.16$$

Combining Equations 3.9 and 3.12, the total strain increment tensor can be written as

$$d\epsilon_{ij} = \frac{dJ_1}{9K} \delta_{ij} + \frac{ds_{ij}}{2G} + d\lambda \frac{\partial f}{\partial \sigma_{ij}} \quad 3.17$$

The plastic strain increment tensor (Equation 3.9) may also be expressed in terms of the hydrostatic and deviatoric components of strain. Applying the chain rule of differentiation to the right-hand side of Equation 3.9 results in

$$d\epsilon_{ij}^p = d\lambda \left[\frac{\partial f}{\partial J_1} \frac{\partial J_1}{\partial \sigma_{ij}} + \frac{\partial f}{\partial \sqrt{J_{2D}}} \frac{\partial \sqrt{J_{2D}}}{\partial \sigma_{ij}} \right] \quad 3.18$$

which simplifies to

$$d\epsilon_{ij}^p = d\lambda \left[\frac{\partial f}{\partial J_1} \delta_{ij} + \frac{1}{2\sqrt{J_{2D}}} \frac{\partial f}{\partial \sqrt{J_{2D}}} s_{ij} \right] \quad 3.19$$

Multiplying both sides of Equation 3.19 by δ_{ij} gives an expression for the plastic volumetric strain

$$d\epsilon_{kk}^p = 3 d\lambda \frac{\partial f}{\partial J_1} \quad 3.20$$

By definition, the deviatoric component of the plastic strain increment tensor is written as:

$$de_{ij}^p = d\epsilon_{ij}^p - \frac{1}{3} d\epsilon_{kk}^p \delta_{ij} \quad 3.21$$

Substitution of Equations 3.19 and 3.20 into Equation 3.21 gives

$$de_{ij}^p = \frac{d\lambda}{2\sqrt{J_{2D}}} \frac{\partial f}{\partial \sqrt{J_{2D}}} s_{ij} = d\lambda \frac{\partial f}{\partial s_{ij}} \quad 3.22$$

The proportionality factor $d\lambda$ must be determined prior to evaluating any of the above plastic strains. Baladi and Akers(1981), Chen and Baladi(1985), and Rohani(1977) outline the methods required to evaluate the proportionality factor. Those methods are included here for completeness.

Using Equations 3.4, 3.5, and 3.6 or 3.7, the total derivative of the loading function f may be expressed as

$$df = \frac{\partial f}{\partial J_1} dJ_1 + \frac{1}{2\sqrt{J_{2D}}} \frac{\partial f}{\partial \sqrt{J_{2D}}} s_{ij} ds_{ij} + \frac{\partial f}{\partial \kappa} \frac{\partial \kappa}{\partial \epsilon_{kk}^p} d\epsilon_{mm}^p = 0 \quad 3.23$$

This expression is known as the "consistent condition" for strain-hardening materials (Chen and Baladi 1985). Using Equations 3.15, 3.16, and 3.20, Equation 3.23 may be manipulated to give

$$3K d\epsilon_{kk}^e \frac{\partial f}{\partial J_1} + \frac{G de_{ij}^e}{\sqrt{J_{2D}}} \frac{\partial f}{\partial \sqrt{J_{2D}}} s_{ij} + 3 d\lambda \frac{\partial f}{\partial J_1} \frac{\partial f}{\partial \kappa} \frac{\partial \kappa}{\partial \epsilon_{kk}^p} = 0 \quad 3.24$$

Substitution of Equation 3.10 into Equation 3.24 produces

$$3K (d\epsilon_{kk}^e - d\epsilon_{kk}^p) \frac{\partial f}{\partial J_1} + \frac{G}{\sqrt{J_{2D}}} (de_{ij}^e - de_{ij}^p) \frac{\partial f}{\partial \sqrt{J_{2D}}} s_{ij} = -3 d\lambda \frac{\partial f}{\partial J_1} \frac{\partial f}{\partial \kappa} \frac{\partial \kappa}{\partial \epsilon_{kk}^p} \quad 3.25$$

By substituting Equations 3.20 and 3.22 into Equation 3.25, one obtains

$$3K \frac{\partial f}{\partial J_1} d\epsilon_{kk} + \frac{G}{\sqrt{J_{2D}}} \frac{\partial f}{\partial \sqrt{J_{2D}}} s_{ij} de_{ij} = \quad 3.26$$

$$d\lambda \left[9K \left(\frac{\partial f}{\partial J_1} \right)^2 + G \left(\frac{\partial f}{\partial \sqrt{J_{2D}}} \right)^2 - 3 \frac{\partial f}{\partial J_1} \frac{\partial f}{\partial \kappa} \frac{\partial \kappa}{\partial \epsilon_{kk}^p} \right]$$

Solving for the proportionality factor $d\lambda$ yields

$$d\lambda = \frac{3K \frac{\partial f}{\partial J_1} d\epsilon_{kk} + \frac{G}{\sqrt{J_{2D}}} \frac{\partial f}{\partial \sqrt{J_{2D}}} s_{ij} de_{ij}}{9K \left(\frac{\partial f}{\partial J_1} \right)^2 + G \left(\frac{\partial f}{\partial \sqrt{J_{2D}}} \right)^2 - 3 \frac{\partial f}{\partial J_1} \frac{\partial f}{\partial \kappa} \frac{\partial \kappa}{\partial \epsilon_{kk}^p}} \quad 3.27$$

By using Equations 3.17, 3.19, and 3.27, the total strain increment tensor may be written as

$$d\epsilon_{ij} = \frac{dJ_1}{9K} \delta_{ij} + \frac{ds_{ij}}{2G}$$

$$+ \left[\frac{3K \frac{\partial f}{\partial J_1} d\epsilon_{kk} + \frac{G}{\sqrt{J_{2D}}} \frac{\partial f}{\partial \sqrt{J_{2D}}} s_{ij} de_{ij}}{9K \left(\frac{\partial f}{\partial J_1} \right)^2 + G \left(\frac{\partial f}{\partial \sqrt{J_{2D}}} \right)^2 - 3 \frac{\partial f}{\partial J_1} \frac{\partial f}{\partial \kappa} \frac{\partial \kappa}{\partial \epsilon_{kk}^p}} \right] \quad 3.28$$

$$\times \left[\frac{\partial f}{\partial J_1} \delta_{ij} + \frac{s_{ij}}{2\sqrt{J_{2D}}} \frac{\partial f}{\partial \sqrt{J_{2D}}} \right]$$

The stress increment tensor may be written as

$$d\sigma_{ij} = K d\epsilon_{kk} \delta_{ij} + 2G de_{ij}$$

$$+ \left[\frac{3K \frac{\partial f}{\partial J_1} d\epsilon_{kk} + \frac{G}{\sqrt{J_{2D}}} \frac{\partial f}{\partial \sqrt{J_{2D}}} s_{ij} de_{ij}}{9K \left(\frac{\partial f}{\partial J_1} \right)^2 + G \left(\frac{\partial f}{\partial \sqrt{J_{2D}}} \right)^2 - 3 \frac{\partial f}{\partial J_1} \frac{\partial f}{\partial \kappa} \frac{\partial \kappa}{\partial \epsilon_{kk}^p}} \right] \quad 3.29$$

$$\times \left[3K \frac{\partial f}{\partial J_1} \delta_{ij} + \frac{G}{\sqrt{J_{2D}}} \frac{\partial f}{\partial \sqrt{J_{2D}}} s_{ij} \right]$$

Equations 3.28 and 3.29 are the general constitutive equations for an elastic work-hardening plastic isotropic material (Chen and Baladi 1985). To use these equations, one must first define the loading function f , the functional forms of the elastic moduli K and G , and the hardening parameter κ for the material of interest.

Elastic-Plastic Constitutive Matrix

In the following section, the equations for the elastic-plastic constitutive matrix are formulated. The equations are written in matrix format to render a more compact form of the equations. The development of the elastic-plastic constitutive matrix follows the derivation of Owen and Hinton (1980).

The loading or yield function f for a general work- or strain-hardening elastic-plastic model (Equation 3.2) may be rewritten as:

$$f(\sigma, \kappa) = F(\sigma) - k(\kappa) = 0 \quad 3.30$$

where (in matrix format) σ is the vector of normal and shear stresses and κ is the hardening parameter that controls the expansion of the yield surface.

Recall that in the cap model, the cap itself is the only strain-hardening yield surface; the failure envelope is not a hardening surface. Equation 3.30 may be differentiated to give:

$$df = \frac{\partial f}{\partial \sigma} d\sigma + \frac{\partial f}{\partial \kappa} d\kappa = 0 \quad 3.31$$

or in another form:

$$a^T d\sigma - A d\lambda = 0 \quad 3.32$$

where

$$a^T = \frac{\partial f}{\partial \sigma} = \frac{\partial f}{\partial \sigma_{ij}} \quad 3.33$$

and

$$A = -\frac{1}{d\lambda} \frac{\partial f}{\partial \kappa} d\kappa \quad 3.34$$

Owen and Hinton refer to the vector a as the *flow vector*. The scalar A will be identified as the plastic hardening modulus.

The total strain increment tensor (Equation 3.10) may be written in matrix format as

$$d\epsilon = d\epsilon^e + d\epsilon^p \quad 3.35$$

By substituting for both the elastic and plastic strain increments, i.e., using the matrix equivalents of Equations 3.9 and 3.11, the following expression is obtained:

$$d\epsilon = D^{-1} d\sigma + d\lambda \frac{\partial f}{\partial \sigma} \quad 3.36$$

where D is the matrix of elastic material constants and the inverse of the material response function.

After multiplying Equation 3.36 by $a^T D$ one obtains:

$$a^T D d\epsilon = a^T d\sigma + a^T D a d\lambda \quad 3.37$$

which may be refined further by eliminating $a^T d\sigma$ with the use of Equation 3.32 to produce:

$$a^T D d\epsilon = [A + a^T D a] d\lambda \quad 3.38$$

This leads to an expression for the scalar term $d\lambda$:

$$d\lambda = \frac{a^T D d\epsilon}{[A + a^T D a]} \quad 3.39$$

This term gives the magnitude of the plastic strain increment vector and is the matrix form of Equation 3.27. Note that in the text by Owen and Hinton (1980), this expression was printed incorrectly.

Having defined an expression for $d\lambda$, it may be substituted into Equation 3.36 to give:

$$D^{-1} d\sigma = \left\{ 1 - \frac{d_D^T a}{[A + d_D^T a]} \right\} d\epsilon \quad 3.40$$

where $d_D^T = a^T D$.

Multiplying both sides of Equation 3.40 by D gives:

$$d\sigma = \left\{ D - \frac{D a d_D^T}{[A + d_D^T a]} \right\} d\epsilon \quad 3.41$$

which is an expression for the elastic-plastic incremental stress-strain relation. If we substitute $d_D = D a$, then the elastic-plastic constitutive matrix may be expressed as:

$$D^{ep} = \left\{ D - \frac{d_D d_D^T}{[A + d_D^T a]} \right\} \quad 3.42$$

Plastic Hardening Modulus

The plastic hardening modulus A must now be evaluated for a strain-hardening formulation such as the cap model. If the hardening parameter κ is a function of the plastic strains, i.e.,

$$\kappa = g(\epsilon^P) \quad 3.43$$

then Equation 3.43 may be differentiated to give:

$$d\kappa = \frac{\partial \kappa}{\partial \epsilon^P} d\epsilon^P \quad 3.44$$

Substituting Equation 3.44 into Equation 3.34, substituting for ϵ^p , and rearranging produces:

$$A = -\frac{\partial f}{\partial \kappa} \frac{\partial \kappa}{\partial \epsilon^p} \frac{\partial f}{\partial \sigma} \quad 3.45$$

The plastic hardening modulus A will be dependent upon the functional form of the loading or yield function f and the hardening function used in the cap model.

Cap Model Implemented into JAM

The following section describes the version of the cap model implemented into the finite element code JAM. The functional forms of the equations are outlined, and the cap model is described in more detail.

Two elastic response functions govern the behavior of the model in the elastic regime. The elastic bulk modulus is defined by the following equation

$$K(J_1, \epsilon_{kk}^p) = \frac{K_i}{1 - K_1} \left[1 - K_1 \exp(K_2 \epsilon_{kk}^p) \right] \quad 3.46$$

where K_i = the initial elastic bulk modulus and

K_1 and K_2 are material constants.

The elastic bulk modulus prescribes the unloading moduli in pressure-volume space. The three material constants may be determined from the unloading data obtained during hydrostatic loading tests. The elastic shear modulus is defined by the following equation

$$G(J_{2D}, \epsilon_{kk}^p) = \frac{G_i}{1 - G_1} \left[1 - G_1 \exp(G_2 \epsilon_{kk}^p) \right] \quad 3.47$$

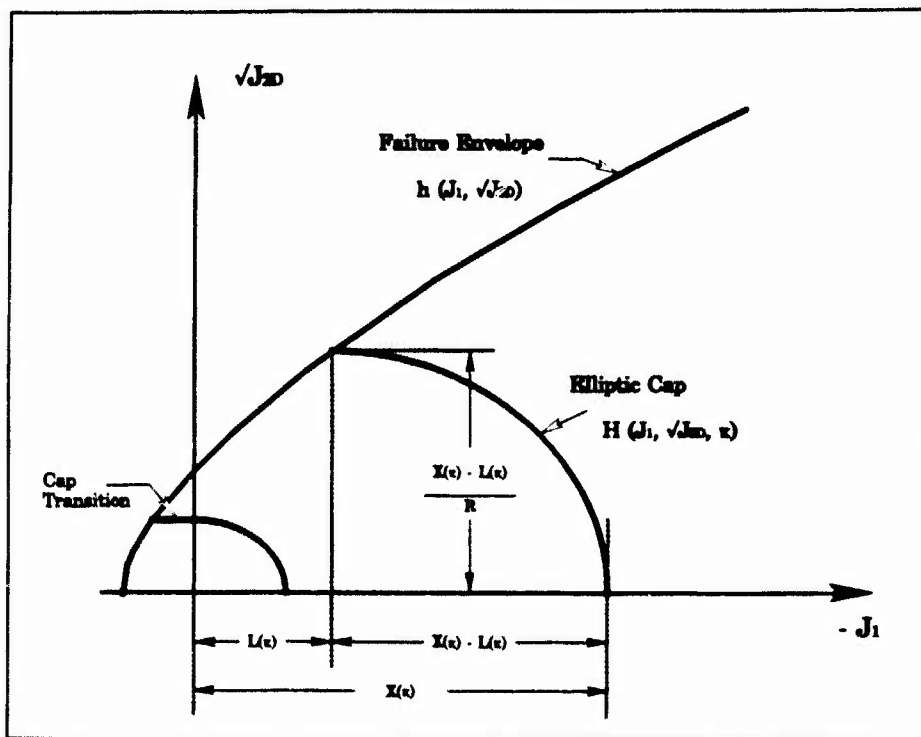
where G_i = the initial elastic shear modulus and

G_1 and G_2 are material constants.

The elastic shear modulus prescribes the unloading moduli in principal stress difference-principal strain difference space. The three material constants may be determined from the unloading shear data of triaxial compression tests.

The constants for the elastic bulk and shear moduli may also be determined from uniaxial strain compression tests, i.e., from the unloading slopes of the stress path ($= 2G/K$) and stress-strain curves ($= K + 4/3 G$).

In the current model, the failure envelope portion of the loading function f is defined by a modified Drucker-Prager failure surface (see Figure 3.1) of the form



3.1. Cap model yield surfaces

$$h(J_1, \sqrt{J_{2D}}) = \sqrt{J_{2D}} - [A - C \exp(BJ_1)] \quad \text{if } J_1 > L(\kappa) \quad 3.48$$

where A , B and C are material constants. These constants may be determined from the locus of triaxial compression failure data plotted in the appropriate stress space. The strain-hardening yield surface or cap is described by the following

$$H(J_1, \sqrt{J_{2D}}, \kappa) = \sqrt{J_{2D}} - \frac{1}{R} \left\{ [X(\kappa) - L(\kappa)]^2 - [J_1 - L(\kappa)]^2 \right\}^{0.5} \quad \text{if } J_1 < L(\kappa) \quad 3.49$$

where $X(\kappa)$ and $L(\kappa)$ define the values of J_1 at the intersection of the cap with the J_1 axis and at the center of the cap, respectively (see Figure 3.1); κ is the hardening parameter, which is equal to the plastic volumetric strain, i.e.,

$$\kappa = \epsilon_{kk}^p \quad 3.50$$

Equations 3.48 and 3.49 also indicate the value of J_1 determines which of the two yield surfaces should be used. R is the ratio of the major to minor axes of the elliptical cap and has the following functional form

$$R[L(\kappa)] = R_i + R_1 \left[1 - \exp\left(R_2\{L(\kappa) - L_0\}\right) \right] \quad 3.51$$

where R_i, R_1, R_2 and L_0 are material constants; L_0 defines the initial location of the cap.

Chen and Baladi (1985) explain that the functional form of the cap was chosen such that the tangent of its intersection with the failure envelope is horizontal. This condition is guaranteed by the following relationship between $X(\kappa)$ and $L(\kappa)$

$$X(\kappa) = L(\kappa) - R h(l(\kappa), \sqrt{J_{2D}}) \quad 3.52$$

where

$$L(\kappa) = \begin{cases} l(\kappa) & \text{if } l(\kappa) < 0 \\ 0 & \text{if } l(\kappa) \geq 0 \end{cases} \quad 3.53$$

The hardening function for this model is defined by

$$\epsilon_{kk}^p = W \left(e^{[D\{X(\kappa) - X_0\}] - 1} - 1 \right) \quad 3.54$$

which may be rewritten in the following form

$$X(\kappa) = \frac{1}{D} \ln \left[\frac{\epsilon_{kk}^p}{W} + 1 \right] + X_0 \quad 3.55$$

where D, W and X_0 are material constants. W establishes the maximum plastic volumetric strain the material can develop; X_0 , like L_0 , defines the initial location of the cap.

As described previously, Drucker's stability postulate places limits on the functional forms of the equations in the cap model. Sandler and Rubin (1979) specify some of those limitations: (a) $Q(J_1)$ must decrease monotonically with increasing values of J_1 ; (b) to avoid work-softening, the functions

$X(\kappa)$ and $L(\kappa)$ must be continuous and monotonically increasing functions and

$$\frac{\partial F}{\partial J_1} \geq 0 \quad \text{and} \quad \frac{\partial F}{\partial \kappa} < 0$$

(c) the cap must extend from the J_1 axis to a point on or below the failure envelope h , i.e.,

$$F[X(\kappa), \kappa] = 0 \quad 3.56$$

and

$$F[L(\kappa), \kappa] \leq Q[L(\kappa)] \quad 3.57$$

(d) within the yield surfaces defined by

$$\sqrt{J_{2D}} < Q(J_1) \quad \text{for } J_1 > L(\kappa) \quad 3.58$$

and

$$\sqrt{J_{2D}} < F(J_1, \kappa) \quad \text{for } L(\kappa) \geq J_1 \geq X(\kappa) \quad 3.59$$

the material response must be isotropic elastic. Sandler and Rubin (1979) explain that if the inequality in Equation 3.57 is true, then a gap exists between the cap H and the failure envelope h and a von Mises type failure surface is used as a transition between the two yield surfaces (Figure 3.1). The yield surface for $J_1 \geq L(\kappa)$ is thus defined by the following expression

$$\sqrt{J_{2D}} = \min \{ F[L(\kappa), \kappa], Q[J_1] \} \quad 3.60$$

In the evaluation of plastic hardening modulus A , one need only be concerned with the functional form of the cap since it is the only hardening surface in the model. In order to evaluate A , each of the three terms in Equation 3.45 must be evaluated. Recalling Equation 3.50, the first term may be expanded as

$$\frac{\partial H}{\partial \kappa} = \frac{\partial H}{\partial X} \frac{\partial X}{\partial \kappa} = \frac{\partial H}{\partial X} \frac{\partial X}{\partial \epsilon_{kk}^p} \quad 3.61$$

Each of these terms is evaluated as

$$\frac{\partial X}{\partial \epsilon_{kk}^p} = \frac{1}{D(\epsilon_{kk}^p + W)} \quad 3.62$$

and

$$\frac{\partial H}{\partial X} = 2(L - X) \quad 3.63$$

Combining the terms gives

$$\frac{\partial H}{\partial \kappa} = \frac{2(L - X)}{D(\epsilon_{kk}^p + W)} \quad 3.64$$

The second term in the expression for A is evaluated as

$$\frac{\partial \kappa}{\partial \epsilon_{ij}^p} = \delta_{ij} \quad 3.65$$

since $\kappa = \epsilon_{kk}^p$. The final term in A can be expanded as

$$\frac{\partial H}{\partial \sigma_{ij}} = \frac{\partial H}{\partial J_1} \delta_{ij} + \frac{s_{ij}}{2\sqrt{J_{2D}}} \frac{\partial H}{\partial \sqrt{J_{2D}}} \quad 3.66$$

Recalling that $s_{ij} \delta_{ij} = 0$ and substituting Equations 3.64-3.66 into Equation 3.45, one gets

$$A = \frac{6(X - L)}{D(\epsilon_{kk}^p + W)} \frac{\partial H}{\partial J_1} \quad 3.67$$

as an expression for A . Simplifying this further by evaluating

$$\frac{\partial H}{\partial J_1} = 2(J_1 - L) \quad 3.68$$

and substituting into Equation 3.67, one obtains the final expression for the

plastic hardening modulus

$$A = \frac{12(X - L)(J_1 - L)}{D(\epsilon_{kk}^p + W)} \quad 3.69$$

Numerical Implementation of the Cap Model

Introduction

The numerical algorithm for the cap model was published by Sandler and Rubin in an attempt "to facilitate the general use of the cap model in dynamic computations, as well as in model fitting" (Sandler and Rubin 1979). The cap model algorithm was designed for use in either finite element or finite difference codes and is applicable to both static and dynamic problems (Chen and Baladi 1985). Of notable foresight on the part of the designers was their use of function statements within the model, which allow substantial changes to be made to the cap model's potential functions with little programming effort. This feature has allowed investigators to simulate a wide variety of natural and man-made materials with high degrees of fidelity between model and material response. Despite the many published variations of the cap model, the original cap model algorithm developed by Sandler and Rubin still forms the foundation of most current cap model algorithms.

The cap model algorithm is essentially an implementation of Equation 3.29. To march the calculation through time, the user must input the stresses σ_{ij} and the location of the cap at time t , which is explicitly defined by the term $l(\kappa)$ and implicitly defined by the hardening parameter κ , and the strain increments from the solution of the field equations for the current time step $\Delta t d\epsilon_{ij}$. The cap model returns the new stresses $\sigma_{ij}^{\Delta t}$ and the updated cap location and hardening parameter $l(\kappa^{\Delta t})$ and $\kappa^{\Delta t}$ at time $t + \Delta t$. A given strain increment may invoke four different types of stress paths that coincide with four different algorithms within the cap model itself:

- (a) an elastic algorithm,
- (b) a failure envelope algorithm,
- (c) a hardening cap algorithm, or
- (d) a tension cutoff algorithm.

In the following text, a description of the four numerical algorithms is provided. The descriptions are based upon previous descriptions by Baladi and Akers (1981), Chen and Baladi (1985), Sandler and Rubin (1979), and Meier (1989). To simplify the presentation, a description of the cap model's response in the tensile regime will be deferred to the later part of this section.

Elastic algorithm

To start the numerical procedure, it is assumed that the given strain increments produce an entirely elastic stress path. A set of elastic trial stresses are calculated from

$$E_{J_1} = {}^t J_1 + 3K {}^{t+\Delta t} d\epsilon_{kk} \quad 3.70$$

and

$$E_{s_{ij}} = {}^t s_{ij} + 2G {}^{t+\Delta t} de_{ij} \quad 3.71$$

The elastic trial stresses are tested with respect to the tension cutoff, the failure envelope, and then the cap. If these surfaces are not violated by the trial stresses, the actual stress path is an elastic path, and the new stresses are the elastic trial stresses, i.e., ${}^{t+\Delta t} J_1 = E_{J_1}$ and ${}^{t+\Delta t} s_{ij} = E_{s_{ij}}$.

Failure envelope algorithm

If the following conditions exist when the elastic trial stresses are tested with respect to the failure envelope,

$$E_{J_1} \geq L({}^t \kappa)$$

$$h(E_{J_1}, \sqrt{E_{J_{2D}}}) = \sqrt{E_{J_{2D}}} - Q(E_{J_1}) \geq 0$$

then the elastic trial stresses have violated the failure envelope, and the given strain increment must be a combination of elastic and plastic strains. The trial stresses must be corrected such that (a) the final stress state falls on the failure surface and satisfies the following relation

$$h({}^{t+\Delta t} J_1, \sqrt{{}^{t+\Delta t} J_{2D}}) = 0 \quad 3.72$$

and (b) the resulting elastic and plastic strain increments add up to the given strain increments ${}^{t+\Delta t} d\epsilon_{ij}$.

The mathematical statement that requires the final stresses to lie on the fixed failure surface is given as

$$dh = \frac{\partial h}{\partial \sigma_{ij}} d\sigma_{ij} = 0 \quad 3.73$$

Assuming small strain increments, Equation 3.73 can be numerically approximated by the following expression

$$dh = \sqrt{E J_{2D}} - \sqrt{{}^{t+\Delta t} J_{2D}} - Q({}^E J_1) + Q({}^{t+\Delta t} J_1) \quad 3.74$$

which reduces to

$$dh = \sqrt{E J_{2D}} - Q({}^E J_1) \quad 3.75$$

since the final stress point must lie on the failure surface, i.e.,

$$\sqrt{{}^{t+\Delta t} J_{2D}} - Q({}^{t+\Delta t} J_1) = 0 \quad 3.76$$

Equation 3.75 may be substituted into Equation 3.73 and expanded in the following manner

$$\begin{aligned} \sqrt{E J_{2D}} - Q({}^E J_1) &= \frac{\partial h}{\partial \sigma_{ij}} d\sigma_{ij} \\ &= \left[\frac{\partial h}{\partial J_1} \frac{\partial J_1}{\partial \sigma_{ij}} + \frac{\partial h}{\partial \sqrt{J_{2D}}} \frac{\partial \sqrt{J_{2D}}}{\partial \sigma_{ij}} \right] d\sigma_{ij} \quad 3.77 \\ &= \frac{\partial h}{\partial J_1} dJ_1 + \frac{1}{2\sqrt{J_{2D}}} \frac{\partial h}{\partial \sqrt{J_{2D}}} E_{s_{ij}} ds_{ij} \end{aligned}$$

where $dJ_1 = {}^E J_1 - {}^t J_1$ and $ds_{ij} = E_{s_{ij}} - {}^t s_{ij}$. From Equations 3.70 and 3.71, we know that $dJ_1 = 3K {}^{t+\Delta t} d\epsilon_{kk}$ and $ds_{ij} = 2G {}^{t+\Delta t} d\epsilon_{ij}$, and these expressions may be substituted into Equation 3.77 to give

$$\begin{aligned} \sqrt{E J_{2D}} - Q({}^E J_1) &= 3K {}^{t+\Delta t} d\epsilon_{kk} \frac{\partial h}{\partial J_1} \\ &+ \frac{G}{\sqrt{J_{2D}}} \frac{\partial h}{\partial \sqrt{J_{2D}}} E_{s_{ij}} {}^{t+\Delta t} d\epsilon_{ij} \end{aligned} \quad 3.78$$

If we substitute Equation 3.78 into the numerator of Equation 3.27 and recognize that $h = f$, $\frac{\partial h}{\partial J_1} = -\frac{\partial Q}{\partial J_1}$, $\frac{\partial h}{\partial \sqrt{J_{2D}}} = 1$, and $\frac{\partial h}{\partial \kappa} = 0$ for the fixed failure envelope, an expression for $d\lambda$ may be written as

$$d\lambda = \frac{\sqrt{E_{J_{2D}}} - Q(E_{J_1})}{9K \left[\frac{\partial Q}{\partial J_1} \right]^2 + G} \quad 3.79$$

Substituting the above expression into Equation 3.20, the final expression for the plastic strain increment is obtained

$$d\epsilon_{kk}^P = -3 \left[\frac{\sqrt{E_{J_{2D}}} - Q(E_{J_1})}{9K \left[\frac{\partial Q}{\partial J_1} \right]^2 + G} \right] \frac{\partial Q}{\partial J_1} \quad 3.80$$

An expression for ${}^{i+\Delta i}J_1$ may be developed in the following manner

$$\begin{aligned} {}^{i+\Delta i}J_1 &= {}^iJ_1 + 3K d\epsilon_{kk}^e \\ &= {}^iJ_1 + 3K {}^{i+\Delta i}d\epsilon_{kk} - 3K d\epsilon_{kk}^P \quad 3.81 \\ &= E_{J_1} - 3K d\epsilon_{kk}^P \end{aligned}$$

where $d\epsilon_{kk}^P$ is defined by Equation 3.80. A "tentative" value of ${}^{i+\Delta i}J_1$ may be calculated from Equation 3.81; this value is tentative because it must be tested against the current position of the cap, which is defined by the value of $L({}^i\kappa)$.

If ${}^{i+\Delta i}J_1 < L({}^i\kappa)$, which indicates the stress point has violated the cap, then corner coding is required, i.e., the cap must intersect the failure envelope forming a corner, and the value of ${}^{i+\Delta i}J_1$ must be adjusted. Adhering to the imposed conditions of normality, a stress state lying on the failure envelope produces dilatant plastic volumetric strains. Since cap expansion can only result from compressive plastic volumetric strains, the cap is stationary, and the new stress state can not move beyond the intersection of the cap and the failure envelope. Thus, the final stress state is ${}^{i+\Delta i}J_1 = L({}^i\kappa)$, and the updated hardening parameter is ${}^{i+\Delta i}\kappa = {}^i\kappa$.

If ${}^{t+\Delta t}J_1 > L({}^t\kappa)$, then the final stresses will depend upon the form of the hardening function. Equation 3.7 is the simplest form of the hardening function to use because it only permits plastic volumetric compaction, i.e., the cap is only allowed to expand. As in the above case, a stress state lying on the failure envelope produces dilatant plastic volumetric strains. Since the hardening function defined by Equation 3.7 prescribes no cap movement due to dilatant volumetric strains, the cap is stationary. Thus, the final stress state is ${}^{t+\Delta t}J_1$, i.e., no adjustment is required, and the updated hardening parameter is ${}^{t+\Delta t}\kappa = {}^t\kappa$. If the hardening function takes the form of Equation 3.6, which allows the cap to expand and contract, the cap is adjusted (in this case contracted) to a position prescribed by

$${}^{t+\Delta t}l = {}^tl + \left. \frac{\partial l}{\partial \epsilon_{kk}^p} \right|_{{}^tl} d\epsilon_{kk}^p \quad 3.82$$

and a tentative value of ${}^{t+\Delta t}\kappa$ is obtained. The new position of the cap must be compared to the value of ${}^{t+\Delta t}J_1$. If the cap has contracted such that ${}^{t+\Delta t}J_1 < L({}^{t+\Delta t}\kappa) = {}^{t+\Delta t}l$, both ${}^{t+\Delta t}\kappa$ and ${}^{t+\Delta t}J_1$ must be adjusted such that ${}^{t+\Delta t}J_1 = L({}^{t+\Delta t}\kappa) = {}^{t+\Delta t}l$. This is accomplished by starting with the following relation

$$EJ_1 - 3Kd\epsilon_{kk}^p = {}^{t+\Delta t}J_1 = L({}^{t+\Delta t}\kappa) = {}^{t+\Delta t}l + \left. \frac{\partial l}{\partial \epsilon_{kk}^p} \right|_{{}^{t+\Delta t}l} d\epsilon_{kk}^p \quad 3.83$$

eliminating $d\epsilon_{kk}^p$, which is the third unknown, by substituting the following

$$d\epsilon_{kk}^p = \frac{EJ_1 - {}^tl}{\left. \frac{\partial l}{\partial \epsilon_{kk}^p} \right|_{{}^tl} + 3K} \quad 3.84$$

from which one can show that

$$\begin{aligned}
 {}^{t+\Delta t}J_1 &= E_{J_1} - 3K \frac{E_{J_1} - {}^t l}{\left. \frac{\partial l}{\partial \epsilon_{kk}^p} \right|_{{}^t l}} + 3K \\
 &= \frac{E_{J_1} \left[\left. \frac{\partial l}{\partial \epsilon_{kk}^p} \right|_{{}^t l} + 3K \right] - 3K(E_{J_1} - {}^t l)}{\left. \frac{\partial l}{\partial \epsilon_{kk}^p} \right|_{{}^t l}} + 3K
 \end{aligned} \tag{3.85}$$

which in turn simplifies to

$${}^{t+\Delta t}l = l({}^{t+\Delta t}\kappa) = {}^{t+\Delta t}J_1 = \frac{\left. \frac{\partial l}{\partial \epsilon_{kk}^p} \right|_{{}^t l} E_{J_1} + 3K {}^t l}{\left. \frac{\partial l}{\partial \epsilon_{kk}^p} \right|_{{}^t l}} + 3K \tag{3.86}$$

Having calculated the final value of ${}^{t+\Delta t}J_1$, we must calculate the new components of the deviatoric stress tensor ${}^{t+\Delta t}s_{ij}$. The expressions for ${}^{t+\Delta t}s_{ij}$ are developed below.

Recognizing the path independence of linear elastic constitutive equations, we can write

$${}^{t+\Delta t}s_{ij} = {}^t s_{ij} + 2G de_{ij}^e \tag{3.87}$$

Substituting Equation 3.71 into Equation 3.87 and performing a simple manipulation one obtains

$${}^{t+\Delta t}s_{ij} = E s_{ij} - 2G de_{ij}^p \tag{3.88}$$

Recalling Equation 3.22 and recognizing that $\frac{\partial f}{\sqrt{J_{2D}}} = 1$, we can write

$$de_{ij}^p = \frac{d\lambda}{2\sqrt{J_{2D}}} s_{ij} \tag{3.89}$$

which can be substituted into Equation 3.88 giving

$${}^{t+\Delta t}S_{ij} = E_{S_{ij}} - \frac{d\lambda G}{\sqrt{{}^{t+\Delta t}J_{2D}}} {}^{t+\Delta t}S_{ij} \quad 3.90$$

After rearranging the above equation one obtains

$${}^{t+\Delta t}S_{ij} \left(1 + \frac{d\lambda G}{\sqrt{{}^{t+\Delta t}J_{2D}}} \right) = E_{S_{ij}} \quad 3.91$$

Squaring each side of Equation 3.91 and multiplying by $\frac{1}{2}$ produces

$${}^{t+\Delta t}J_{2D} \left(1 + \frac{d\lambda G}{\sqrt{{}^{t+\Delta t}J_{2D}}} \right)^2 = E_{J_{2D}} \quad 3.92$$

Taking the square root of each side and rearranging terms, one obtains

$$\frac{\sqrt{{}^{t+\Delta t}J_{2D}}}{\sqrt{E_{J_{2D}}}} = 1 + \frac{d\lambda G}{\sqrt{{}^{t+\Delta t}J_{2D}}} \quad 3.93$$

Replacing the right-hand side of Equation 3.93 with the expressions in Equation 3.91, one obtains

$$\frac{\sqrt{{}^{t+\Delta t}J_{2D}}}{\sqrt{E_{J_{2D}}}} = \frac{{}^{t+\Delta t}S_{ij}}{E_{S_{ij}}} \quad 3.94$$

which may be rewritten for our use as

$${}^{t+\Delta t}S_{ij} = \frac{\sqrt{{}^{t+\Delta t}J_{2D}}}{\sqrt{E_{J_{2D}}}} E_{S_{ij}} \quad 3.95$$

to calculate the new deviator stress tensor components.

Cap algorithm

If the failure envelope is not violated by the elastic trial stresses, the trial stresses are checked against the loading function for the cap. If the following conditions exist

$$H(EJ_1, \sqrt{EJ_{2D}}, {}^t\kappa) > 0$$

and

$$EJ_1 < X({}^t\kappa)$$

or

$$EJ_1 \leq L({}^t\kappa)$$

then the cap algorithm is invoked and the position of the cap is adjusted until

$$H({}^{t+\Delta t}J_1, \sqrt{{}^{t+\Delta t}J_{2D}}, {}^{t+\Delta t}\kappa) = 0$$

An iterative procedure is used in the cap algorithm. To start the procedure, a trial value of $dl^{(i)}$ is assumed in order to calculate a new trial cap position ${}^{t+\Delta t}l^{(i)} = l^{(i)} = {}^t l + dl^{(i)}$, where the superscript i denotes an iterative value. In addition, trial values of $\kappa^{(i)}$, $L(\kappa^{(i)})$, $X(\kappa^{(i)})$, and $d\epsilon_{kk}^p$ are computed. Finally, a trial value of J_1 is computed from the following relation

$$J_1^{(i)} = EJ_1 - 3Kd\epsilon_{kk}^p \quad 3.96$$

If $J_1^{(i)} \leq X(\kappa^{(i)})$, a smaller value of $dl^{(i)}$ is assumed. If

$J_1^{(i)} \geq L(\kappa^{(i)})$, a larger value of $dl^{(i)}$ is assumed. This process is carried on until the condition $L(\kappa^{(i)}) \leq J_1^{(i)} < X(\kappa^{(i)})$ is satisfied. The final value of l is one which satisfies the following equation to some desired accuracy

$$\sqrt{{}^{t+\Delta t}J_{2D}} + \frac{Gd\epsilon_{kk}^p}{3\xi} = \sqrt{EJ_{2D}} \quad 3.97$$

where

$$\xi = - \left. \frac{\partial F}{\partial J_1} \right|_{J_1^{(i)}, \kappa^{(i)}} = - \left. \frac{\partial F}{\partial J_1} \right|_{J_1^{(i)}, l^{(i)}} \quad 3.98$$

The derivation of Equation 3.97 is outlined in the following text.

If we start with Equation 3.22 and substitute for $d\lambda$ using Equation 3.20, one obtains

$$de_{ij}^P = s_{ij} d\epsilon_{kk}^P \left[\frac{1}{6\sqrt{J_{2D}}} \frac{\partial H}{\partial \sqrt{J_{2D}}} \right] / \frac{\partial H}{\partial J_1} \quad 3.99$$

Recognizing that $f = H$, $\partial H / \partial \sqrt{J_{2D}} = 1$ and $\partial H / \partial J_1 = -\partial F / \partial J_1 = \xi$, we can rewrite Equation 3.99 as

$$de_{ij}^P = s_{ij} \frac{d\epsilon_{kk}^P}{6\xi\sqrt{J_{2D}}} \quad 3.100$$

Substituting the above into Equation 3.88 and rearranging gives

$$s_{ij} \left[1 + \frac{G d\epsilon_{kk}^P}{3\xi\sqrt{J_{2D}}} \right] = E s_{ij} \quad 3.101$$

Performing the same operations on the above equation as was used on Equations 3.91-3.93, one obtains Equation 3.97.

The solution of Equation 3.97 is obtained through the use of an iterative convergence routine known as the modified regula falsi method (Sandler and Rubin 1979). A dimensionless function $P(l)$ is defined as

$$P(l) = \begin{cases} \frac{l(\kappa) - J_1^{(i)}}{l(\kappa) - X(\kappa)} & \text{if } J_1^{(i)} \leq X(\kappa) \\ \frac{\sqrt{E J_{2D}} - \sqrt{l \cdot \Delta l J_{2D}^{(i)}} - \frac{G d\epsilon_{kk}^P}{3\xi}}{\sqrt{E J_{2D}} + \sqrt{l \cdot \Delta l J_{2D}^{(i)}} + \frac{G d\epsilon_{kk}^P}{3\xi}} & \text{if } X(\kappa) < J_1^{(i)} < L(\kappa) \\ \frac{X(\kappa) - J_1^{(i)}}{L(\kappa) - X(\kappa)} & \text{if } J_1^{(i)} \geq L(\kappa) \end{cases} \quad 3.102$$

where the solution $P(l) = 0$ is also the solution of Equation 3.97. If we can show that $E J_1 < l \cdot \Delta l J_{2D}^{(i)} < l$, then $P(l)$ is bounded and monotonic in the strict sense, and the solution $P(l) = 0$ is unique and can be found to any

desired degree of accuracy (Sandler and Rubin 1979). An expression for the degree of accuracy or tolerated error is given by

$$\left| \sqrt{E_{J_{2D}}} - \sqrt{{}^{t+\Delta t}J_{2D}} - \frac{G d\epsilon_{kk}^p}{3\xi} \right| < N Q [X(\kappa)] \quad 3.103$$

where a tolerance of $N/h(\infty, \sqrt{J_{2D}}) = 10^{-3}$ (in dimensionless format) is typically used.

To show that $E_{J_1} < {}^{t+\Delta t}l^{(i)} < {}^t l$, we must recognize that $J_1^{(i)} < L({}^t \kappa)$ must be true, since it is a condition for invoking the cap algorithm. In addition, since

$$J_1^{(i)} = E_{J_1} - 3K d\epsilon_{kk}^p \quad 3.104$$

we know that $J_1^{(i)} > E_{J_1}$, because the plastic volumetric strain increment is negative during volumetric compaction, i.e., when the cap expands. This means that the final value of ${}^{t+\Delta t}J_1$ must lie in the range

$$E_{J_1} < {}^{t+\Delta t}J_1 < L({}^t \kappa)$$

Now let us determine the lower limit of ${}^{t+\Delta t}J_1^{(i)}$, which will lead us to the lower limit of ${}^{t+\Delta t}l^{(i)}$. The cap exhibits its furthest expansion when E_{J_1} is at the intersection of the cap and the failure envelope. When the cap is in this position, ${}^{t+\Delta t}J_1 = L({}^{t+\Delta t} \kappa) = E_{J_1}$, which implies that the lower bound of ${}^{t+\Delta t}l^{(i)}$ is

$${}^{t+\Delta t}l = l({}^{t+\Delta t} \kappa) = L({}^{t+\Delta t} \kappa) = E_{J_1}$$

The upper bound of ${}^{t+\Delta t}l^{(i)}$ is simply the value at time t , i.e., ${}^{t+\Delta t}l = {}^t l$. Combining these expressions, the range of ${}^{t+\Delta t}l^{(i)}$ must be

$$E_{J_1} < {}^{t+\Delta t}l^{(i)} < {}^t l$$

With the above conditions satisfied, the solution to Equation 3.97 may be obtained. This concludes the description of the cap algorithm. A description of the cap model's response in the tensile regime follows.

Tensile algorithm

Sandler and Rubin (1979) recognized that soil tensile data is seldom obtained in the laboratory and therefore dealt with tensile behavior in a simple manner. They also cautioned potential users of the simplistic nature of the cap model in the tension regime. A tension failure response is invoked if

$E J_1 > T$, where T is the tension cutoff or limit. Sandler and Rubin recommended that the final stresses be defined as ${}^{t+\Delta t} J_1 = T$ and ${}^{t+\Delta t} s_{ij} = 0$ when the tension cutoff is exceeded. For materials using the definition of the hardening parameter defined by Equation 3.6, the plastic volumetric strain is defined by

$$d\epsilon_{kk}^p = d\epsilon_{kk} + \frac{E J_1 - {}^t J_1}{3K} \quad 3.105$$

and an updated hardening parameter is determined. If the tension cutoff is not exceeded but $E J_1 > 0$, i.e., the elastic trial stress still lies in the tension regime, the stress state must be checked against both the failure envelope and the von Mises transition using the following inequality

$$\sqrt{E J_{2D}} \geq \min \{ Q(E J_1), F[L({}^t \kappa), {}^t \kappa] \}$$

Stress states violating the von Mises transition must be returned to that surface using the same logic implemented for the failure envelope. Stress states lying on the von Mises transition will produce no plastic volumetric strains due to the imposed normality conditions. In addition, the von Mises transition is fixed because the cap hardening surface does not expand.

Implementation of Cap Model into JAM

Two basic operations that are associated with elastic-plastic material models must be performed in most implicit finite element codes: (1) the construction of the elastic-plastic constitutive matrix and (2) the calculation of the residual forces. The purpose of this section is to explain how these two operations were affected by the implementation of the cap model. The later operation will be considered first since it is a straight forward process.

After the strain increments at time $t + \Delta t$ are obtained from the solution of the field equations, the stresses at time $t + \Delta t$ in each element are calculated. The residual forces at time $t + \Delta t$ are then calculated based on the stress states in the elements. In this operation, no substantial changes are required in the cap model subroutines; hence, the implementation is rather simple.

However, three components, the elastic constitutive matrix D , the plastic hardening modulus A , and the flow vector a , are required to calculate the elastic-plastic constitutive matrix D^{ep} . The calculation of the elastic constitutive matrix is simple and needs no further discussion. In JAM, a modified cap-model subroutine calculates and returns values for the flow vector and the plastic hardening modulus. This subroutine first determines which of four possible regions or surfaces a stress point resides in or on, i.e., an elastic

region, the failure surface, the cap, or the tension cutoff. The plastic hardening modulus is nonzero only when the stress point falls on the cap since it is the only hardening surface. In this case, the plastic hardening modulus is calculated using Equation 3.69. The flow vector is calculated by numerically evaluating Equation 3.66 when the stress state lies on the failure surface, the cap, or the tension cutoff.

To complete the implementation, one must provide the model access to the material constants and an array to store the location of the cap for each numerical integration point.

Verification

To insure that the cap model was correctly incorporated into the finite element program JAM, several laboratory stress- and strain-path tests were numerically simulated. These calculations were compared to the output from a cap model driver (Chen and Baladi 1985) exercised over the same laboratory stress and strain paths. The two programs should produce similar if not identical results.

The following tests and strain paths were simulated: a hydrostatic compression test with one load/unload cycle, a set of constant radial stress triaxial compression tests, a set of constant mean normal stress tests, a uniaxial strain (K_0) test with one load/unload cycle, and finally a test with a K_0 load/constant axial strain (BX) unload cycle. To simulate the tests with the finite element program, a single element was loaded under the appropriate boundary conditions. Several loading increments were utilized during each calculation, and a convergence tolerance of 1 percent was satisfied at the end of each increment. The output at the end of each increment is represented by a symbol on the comparison plots.

The simulated hydrostatic loading test consisted of an applied loading to a pressure level of 250 MPa, followed by an unloading to zero pressure. This calculation exercised the logic and code affecting both the cap movements and the elastic algorithms within the model and finite element program. The finite element and cap model driver results are compared in Figure 3.2. Output from the finite element program matches the cap model driver with no noticeable errors.

Four constant radial stress triaxial compression tests at radial stresses of 25, 50, 100, and 150 MPa were simulated. Loading was terminated prior to reaching the ultimate failure surface, and unloading results were acquired for only three of the four calculations. The values of principal stress difference calculated by the finite element program were less than those of the cap model driver (Figure 3.3). The magnitude of the errors decreased when a larger number of increments was applied.

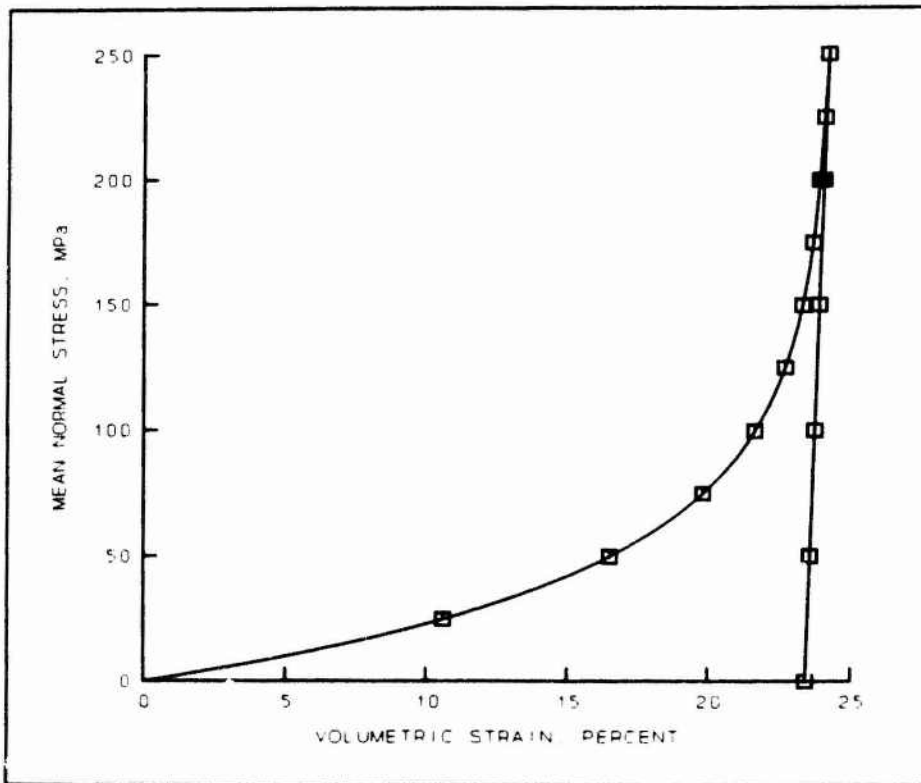


Figure 3.2. Simulated hydrostatic loading stress-strain response

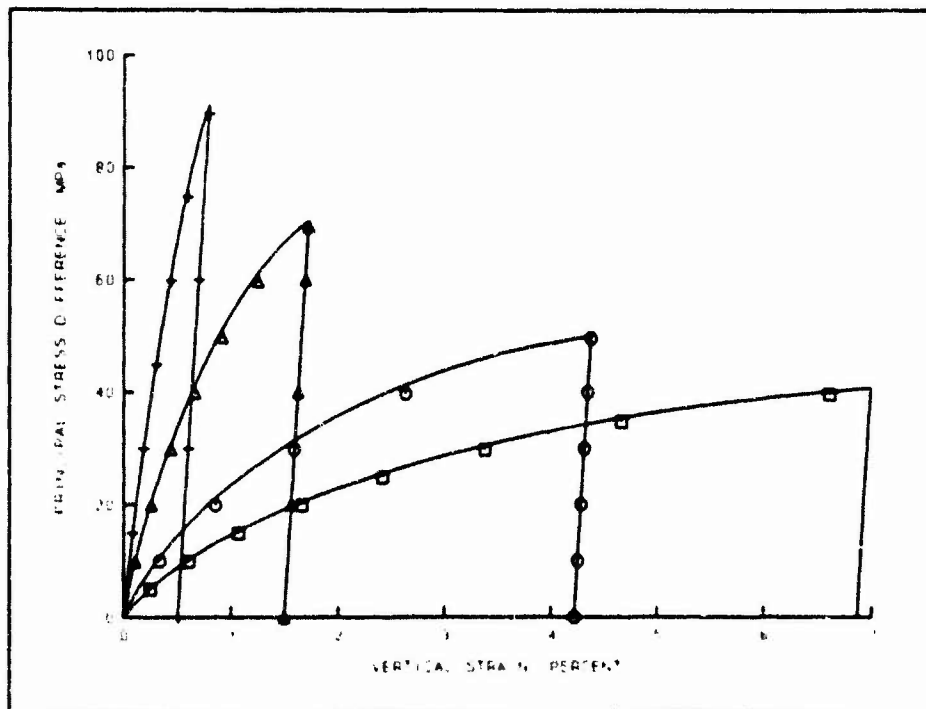


Figure 3.3. Simulated triaxial compression stress-strain response

Four constant mean normal stress tests at confining pressures of 25, 50, 100, and 150 MPa were simulated. As with the simulated triaxial compression

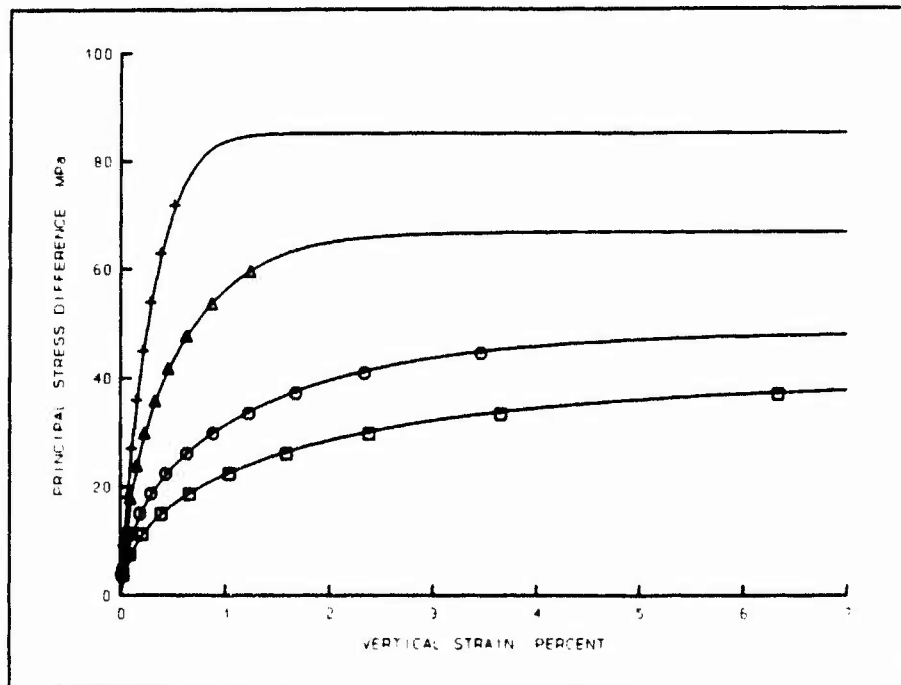


Figure 3.4. Simulated stress-strain response of constant mean normal stress tests

sion tests, loading was terminated prior to reaching the ultimate failure surface; unloading results were not acquired. The finite element and cap model driver results are compared in Figure 3.4. Errors in the stresses calculated by the finite element program were less than those in the simulated triaxial compression tests (Figure 3.3).

The simulated K_0 test consisted of an applied loading to a vertical strain level of 20 percent, followed by an unloading to a small value of vertical stress. In this calculation, the finite element simulation was conducted with a displacement controlled boundary condition. This type of loading should produce an exact match between the finite element program and the cap model driver since no strain increment iterations are required in the finite element program. The calculated K_0 stress-strain response is plotted in Figure 3.5 and the stress path response in Figure 3.6. There are no noticeable differences between the two calculations.

A K_0 load/BX unload test was also simulated with a displacement controlled boundary condition. The test consisted of an applied loading to 20 percent axial strain, followed by an unloading to a small value of radial stress (Figure 3.7). In this calculation, the corner coding of the cap model was exercised as the stress path unloaded along the failure envelope (Figure 3.8). The calculated results suggest a proper implementation of this logic.

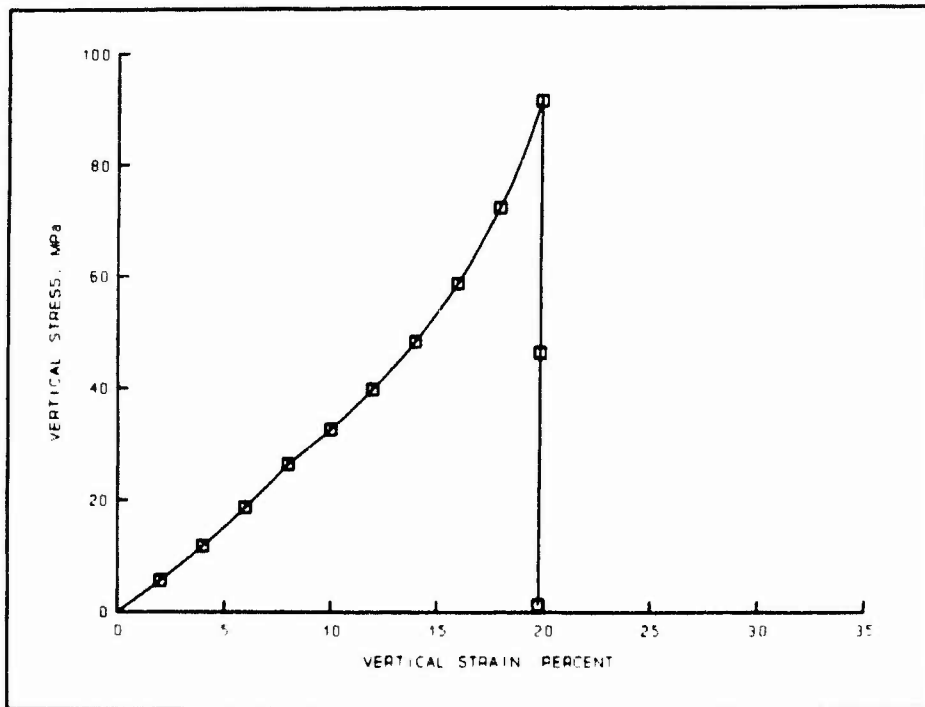


Figure 3.5. Stress-strain response of simulated UX test

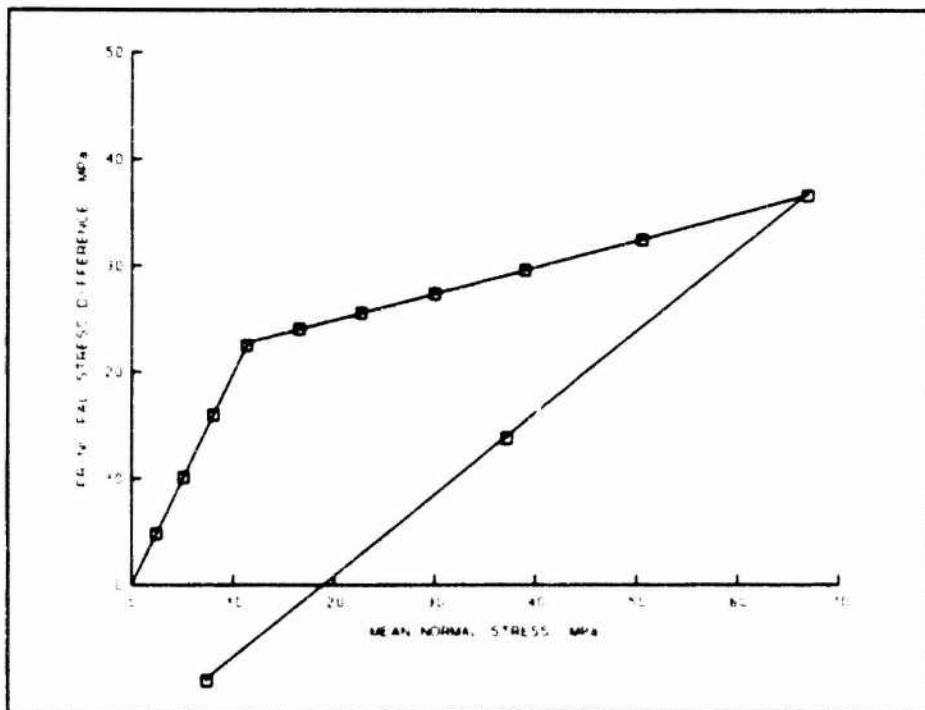


Figure 3.6. Stress path from simulated UX test

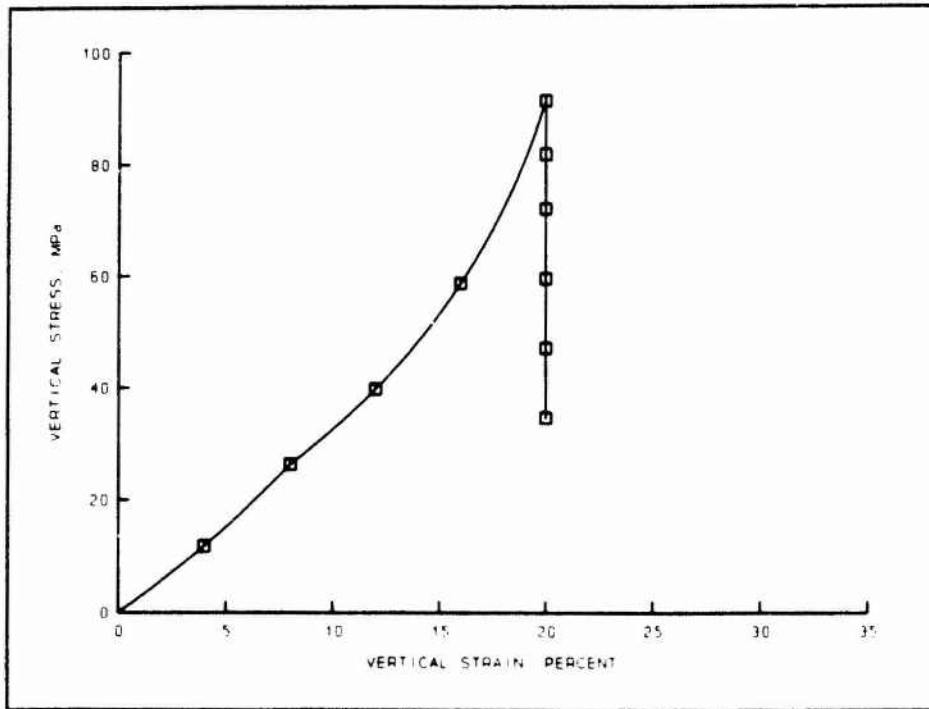


Figure 3.7. Stress-strain response of simulated UX/BX test

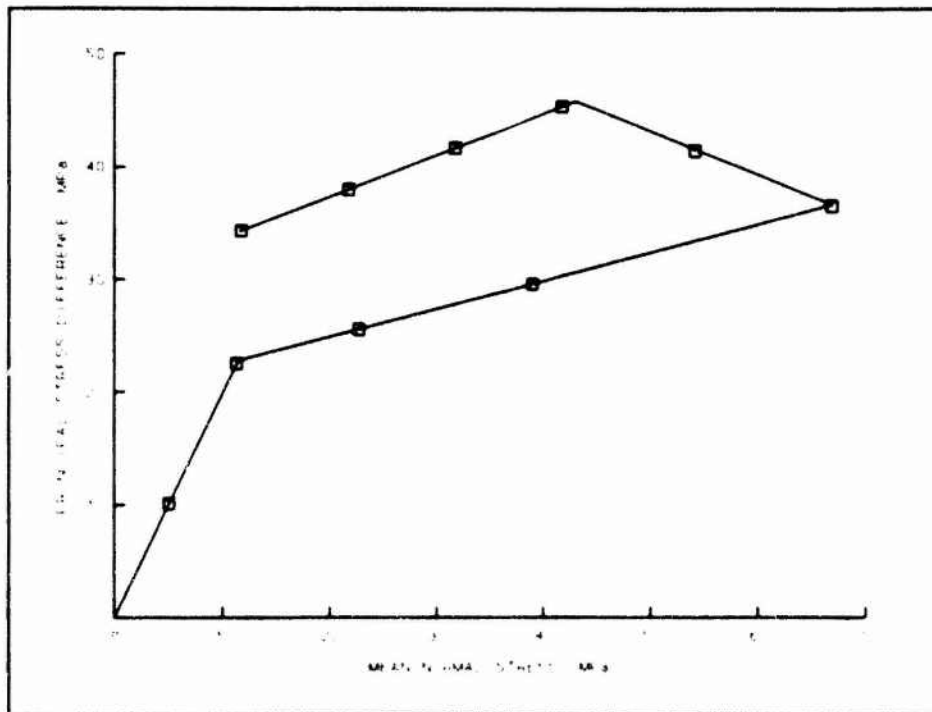


Figure 3.8. Stress path from simulated UX/BX test

Summary

The features of the cap model and the relevant equations were documented in this chapter. In addition, the steps required to implement the cap model into the FE code were summarized. The implementation of the cap model was verified by comparing the output from the FE code and a driver for the cap model.

4 Equations of State for Air, Water, and Solids

Introduction

The materials of interest to this investigation include partially-saturated soil- and rock-like geomaterials and man-made concretes, grouts, and grout-cretes. As outlined in Chapter 2, the equations developed from the Biot theory require an expression for the bulk modulus of the pore fluid and the grain solids. To determine the bulk modulus of the pore fluid, the concept of a homogeneous pore fluid will be adopted to treat partially-saturated materials. This investigation will assume that the liquid within the pore space is water and the gas within the pore space is air. Thus, the pore fluid will be regarded as a compressible mixture of air and water. Based on the equations of state (EOS) for air and water, we will develop equations for the bulk modulus of this air-water mixture. The grain solids will be treated as either linear or nonlinear elastic materials or as nonlinear hysteretic materials; each method for calculating the bulk modulus of the grain solids will be described.

Equation of State for Water

Over the pressure range of interest to this investigation, i.e., 0 to 600 MPa, water has a finite compressibility and should be treated as a nonlinear elastic compressible material. The compressibility of water is depicted in Figure 4.1 as a plot of pressure versus volume strain. The reader should note that at 600 MPa the volume strain of water is nominally 14 percent. The bulk modulus or compressibility of water was evaluated from the Walker-Sternberg EOS for water (Walker and Sternberg 1965), which is valid for pressure levels of up to 50 GPa. The EOS expresses the water pressure as an analytical function of the density and the internal energy of the water. For this investigation, the energy dependent terms in the EOS were not included due to the assumed quasi-static and isothermal nature of the intended calculations. Without the energy terms, the EOS is expressed as

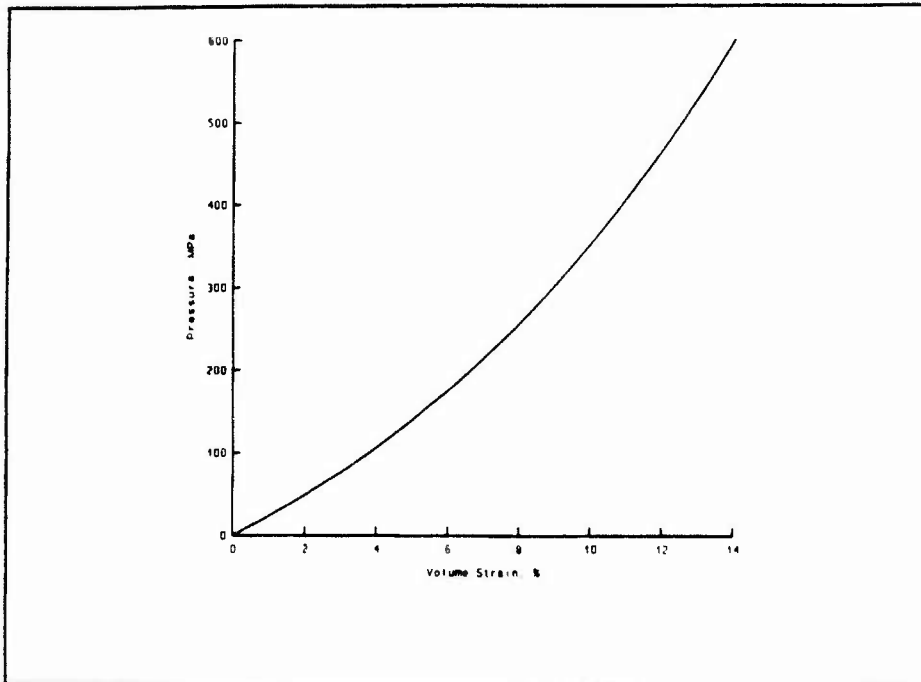


Figure 4.1. Pressure versus volume strain response of water

$$P = \rho f_1 + \rho^3 f_2 + \rho^5 f_3 + \rho^7 f_4 - P_0 \quad 4.1$$

where P is the pressure in the water, ρ is the density of the water, f_i are material constants and P_0 is the initial pressure. If we define volumetric strain as

$$\epsilon_{kk} = 1 - \frac{\rho_0}{\rho} \quad 4.2$$

then the bulk modulus of water may be expressed as

$$K_w = \frac{dP}{d\epsilon_{kk}} = \frac{\rho^2}{\rho_0} \frac{dP}{d\rho} \quad 4.3$$

Substituting Equation 4.1 into Equation 4.3, one obtains the final expression for the bulk modulus of water as a function of density

$$K_w = \frac{1}{\rho_0} \left(\rho^2 f_1 + 3\rho^4 f_2 + 5\rho^6 f_3 + 7\rho^8 f_4 \right) \quad 4.4$$

In the FE program, pressure is the known quantity, not density. Since the EOS expresses pressure and bulk modulus as a function of density, Newton's method was used to calculate the density for a given pressure, then the bulk modulus was calculated.

Air-Water Compressibility

Background

The concept of a homogeneous pore fluid (HPF) was first introduced by Chang and Duncan (1977). In using their concept, one assumes that a three-phase material containing air, water, and solids may be replaced with a two-phase material containing a compressible pore fluid and solids. A partially-saturated material is transformed into a fully-saturated material with a HPF. Effective stress is calculated in the same manner as for a fully-saturated material, and the modulus of the pore fluid is calculated based on the modulus or compressibility of an air-water mixture. The concept is applicable to materials with saturation levels greater than 85 percent. At these levels of saturation, the air should be in the form of occluded bubbles uniformly distributed throughout the water, and the air and water pressures should be identical. At lower saturation levels, one can not guarantee that the air and water pressures will be the same.

The compressibility of air-water mixtures has been studied by several investigators. Bishop and Eldin (1950) examined non-zero total-stress friction angles measured during undrained shear tests. They attributed the observed behavior to incomplete saturation of test specimens. Using Boyle's and Henry's Laws, they developed expressions for the compressibility of an air-water mixture without accounting for surface tension effects.

Schuurman (1966) reviewed the work of previous investigators and concluded that surface tension effects must be included in an air-water compressibility formulation. Schuurman claimed to be the first to attempt such a formulation. Schuurman assumed that at saturation levels greater than 85 percent, the air existed in the form of bubbles. However, to account for surface tension, the radius of the air bubbles was required, yet little if any experimental data was available to provide this necessary information. Schuurman's formulation also differed from that of Bishop in that he wrote his expressions in terms of the current volume of air as opposed to the original volume, and he assumed the water was incompressible.

Fredlund (1976) also developed an expression for the compressibility of an air-water mixture using a formulation in which the water had a finite compressibility. He accounted for surface tension in a manner that did not require a knowledge of air bubble sizes by using a parameter for air-water pressures similar to Skempton's B parameter, which could be evaluated experimentally. Fredlund also interpreted the mixture volume in the expression for compressibility as the volume of water plus free air as compared to water plus total air.

Chang and Duncan (1977) based their expressions for the compressibility of an air-water mixture on the equations of Schuurman. Like Schuurman, they included surface tension effects in their formulation and assumed the water was incompressible.

Alonso and Lloret (1982) reviewed the work of previous investigators, compared the compressibility curves of each, and formulated their own expressions for the compressibility of an air-water mixture. They assumed a finite compressibility for water and accounted for surface tension in the same manner as Fredlund.

In summary, there are significant differences in the equations developed by several investigators for air-water mixtures. For this reason, equations for the compressibility of an air-water mixture will be developed in this chapter. Prior to developing the equations, a brief description of the appropriate physical laws will be provided.

Boyle's and Henry's laws

Boyle's and Henry's Laws will be used in developing equations for the compressibility of an air-water mixture. These laws are defined and explained for purposes of completeness. Boyle's Law states that "at a constant temperature, the volume of a given quantity of any gas varies inversely as the pressure to which the gas is subjected" (CRC Handbook 1980).

Air dissolves in water according to Henry's Law, which states that "the weight of gas dissolved in a fixed quantity of liquid, at constant temperature, is directly proportional to the pressure of the gas above the solution" (Fredlund 1976). Fredlund (1976) explains that the structure of water molecules produces a "porosity" within the water of approximately 2 percent by volume. This porosity can be filled by a gas such as air, i.e., air dissolves in water by filling this pore space (see Table 4.1).

Fredlund (1976) provides a simple analogy to understand the compressibility of an air-water mixture.

Consider a test vessel made of a cylinder and piston. At the base of the cylinder is a porous stone having a porosity of 2 percent; the porous stone simulates the behavior of the water. The piston is initially positioned some distance above the stone with air filling the space in between. An imaginary valve at the surface of the porous stone controls the movement of air into the stone. The air in the porous stone simulates the air dissolved in water. If the valve is closed and the piston moves down into the cylinder, the air above the stone compresses following Boyle's Law. If the valve is opened, some of the air will diffuse into the porous stone following Henry's Law. This process will continue until all of the air passes into the porous stone. When the piston con-

Table 4.1.
Solubility of Air in Water

Temperature Degrees C	Henry's Constant
0	0.02918
4	0.02632
10	0.02284
15	0.02055
20	0.01868
25	0.01708
30	0.01564
from Fredlund (1976)	

tacts the porous stone, there is a discontinuity in the compressibility of the system; the compressibility jumps immediately to that of water. The level of saturation within an air-water mixture must be evaluated to determine the discontinuity point.

Derivation of equations

The following assumptions were made for this analysis. We will assume initial saturation levels are greater than 85 percent, which implies that all air bubbles are occluded. Surface tension effects will be neglected, which allows us to assert that the air bubbles within the water will be at the same pressure as the water. The air is soluble in water and observes Henry's Law, and the rate of increase in pore water pressure from any simulation is slower than the rate of diffusion of air in water. Finally, prior to full saturation, the compressibility or bulk modulus of water is a constant. We will first develop the equations for an air-water system with a rigid porous skeleton, then one with a compressible porous skeleton.

The following terms are used in the derivation of the compressibility of an air-water mixture. Let

- V denote the total volume of air and water,
- V_v the volume of the void space,
- V_w the volume of water,
- V_d the volume of dissolved air,
- V_a the total volume of air,
- V'_a the volume of free air, which is equal to $V_a - V_d$,
- P_w the pore water pressure,
- P_a the pore air pressure and
- H Henry's constant.

A subscripted "o" is used to indicate an initial value. The total mass of air and water remains constant. Substituting expressions for porosity (n) and saturation (S), the initial volumes of water V_{wo} and free air V'_{ao} may be expressed as

$$V_{wo} = S_o V_{vo} = n_o V_o S_o \quad 4.5$$

and

$$V'_{ao} = (1 - S_o) V_{vo} = n_o V_o (1 - S_o) \quad 4.6$$

Using Henry's Law and Equation 4.5, the initial volume of dissolved air may be expressed as

$$V_{do} = V_{wo} H = n_o V_o S_o H \quad 4.7$$

The sum of Equations 4.6 and 4.7 yields an expression for the initial total

volume of air in the system

$$V_{ao} = n_o V_o (1 - S_o + S_o H) \quad 4.8$$

Expressions for the compressibility of water and an air-water mixture may be written as

$$C_w = - \frac{1}{V_w} \frac{dV_w}{dP_w} \quad 4.9$$

and

$$C_m = - \frac{1}{V_a + V_w} \left[\frac{dV_a}{dP_w} + \frac{dV_w}{dP_w} \right] \quad 4.10$$

respectively. Substituting Equation 4.9 into Equation 4.10 one obtains

$$C_m = - \frac{1}{V_a + V_w} \left[\frac{dV_a}{dP_w} - V_w C_w \right] \quad 4.11$$

We will now use Boyle's Law to develop an expression for the derivative in Equation 4.11. Boyle's Law may be written as

$$V_a P_a = V_{ao} P_{ao} \quad 4.12$$

If we assume the pore and air pressure are equal and $V_d = V_{do}$, we can write the following

$$\frac{P_{ao}}{P_a} = \frac{P_{wo}}{P_w} = \frac{V_a + V_d}{V_{ao} + V_d} \quad 4.13$$

from which we write

$$\begin{aligned} \frac{dP_w}{dV_a} &= - \frac{V_{ao} + V_d}{(V_a + V_d)^2} P_{ao} \\ &= - \frac{V_{ao} P_{ao}}{V_a^2} \end{aligned} \quad 4.14$$

Substituting the latter expression in Equation 4.14 into Equation 4.11, one

obtains

$$C_m = \frac{1}{V_a' + V_w} \left[\frac{V_a^2}{V_{ao} P_{ao}} + V_w C_w \right] \quad 4.15$$

which is an expression for the compressibility of an air-water mixture. By judiciously substituting for the volume terms in Equation 4.15, we will develop a final expression for the compressibility of the mixture.

By combining Boyle's Law (Equation 4.12) and Equation 4.8, we may write an expression for the current total volume of air

$$V_a = \frac{P_{ao}}{P_a} n_o V_o (1 - S_o + S_o H) \quad 4.16$$

The current volume of water may be expressed as

$$V_w = V_{wo} (1 + C_w \delta P) \quad 4.17$$

and, after substituting for V_{wo} , as

$$V_w = n_o V_o S_o (1 + C_w \delta P) \quad 4.18$$

The current volume of dissolved air, which is a function of Henry's Law and the current volume of water, is written as

$$V_d = n_o V_o S_o H (1 + C_w \delta P) \quad 4.19$$

Subtracting Equation 4.19 from Equation 4.16, one obtains an expression for the current volume of free air

$$V_a' = n_o V_o \left\{ \frac{P_{ao}}{P_a} (1 - S_o + S_o H) - S_o H (1 + C_w \delta P) \right\} \quad 4.20$$

Adding Equations 4.20 and 4.18, one obtains

$$V_a' + V_w = n_o V_o \left\{ \frac{P_{ao}}{P_a} (1 - S_o + S_o H) + S_o (1 - H) (1 + C_w \delta P) \right\} \quad 4.21$$

which will eventually be substituted back into Equation 4.15. Combining

Equations 4.8 and 4.16, one may write

$$\frac{V_a^2}{V_{ao}} = \left[\frac{P_{ao}}{P_a} \right]^2 n_o V_o (1 - S_o + S_o H) \quad 4.22$$

and, by multiplying Equation 4.18 by the compressibility of water and dropping the higher order terms, one obtains

$$V_w C_w = n_o V_o S_o C_w \quad 4.23$$

Substituting Equations 4.21, 4.22, and 4.23 into Equation 4.15 yields the final expression for the compressibility of an air-water mixture

$$C_m = \left\{ \frac{P_{ao}}{P_a} (1 - S_o + S_o H) + S_o (1 - H) (1 - C_w \delta P) \right\}^{-1} \quad 4.24$$

$$\times \left\{ \frac{P_{ao}}{P_a^2} (1 - S_o + S_o H) + S_o C_w \right\}$$

In a similar manner, an expression for the level of saturation may be developed and written as

$$S = \frac{V_w}{V_a + V_w} \quad 4.25$$

$$= \frac{S_o (1 + C_w \delta P)}{\frac{P_{ao}}{P_a} (1 - S_o + S_o H) + S_o (1 - H) (1 + C_w \delta P)}$$

When the porous skeleton is compressible, the current void volume may be expressed as

$$V_a + V_w = V_o (n_o - \epsilon_{kk}) \quad 4.26$$

where V_o is the initial total volume of voids and solids and ϵ_{kk} is the effective volumetric strain. Substituting the above and Equation 4.18 into the first expression in Equation 4.25, one obtains

$$S = \frac{V_w}{V_a + V_w} = \frac{n_o S_o (1 - C_w \delta P)}{n_o - \epsilon_{kk}} \quad 4.27$$

which is an expression for the level of saturation in a deforming porous skeleton. An equation for the compressibility of an air-water mixture within a deforming porous skeleton may be obtained by combining Equations 4.15, 4.22, 4.23, and 4.26 to yield

$$C_m = \frac{n_o}{n_o - \epsilon_{kk}} \left\{ \frac{P_{ao}}{P_a^2} (1 - S_o + S_o H) + S_o C_w \right\} \quad 4.28$$

In the process of a calculation, one must first evaluate Equation 4.27. If the level of saturation is less than one, Equation 4.28 is used to calculate the bulk modulus of the pore fluid. If the level of saturation is equal to one, the bulk modulus of the pore fluid is calculated from the EOS of water, i.e., Equation 4.4.

To illustrate the response of a partially-saturated material to an applied loading, an example calculation was conducted and the output graphically

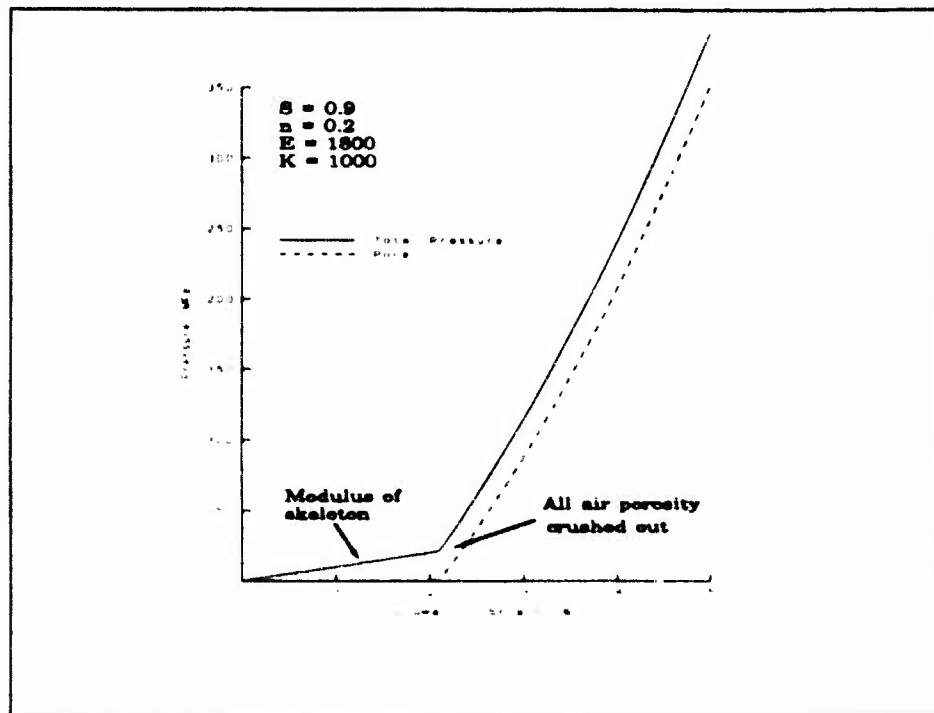


Figure 4.2. Pressure-volume response of partially-saturated material

presented in Figure 4.2. The simulated material has a Young's modulus of 1800 MPa, a bulk modulus of 1000 MPa, a total porosity of 20 percent, a

saturation level of 90 percent, and an air porosity of 2 percent. The material was loaded under undrained uniaxial strain boundary conditions. At volume strains less than approximately 2 percent, the generated pore pressures are negligible, and the loading bulk modulus is equal to the skeletal bulk modulus of 1000 MPa. At these strain levels, the material loads as if it were fully drained. At a volume strain of 2 percent, all of the air porosity is eliminated, and the pore fluid becomes fully saturated and begins to carry a major portion of the applied stress. At these strain levels and above, the material loads as a fully-saturated material. In addition, the pressure-volume response is nonlinear due to the nonlinear nature of the water.

Equation of State for Solids

Three methods for calculating the bulk modulus of the grain solids were implemented into the FE program. The first method assumes the grain solids are linear elastic materials. The second method uses an analytical EOS and treats the solids as a nonlinear elastic material. The third method uses a simple model to simulate the nonlinear hysteretic material behavior of the grains.

The first method is self explanatory; the program simply uses a constant bulk modulus value for the entire calculation. In the second method, an analytic relationship between pressure and compression is developed for each material. Compression is defined as

$$\mu = \frac{\epsilon}{1 - \epsilon} \quad 4.29$$

where ϵ is the Cauchy or engineering strain. Using solid carbonate as an example material, the pressure-compression relationship is linear below 1.2 GPa and may be written as

$$P_g = 0.7 \mu \quad 4.30$$

where P_g is the grain pressure. The bulk modulus for carbonate may then be written as

$$K_g = (1 - \mu)^2 \frac{dP}{d\mu} = 0.7 (1 - \mu)^2 \quad 4.31$$

A plot of pressure versus volumetric strain for carbonate is plotted in Figure 4.3. Other materials may be simulated in an analogous manner.

The third model, which simulates nonlinear hysteretic material behavior, uses tabulated curves that describe the loading and unloading pressure-volume response of the grains. This model is based on the work of Meier (1986),

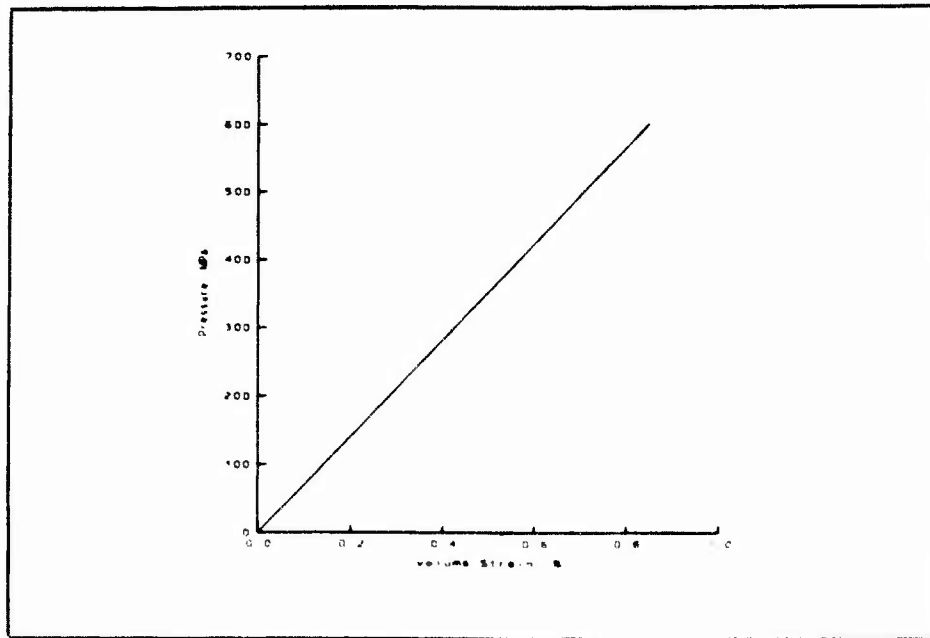


Figure 4.3. Pressure versus volume strain response of carbonate

who used a similar model for one-dimensional, plane-wave ground shock calculations.

During virgin loading, the volume strain is computed from the current value of pressure through linear interpolation of the tabulated loading curve. A similar process is employed when unloading occurs from pressure levels at or above the lockup point using the tabulated unloading curve. When unloading takes place from pressure levels below the lockup point, a scaling process must be applied to the tabulated unloading curve. In this scaling process, let P_m and ϵ_m represent the peak pressure and peak volume strain, respectively, from which unloading commences (see Figure 4.4). The pressure and volume strain scaling factors are calculated as

$$f_p = \frac{P_l - P_t}{P_m - P_t} \quad 4.32$$

and

$$f_\epsilon = (1 - a)f_p + a \quad 4.33$$

where P_l is the pressure at lock up, P_t is the tension cutoff pressure, and a is an empirically determined calibration constant with values ranging between zero and unity. Knowing the unloading pressure (P_l), the recovered pressure (ΔP), which is the difference between the pressure at lock up and the value of pressure on the tabulated unloading curve, is calculated in the following manner

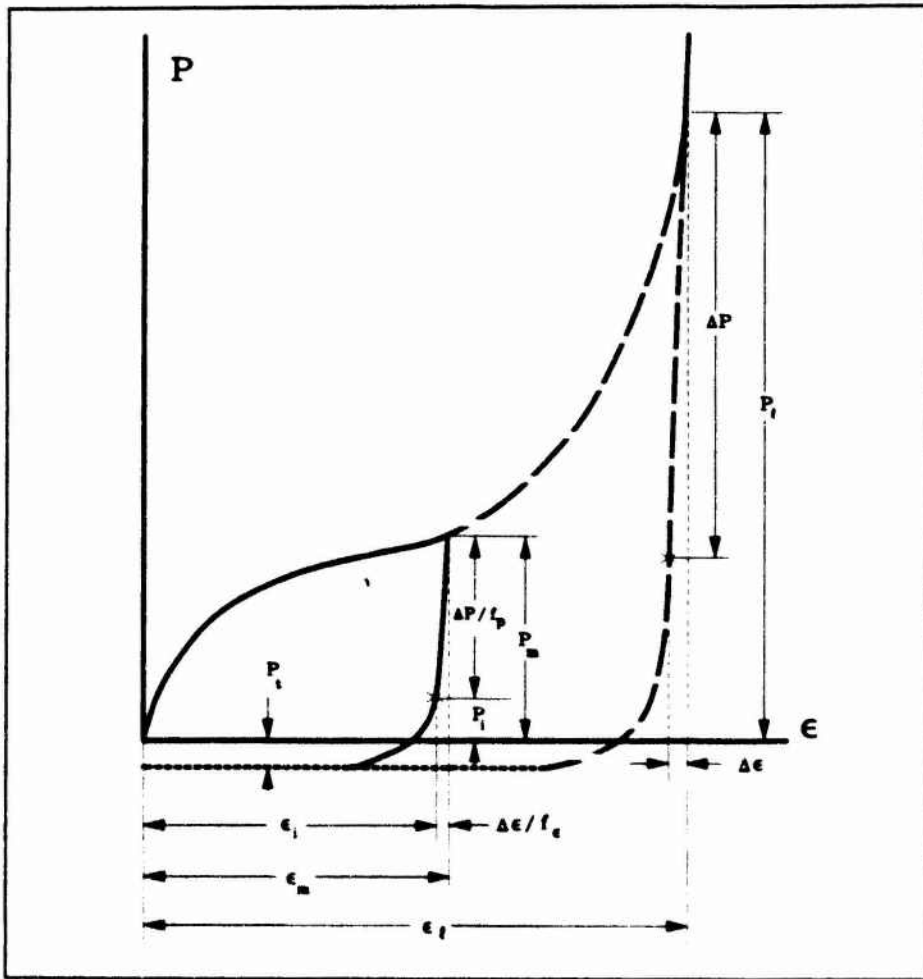


Figure 4.4. Nonlinear-hysteretic model

$$\Delta P = (P_m - P_i) f_p \quad 4.34$$

The recovered strain ($\Delta \epsilon$) is computed through linear interpolation of the tabulated unloading curve. The unloading volume strain (ϵ_i) is calculated by subtracting the scaled value of recovered strain from the peak strain

$$\epsilon_i = \epsilon_m - \frac{\Delta \epsilon}{f_e} \quad 4.35$$

The bulk modulus on this unloading curve is calculated as

$$K_i = K_u (f_e / f_p) = K_u \left[1 - a + \frac{a}{f_p} \right] \quad 4.36$$

where $K_u = \Delta P / \Delta \epsilon$. Reloading occurs along a line passing between the last unloading pressure-volume strain point and the point P_m, ϵ_m .

Summary

The algorithms required to numerically simulate the behavior of the three primary constituents of geomaterials, air, water and solids, were documented in this chapter. When these algorithms are combined with an appropriate skeletal model into the FE formulation of Biot's theory, the multikilobar response of any geomaterial may be calculated.

5 Features and Verification of FE Program

Introduction

The objectives of this chapter are to (1) describe features in the FE program that have not already been introduced and (2) present solutions from several verification problems as proof that the program works correctly. Several features of the FE program have already been introduced. In Chapter 2, the benefits gained from effective stress simulations of multi-kilobar material behavior and the available material models were described. The cap model was documented in Chapter 3 and the equations of state of air, water, and solids were described in Chapter 4.

The following features will be presented in this chapter. A restart feature was implemented into the FE program to permit the simulation of certain laboratory tests. For example, a consolidated undrained triaxial compression test wherein the consolidation phase has drained boundary conditions and the shear phase has undrained boundary conditions requires changing fluid flux boundary conditions. A brief summary of the postprocessing procedures will also be presented. These features are described in the next section.

The final sections of this chapter document solutions from several verification problems. For each problem, the FE solution is compared to available closed form or analytic solutions. These verification problems establish the FE program's ability to correctly solve a variety of initial and boundary value problems.

Additional Features of FE Program

Restart feature

The restart feature was implemented for the purpose of allowing the user to change the boundary conditions at a preselected time in the calculation. A K_0 /BX/STX test (acronyms defined subsequently) is an example of a laboratory test with changing boundary conditions. This test is conducted by

loading a cylindrical specimen to a desired mean normal stress level under K_0 or uniaxial strain boundary conditions, unloading to a desired mean normal stress level under constant axial strain (BX) boundary conditions, and then conducting a constant radial stress triaxial compression (STX) test at yet another mean normal stress level. The K_0 loading and the BX unloading phases may be numerically simulated with displacement controlled boundary conditions. However, to realistically attempt to simulate the STX phase, the user should apply stress controlled boundary conditions. The restart feature implemented into JAM allows the user to perform this calculation in a simple manner.

Postprocessing

In many instances, one would like to plot FE results at a single location, e.g., at the nodal points. Many postprocessing FE software packages require stress and strain values at the nodes rather than at the Gauss integration points. A procedure was implemented in the FE program JAM to extrapolate and smooth Gauss point data to the element vertices, i.e., corner nodes. Values at the midside nodes were then calculated from the values at the appropriate corner nodes.

The implemented smoothing procedure was developed and described by Hinton, Scott, and Ricketts (1975) and Hinton and Campbell (1974). The procedure is simple and straightforward. The smoothed stresses at the nodes may be calculated from the expression

$$\begin{Bmatrix} \bar{\sigma}_1 \\ \bar{\sigma}_2 \\ \bar{\sigma}_3 \\ \bar{\sigma}_4 \end{Bmatrix} = \begin{bmatrix} a & b & c & b \\ b & a & b & c \\ c & b & a & b \\ b & c & b & a \end{bmatrix} \begin{Bmatrix} \sigma_I \\ \sigma_{II} \\ \sigma_{III} \\ \sigma_{IV} \end{Bmatrix} \quad 5.1$$

where the $\bar{\sigma}_i$ are the smoothed stresses, $\sigma_I, \sigma_{II}, \sigma_{III}$ and σ_{IV} are the stresses

at the integration points, and $a = 1 + \frac{\sqrt{3}}{2}$, $b = -\frac{1}{2}$ and $c = 1 - \frac{\sqrt{3}}{2}$.

At a given corner node, smoothed values from adjacent elements are averaged to yield a single value.

Plane and Axisymmetric Verification Problems

Five problems with plane or axisymmetric geometries were solved with JAM to test and verify that the material models, the eight-node quadrilateral element, and numerous other algorithms were correctly implemented in the FE program. For each of the five problems, selected output from JAM are

compared with closed form or analytic solutions.

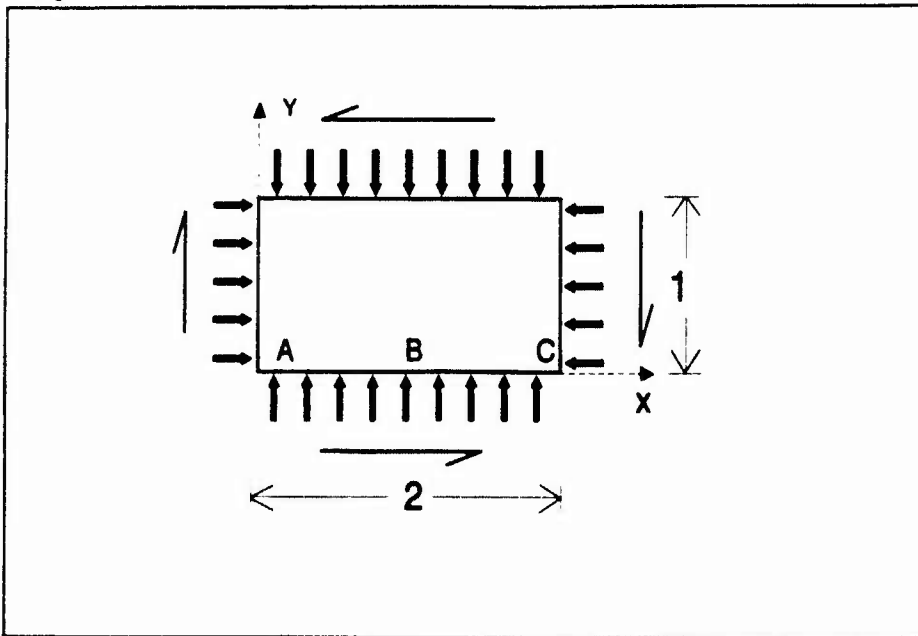


Figure 5.1. Geometry and loading conditions for Verification Problem 1

Verification Problem 1 exercises a single element under distributed normal and shear loads of 1000/length as shown in Figure 5.1. The element simulates an isotropic linear elastic material having a Young's modulus of 30×10^6 and a Poisson's ratio 0.3. The following boundary conditions were imposed:

$$u_x = u_y = 0 \text{ at point A and } u_y = 0 \text{ at points B and C}$$

Table 5.1.
Results from Verification Problem 1

Stress or Strain	Plane Strain		Plane Stress	
	JAM	Analytic	JAM	Analytic
σ_x	-1000.	-1000.	-1000.	-1000.
σ_y	-1000.	-1000.	-1000.	-1000.
σ_{xy}	-1000.	-1000.	-1000.	-1000.
σ_z	-600.	-600.	0.	0.
ϵ_x	-1.733×10^{-5}	-1.733×10^{-5}	-2.333×10^{-5}	-2.333×10^{-5}
ϵ_y	-1.733×10^{-5}	-1.733×10^{-5}	-2.333×10^{-5}	-2.333×10^{-5}
ν_{xy}	-8.667×10^{-5}	-8.667×10^{-5}	-8.667×10^{-5}	-8.667×10^{-5}

Table 5.1 compares stress and strain states calculated from the FE and

analytic solutions (Hibbitt, Karlsson and Sorensen 1989) for this problem under plane strain and plane stress boundary conditions. This problem exercises the elastic constitutive model, verifies that the eight-node quadratic element accurately models constant strain states, and also checks that distributed loads are correctly simulated. The results from JAM match the analytic solution exactly. Verification Problem 1 was also successfully solved using the Cap model algorithm.

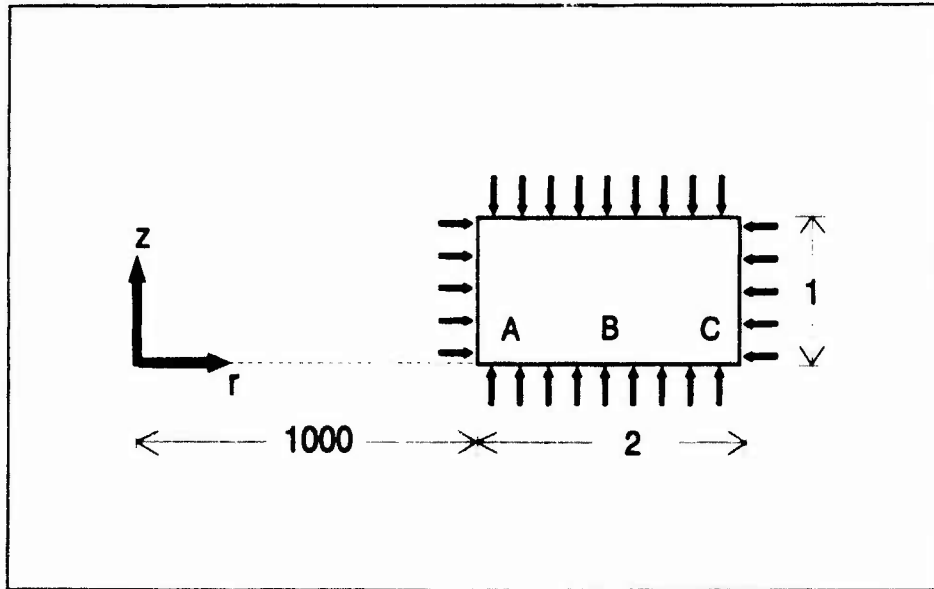


Figure 5.2. Geometry and loading conditions for Verification Problem 2

Verification Problem 2 exercises a single axisymmetric element under distributed normal loads of 1000/area as shown in Figure 5.2. The element simulates an isotropic linear elastic material having a Young's modulus of 30×10^6 and a Poisson's ratio 0.3. The following boundary conditions were imposed:

$$u_z = 0 \text{ at points A, B, and C}$$

Table 5.2 compares stress and strain states calculated from the FE and analytic solutions (Hibbitt, Karlsson and Sorensen 1989) under the imposed axisymmetric boundary conditions. Like Verification Problem 1, problem 2 exercises the elastic constitutive model, verifies that the eight-node quadratic element accurately models constant strain states, and also checks that distributed loads are correctly simulated. The results from JAM match the analytic solution exactly.

Plane and axisymmetric patch tests were employed in Verification Problems 3 and 4. In the patch test, nodal point displacements are applied to a patch of elements such that a constant state of strain exists throughout the mesh. In Verification Problem 3, the elements simulate an isotropic linear elastic material having a Young's modulus of 30×10^6 and a Poisson's ratio 0.3. The imposed displacement boundary conditions were applied to the patch

Table 5.2.
Results from Verification Problem 2

Stress or Strain	Axisymmetric	
	JAM	Analytic
σ_r	-1000.	-1000.
σ_z	-1000.	-1000.
σ_{rz}	0.	0.
σ_θ	-1000.	-1000.
ϵ_r	-1.333×10^{-5}	-1.333×10^{-5}
ϵ_z	-1.333×10^{-5}	-1.333×10^{-5}
ν_{rz}	0.	0.
ϵ_θ	-1.333×10^{-5}	-1.333×10^{-5}

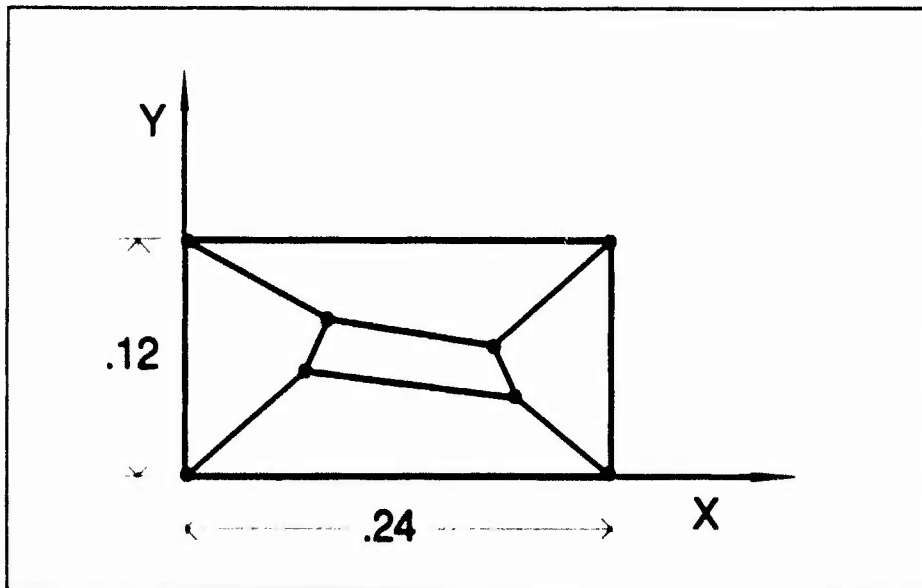


Figure 5.3. Geometry for Verification Problem 3

of elements shown in Figure 5.3 and were calculated as:

$$u_x = \left[x + \frac{y}{2} \right] \times 10^{-3} \quad \text{and} \quad u_y = \left[y + \frac{x}{2} \right] \times 10^{-3}$$

Table 5.3 compares stress and strain states calculated from the FE and analytic solutions (Hibbitt, Karlsson and Sorensen 1989) for this problem under plane strain and plane stress boundary conditions. The results from JAM match the analytic solution exactly. Verification Problem 3 was also successfully solved using the Cap model algorithm.

Verification Problem 4 consists of a patch of axisymmetric elements

Table 5.3.
Results from Verification Problem 3

Stress or Strain	Plane Strain		Plane Stress	
	JAM	Analytic	JAM	Analytic
σ_x	1600.	1600.	1333.	1333.
σ_y	1600.	1600.	1333.	1333.
σ_{xy}	400.	400.	400.	400.
σ_z	800.	800.	0.	0.
ϵ_x	$1. \times 10^{-3}$	$1. \times 10^{-3}$	$1. \times 10^{-3}$	$1. \times 10^{-3}$
ϵ_y	$1. \times 10^{-3}$	$1. \times 10^{-3}$	$1. \times 10^{-3}$	$1. \times 10^{-3}$
ν_{xy}	$1. \times 10^{-3}$	$1. \times 10^{-3}$	$1. \times 10^{-3}$	$1. \times 10^{-3}$

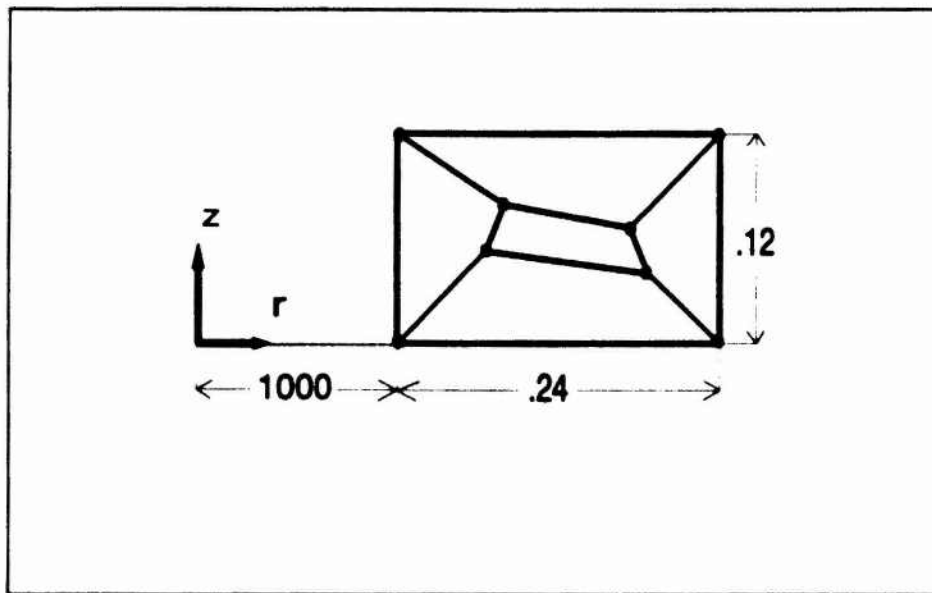


Figure 5.4. Geometry for Verification Problem 4

simulating an isotropic linear elastic material having a Young's modulus of 30×10^6 and a Poisson's ratio 0.3. The imposed displacement boundary conditions were applied to the patch of elements shown in Figure 5.4 and were calculated as:

$$u_r = \left[(r - 1000) + \frac{z}{2} \right] \times 10^{-3} \quad \text{and} \quad u_z = \left[z + \frac{(r - 1000)}{2} \right] \times 10^{-3}$$

Table 5.4 compares stress and strain states calculated from the FE and analytic solutions (Hibbitt, Karlsson and Sorensen 1989) for this problem. The results from JAM match the analytic solution exactly. Verification Problem 4 was also successfully solved using the Cap model algorithm.

Table 5.4.
Results from Verification Problem 4

Stress or Strain	Axisymmetric	
	JAM	Analytic
σ_r	5.769×10^4	5.769×10^4
σ_z	5.769×10^4	5.769×10^4
σ_{rz}	1.154×10^4	1.154×10^4
σ_θ	3.462×10^4	3.462×10^4
ϵ_r	$1. \times 10^{-3}$	$1. \times 10^{-3}$
ϵ_z	$1. \times 10^{-3}$	$1. \times 10^{-3}$
γ_{rz}	$1. \times 10^{-3}$	$1. \times 10^{-3}$
ϵ_θ	0.	0.

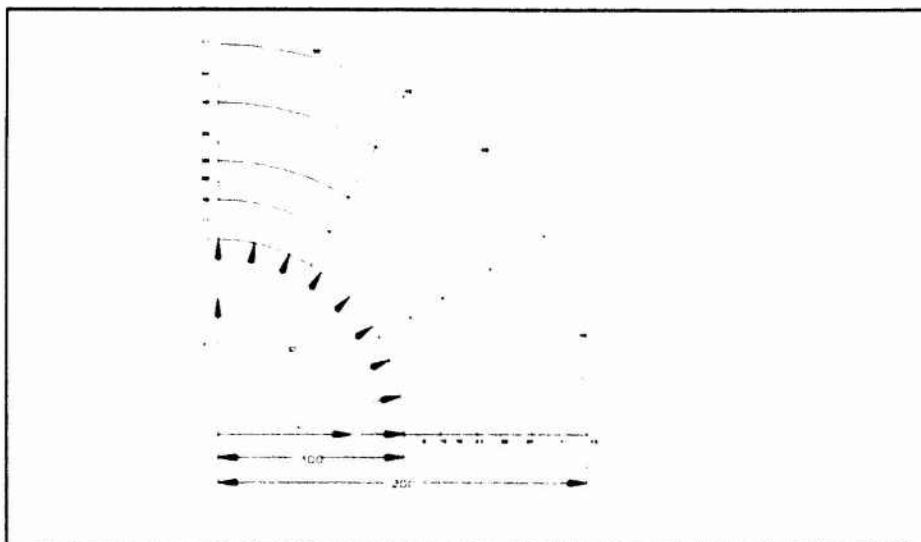


Figure 5.5. Mesh geometry for Verification Problem 5

Verification Problem 5 is a plane strain simulation of a thick wall cylinder subjected to an increasing internal pressure. Due to the symmetry of the problem, a quarter grid was used in the calculation; the problem geometry and FE mesh are shown in Figure 5.5. The material was modeled with the following properties, a Young's modulus of 21000, a Poisson's ratio of 0.3, a yield stress of 24 and a linear hardening modulus of 0. When a cylinder with these properties is subjected to an increasing internal pressure above 10.4, an elastic-plastic boundary moves through the cylinder; on the external side of the boundary, all of the strains are elastic, and on the interior side, the strains are elastic-plastic. Table 5.5 compares stresses calculated from the FE and analytic solutions (Hodge and White 1950; Prager and Hodge 1951) at several radii within the elastic region for an applied internal pressure of 18, which places the elastic-plastic boundary at a radius of 160. The computed results

Table 5.5.
Results from Verification Problem 5

Stress	Radius	Plane Strain	
		JAM	Analytic
Max. Principal Stress or σ_θ	163.64	22.12	22.09
	176.32	20.32	20.25
	193.64	18.37	18.31
σ_z	> 160	5.33	5.31
J_1	> 160	23.11	23.03

are well within the imposed convergence tolerance of 1 percent. The results from JAM also agree with the results calculated by Owen and Hinton (1980) for this problem. This validates the plasticity formulation in JAM.

Consolidation Problems

To verify that the FE program could solve consolidation problems, output from JAM were compared to the results calculated from closed form solu-

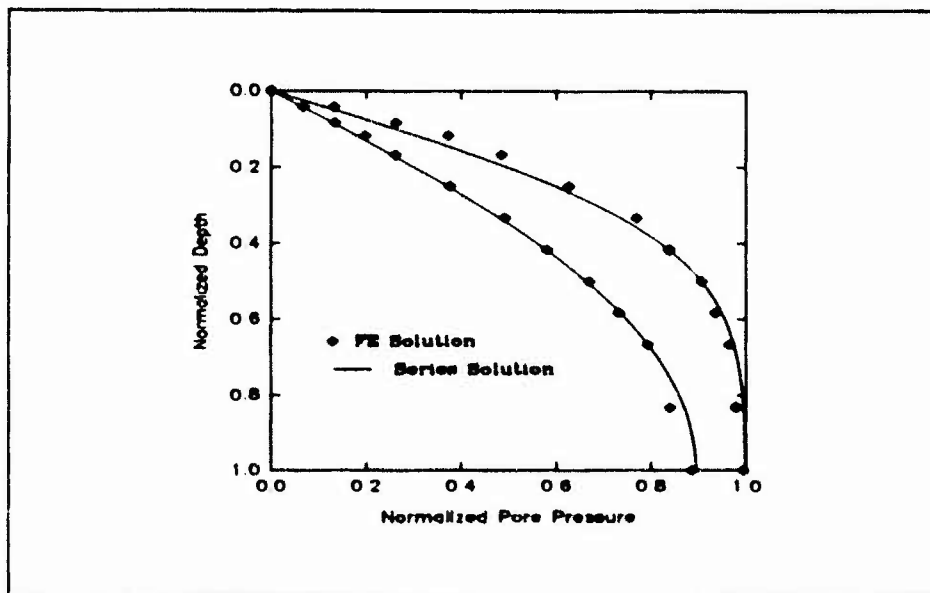


Figure 5.6. Pore pressure versus depth at two time increments

tions. Boundary conditions and material properties were altered to fully exercise different features within the FE program. In Figure 5.6, depth versus calculated pore fluid pressures are plotted in a normalized format at two different time increments for a one-dimensional consolidation problem in which

the soil column was idealized as an elastic porous skeleton with an incompressible pore fluid. Good agreement is shown between the FE results and the closed form solution. A similar one-dimensional problem was solved with two materials having compressible pore fluids, where the ratios of pore fluid modulus to skeletal modulus (N) were 2000 (nearly incompressible pore fluid) and 5 (highly compressible pore fluid). Results from the FE program and the closed form solution (Chang and Duncan 1983) are plotted in Figure 5.7 as normalized displacements versus time factor, i.e., normalized time. Again,

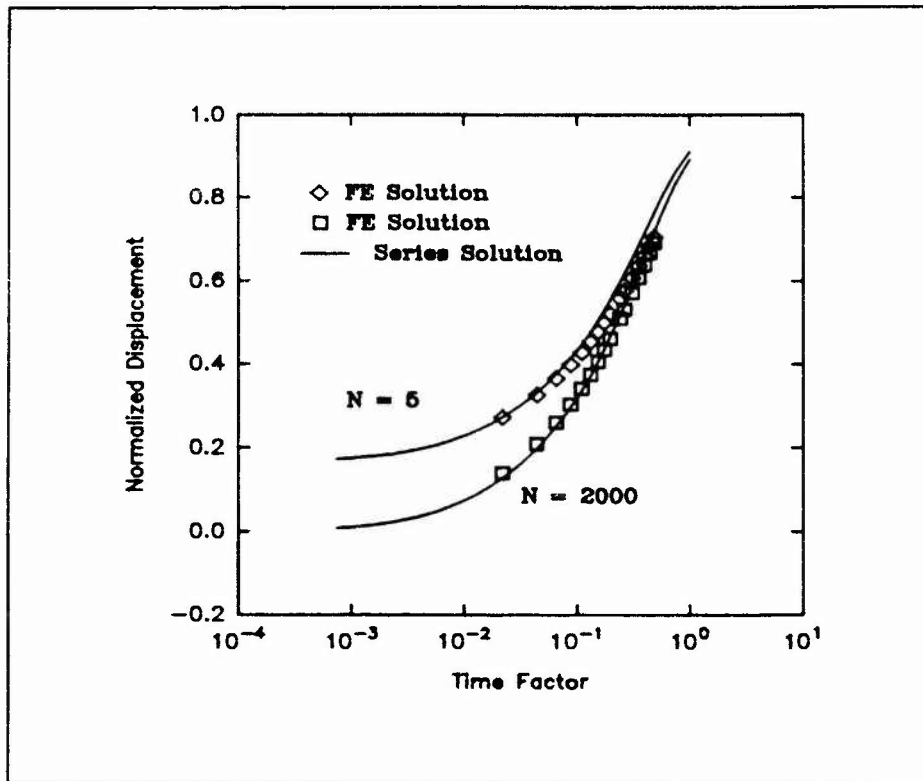


Figure 5.7. Displacement versus time for one-dimensional consolidation of an idealized elastic material

the results show reasonable agreement between the FE results and the closed form solution.

A two-dimensional axisymmetric consolidation problem consisting of a circular foundation on a finite soil layer (Figure 5.8) was also calculated. The mesh is A units high by $10A$ units wide, and a uniform vertical load of radius A was applied to the top surfaces of three elements to simulate the foundation loads. The following boundary conditions were invoked for this problem. The vertical edges of the mesh (A-D and B-C) were constrained in the radial direction, the bottom edge of the mesh (C-D) was constrained in the vertical direction, the top surface (A-B) was free draining, and no flow conditions were applied to the three remaining surfaces (B-C, C-D, and A-D). The calculated settlements (in dimensionless format) from JAM (solid circles) are compared in Figure 5.9 to settlements calculated from the analytical solution

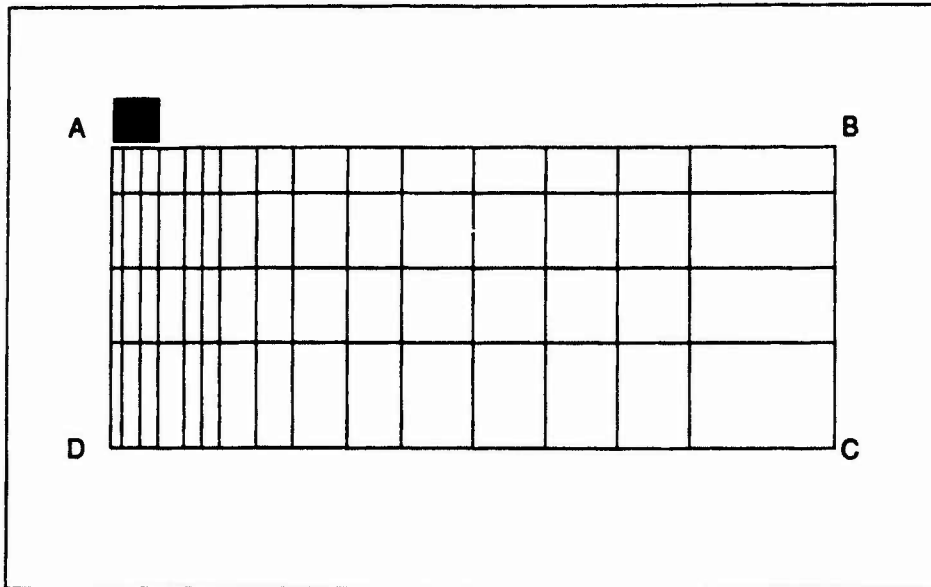


Figure 5.8. Mesh geometry for Axisymmetric Consolidation Problem

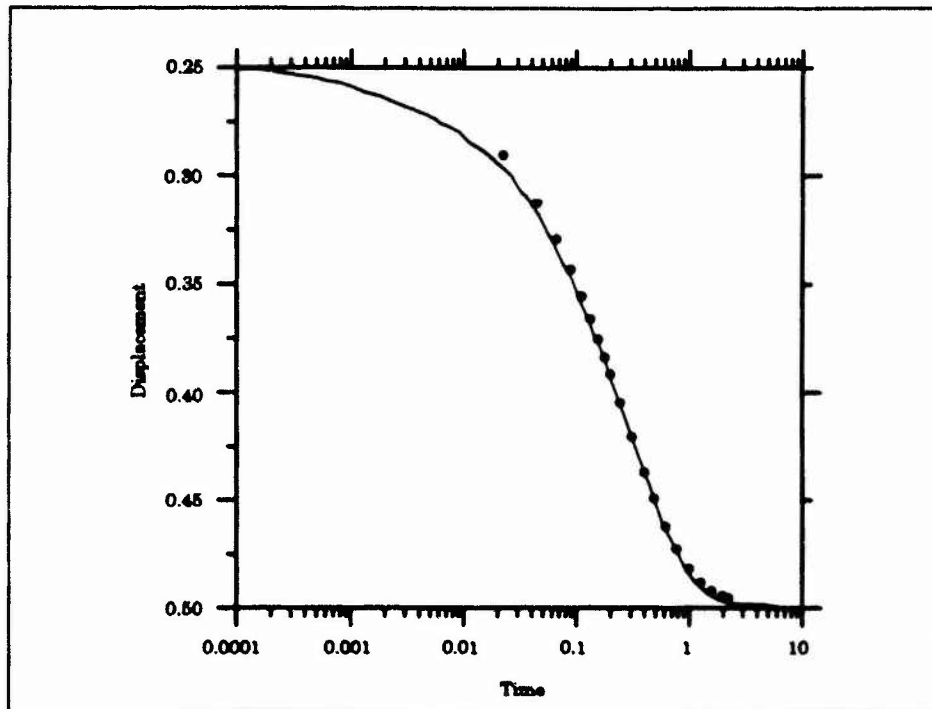


Figure 5.9 Displacement vs Time from 2D Consolidation Problem

(solid line). Again, there is excellent agreement between the calculation and the analytical solution.

Cryer Problem

A numerical simulation of Cryer's problem (Cryer 1963) was conducted as an additional verification test of the FE program. Cryer developed a closed

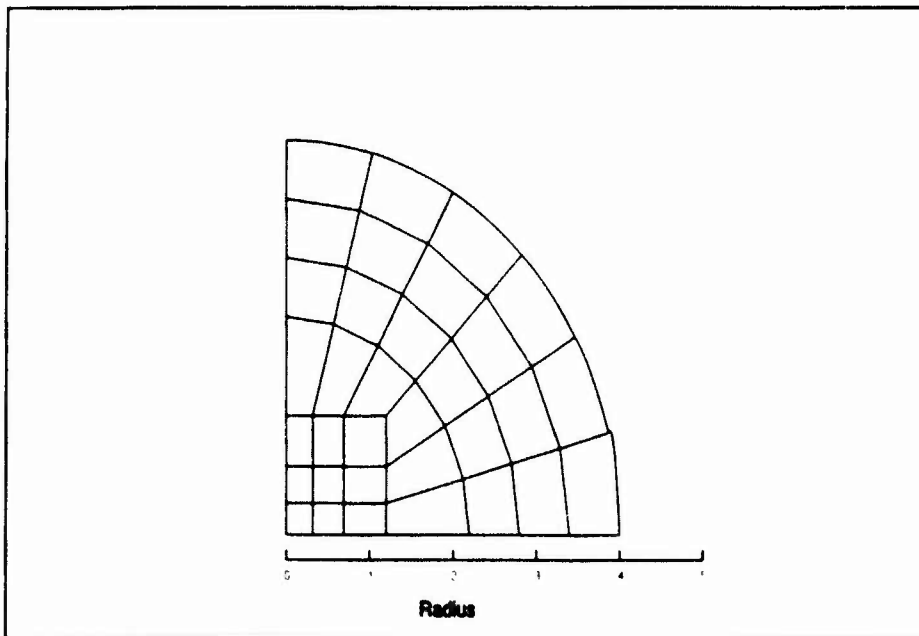


Figure 5.10. Mesh geometry for Cryer Problem

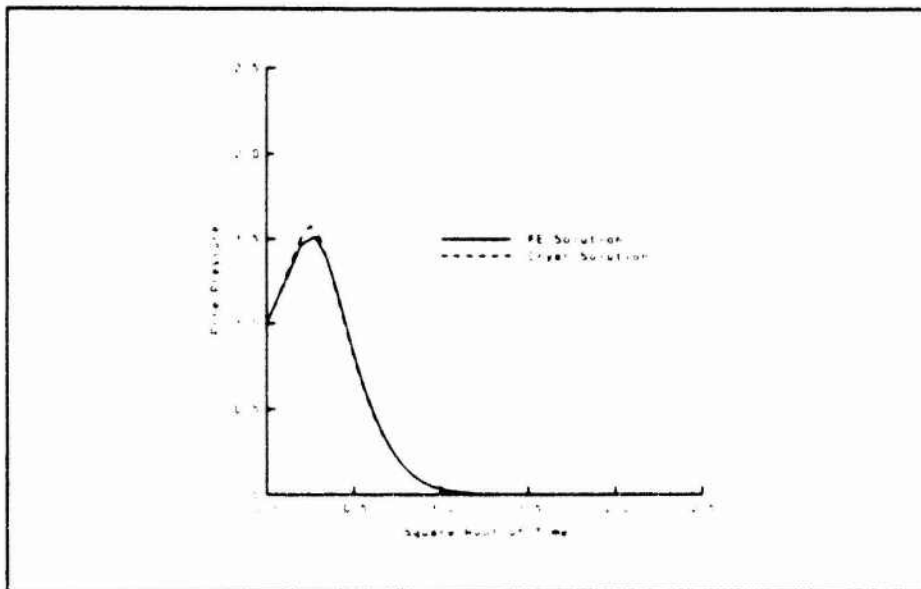


Figure 5.11. Dimensionless pore pressure response for Cryer's problem

form solution to the problem of a sphere of elastic porous material loaded on the surface by a constant uniform pressure and having drained boundary conditions. For values of Poisson's ratio less than 0.5, pore pressure at the center of the sphere increases to stress levels greater than the externally applied pressure and then dissipates. The greatest increase in pore pressure

occurs for values of Poisson's ratio equal to 0. This response is called the Mandel-Cryer effect after the two mathematicians who discovered the phenomena. Gibson et al. (1963) conducted laboratory experiments on clay spheres and were able to reproduce the Mandel-Cryer effect. They demonstrated that the total stress within a consolidating sphere is not time invariant as predicted by Terzaghi-Rendulic consolidation theory. Dimensionless total stress at the center of the sphere increases above unity and approaches unity at late time.

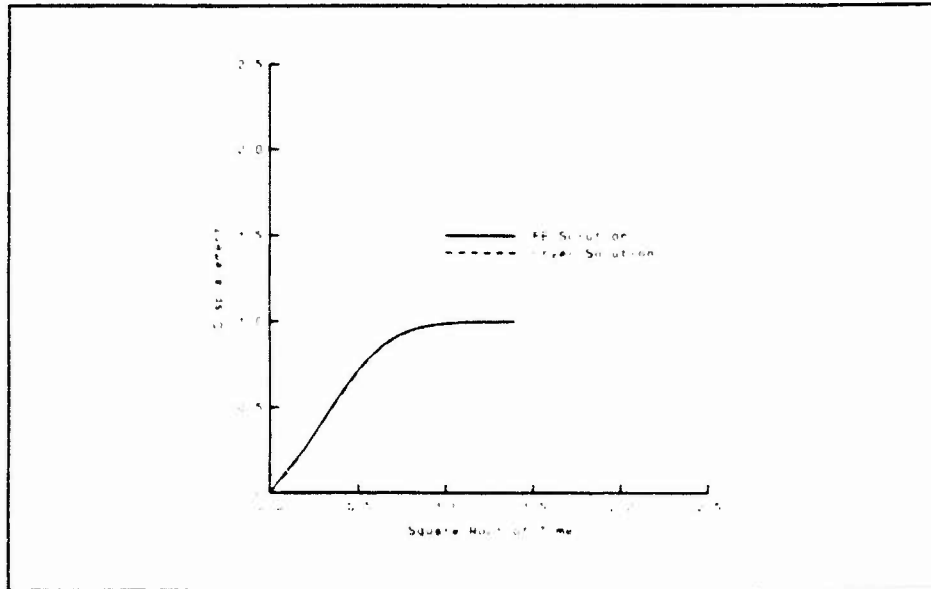


Figure 5.12. Dimensionless displacement response for Cryer's problem

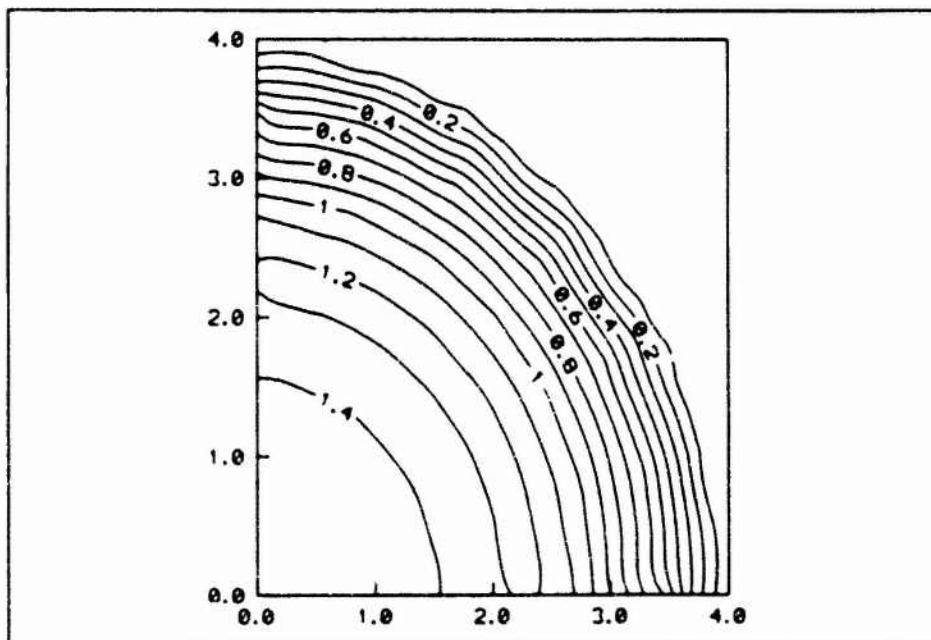


Figure 5.13. Pore pressure contours for Cryer Problem

Utilizing the symmetry of the problem, the soil sphere was represented by the mesh depicted in Figure 5.10 and calculated as an elastic axisymmetric problem. A unit pressure was placed on the boundary during the first increment of loading and held constant thereafter. Figure 5.11 and Figure 5.12 compare the results from JAM with the closed form solution for a value of Poisson's ratio equal to 0. Figure 5.11 is a plot of dimensionless pore pressure at the center of the sphere versus the square root of dimensionless time; Figure 5.12 is a plot of dimensionless displacement of the outer surface of the sphere versus the square root of dimensionless time. The comparison between the FE calculation and the closed form solution is very good. Pore pressure contours at a dimensionless time of approximately 0.04 are plotted in Figure 5.13. At this early time, a significant portion of the sphere has pore pressures greater than unity.

Summary

In this chapter, the restart and post-processing features of the FE program were described. The documented verification problems indicate that the FE program correctly calculates one- and two-dimensional consolidation problems and elastic and elastic-plastic boundary value problems. Although the successful calculation of these verification problems does not certify the FE program is error free, they should increase the confidence of the end user.

6 Numerical Simulations

Introduction

Numerical simulations of limestone behavior under drained and undrained boundary conditions are presented in this chapter. The ability of the 14-parameter cap model to simulate the basic drained behavior of limestone is demonstrated by comparing calculated responses of hydrostatic, uniaxial strain, and triaxial compression loadings with measured or recommended limestone responses. In a similar manner, the ability of the FE code to calculate the undrained behavior of limestone is demonstrated by comparing calculated responses of uniaxial strain loadings with recommended limestone responses. Finally, some example calculations are documented that demonstrate the utility of the FE code in analyzing laboratory test specimen conditions.

Salem Limestone

The limestone simulated in this chapter is commonly referred to as Salem, Bedford, or Indiana limestone. It was extracted from the Salem formation near the community of Bedford, Indiana. Mechanical property tests were conducted on intact specimens of 13.5-percent porosity Salem limestone by the Vermont office of Applied Research Associates. These mechanical property tests included drained and undrained (with pore pressure measurements) hydrostatic loading tests, K_0 or uniaxial strain tests, triaxial compression tests, and strain path tests. Laboratory test data and recommended material properties were obtained from Blouin and Chitty (1988a, 1988b) and Zelasko (1991).

Simulations

Process

Prior to numerically simulating limestone behavior under drained or undrained boundary conditions, the skeletal or drained behavior of Salem limestone was required. The 14-parameter cap model, which was documented in Chapter 3, was fit to recommended drained Salem limestone mechanical

properties. With this model and fit implemented into JAM, drained single-element boundary value problems were conducted to insure the FE code would reproduce the cap model calculations. Undrained single-element boundary value problems were then conducted.

Drained limestone simulations

The following recommended drained Salem limestone mechanical properties were available for fitting: a failure envelope, hydrostatic load and unload behavior, K_0 stress-strain behavior, K_0 pressure-volume behavior and K_0 stress paths, stress-strain curves from triaxial compression tests conducted at several confining stress levels, and strain path data along three different paths.

Typically, a high fidelity fit of both the hydrostatic loading and K_0 , or uniaxial strain, responses is impossible to capture with a relatively simple cap

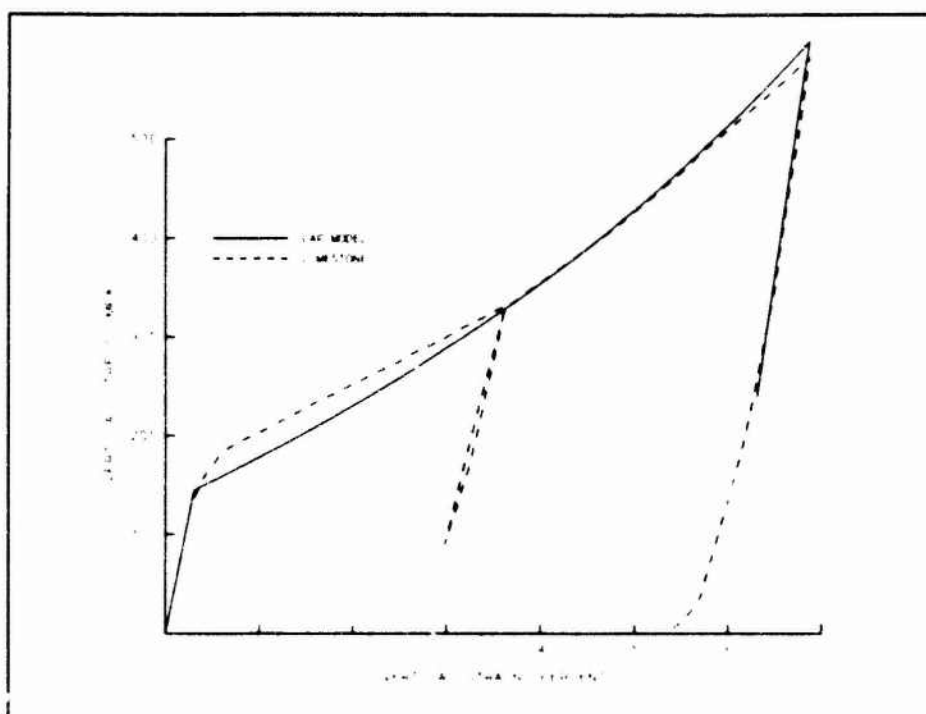


Figure 6.1. Drained K_0 stress-strain comparison

model. For this reason, greater emphasis was placed on fitting the uniaxial-strain stress path and stress-strain responses and less emphasis on the hydrostatic loading response. In Figures 6.1-6.3, the calculated drained K_0 stress and strain responses from the 14-parameter cap model are compared to the recommended drained K_0 behavior. Figure 6.1 compares the drained K_0 stress-strain behavior, Figure 6.2 the K_0 stress paths, and Figure 6.3 the K_0 pressure-volume responses. The quality of the fits are very good. To make these fits, one must compromise between fitting the K_0 stress path and the K_0 stress-strain behavior. The model K_0 stress-strain response breaks over at a

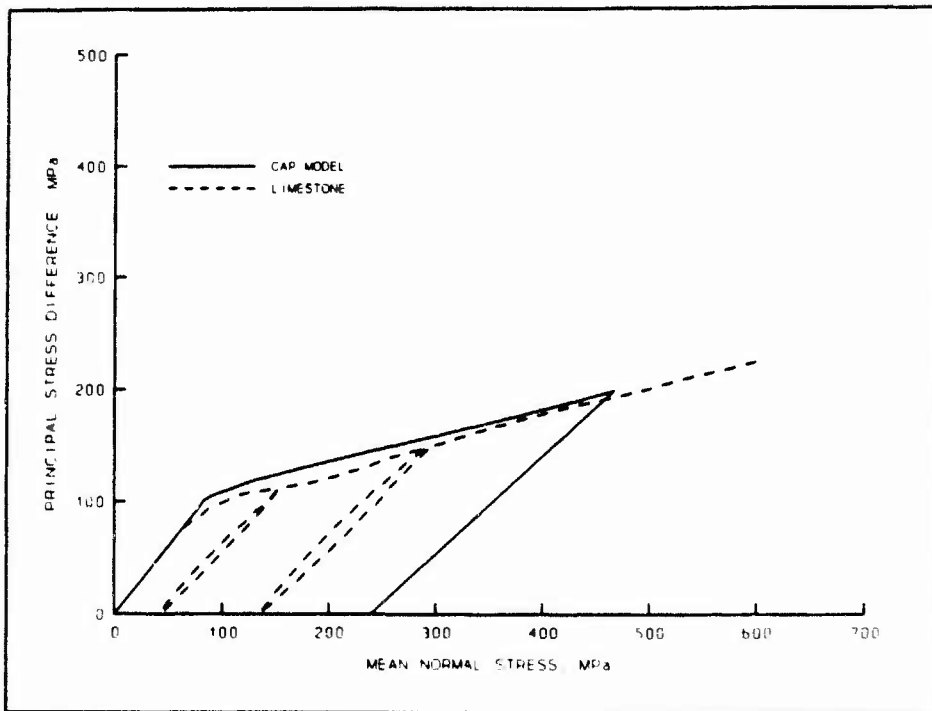


Figure 6.2. Drained K_0 stress path comparison

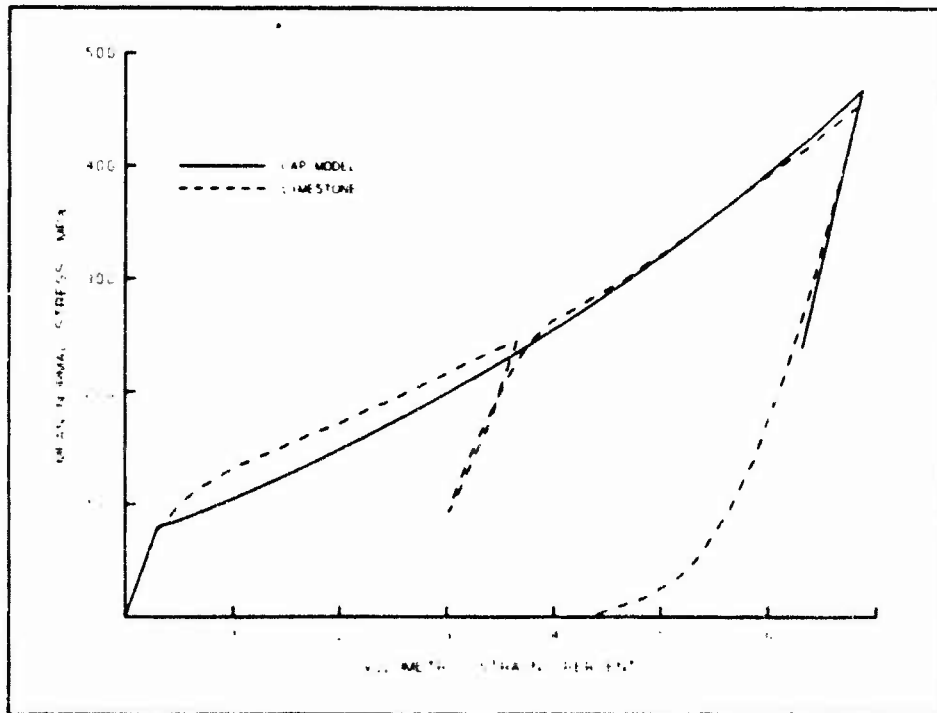


Figure 6.3. Drained K_0 pressure-volume comparison

vertical stress of approximately 150 MPa. A better match to the stress-strain behavior would require the K_0 stress path to break over at a higher value of principal stress difference. Higher fidelity was desired in the K_0 stress path.

In Figure 6.4, the calculated drained hydrostatic pressure-volume response of Salem limestone is compared to the recommended behavior. The quality of

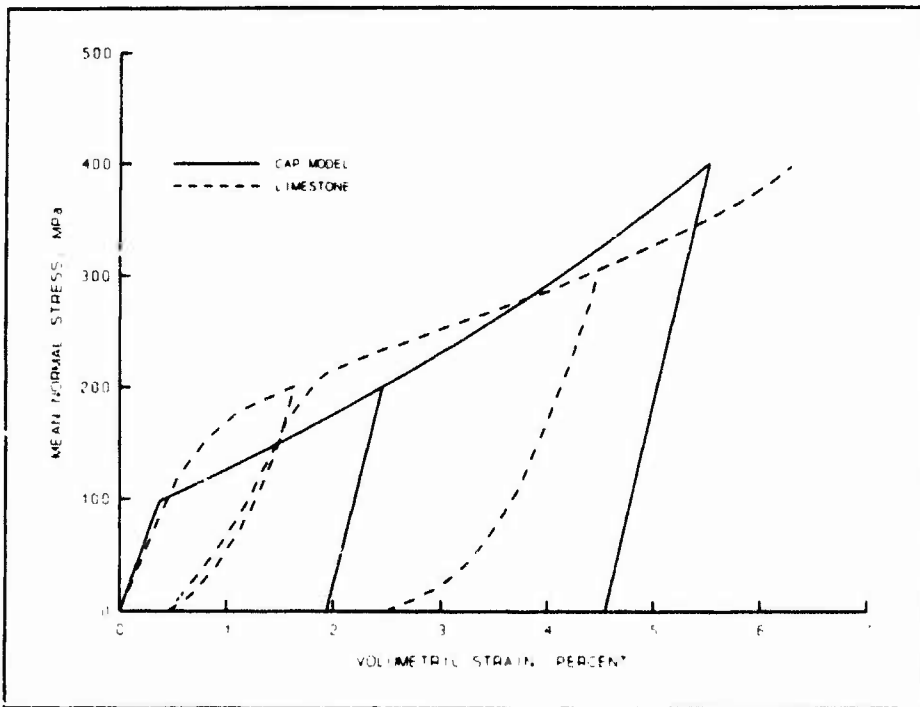


Figure 6.4. Drained hydrostatic load-unload comparison

the fit is not very good because greater emphasis was placed on fitting the K_0 behavior. Only a very complicated cap model, with several tens of fitting parameters, would fit both the hydrostatic and K_0 behavior of this material.

Drained triaxial compression (TXC) tests at confining pressures of 100 and 400 MPa were also simulated with the cap model. The calculated responses are plotted as principal stress difference versus axial strain and compared to actual test results in Figures 6.5 and 6.6. The quality of the fits is quite good considering the error introduced into the calculations by the lack of fidelity in the calculated hydrostatic pressure-volume response.

Undrained limestone simulations

The following single-element undrained simulations were performed using the Walker-Sternberg EOS for water and a carbonate EOS for the grain solids. The cap model fit to the recommended drained limestone properties modeled the skeletal behavior of the limestone.

An undrained K_0 test conducted on a fully-saturated specimen of Salem limestone was simulated with the FE code. The output is compared to the available recommended properties as another method of verifying the FE code. The calculated and recommended stress-strain responses are compared

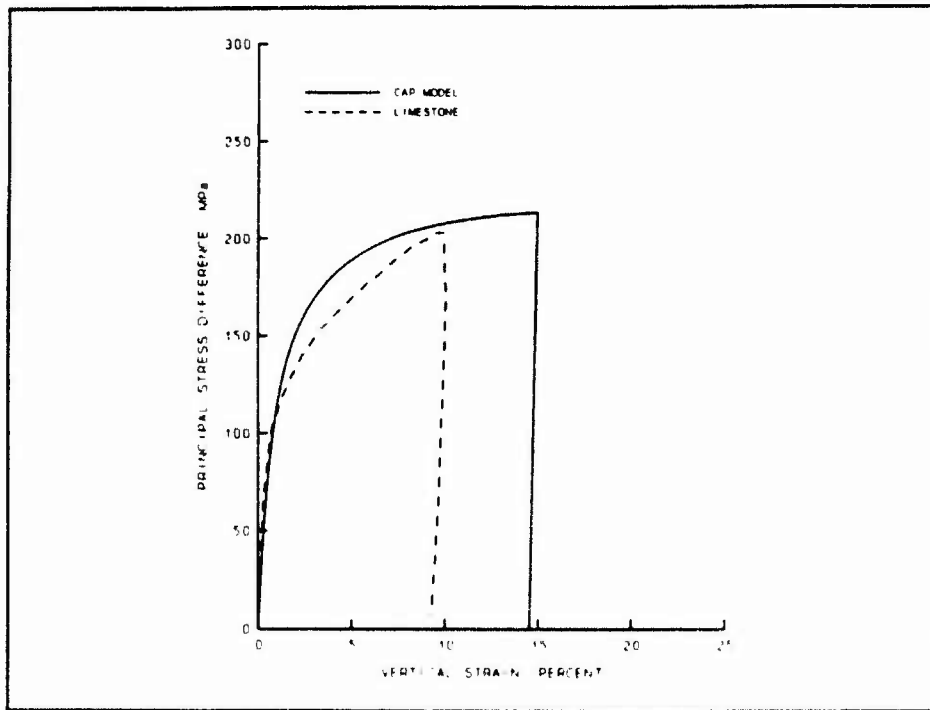


Figure 6.5. Drained TXC stress-strain comparison at 100 MPa confining pressure

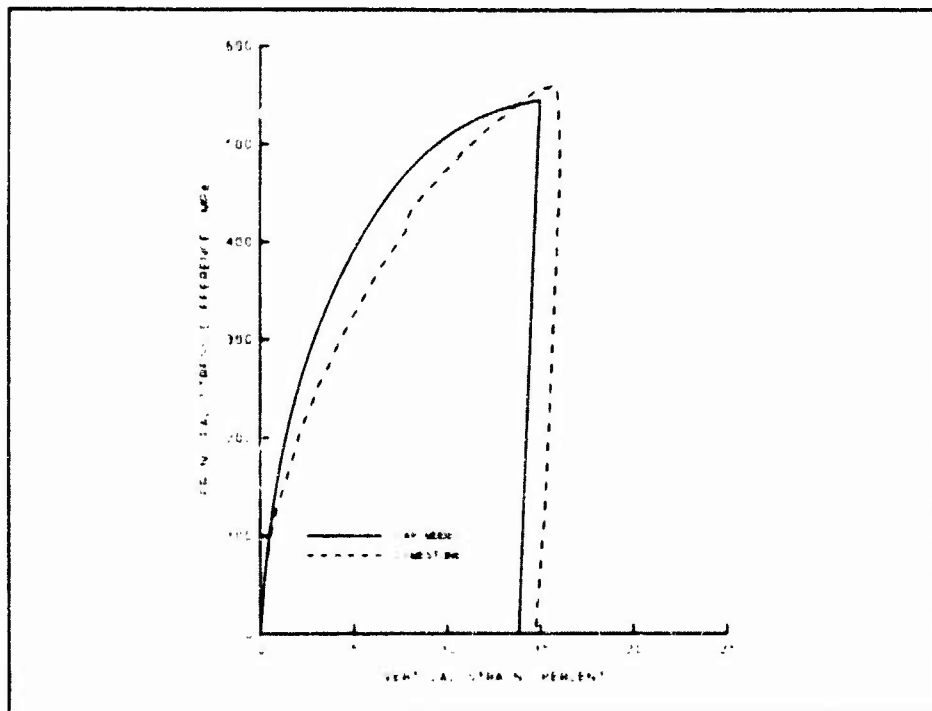


Figure 6.6. Drained TXC stress-strain comparison at 400 MPa confining pressure

in a plot of total vertical stress versus total vertical strain (Figure 6.7). The calculated undrained K_0 stress-strain response replicates the recommended

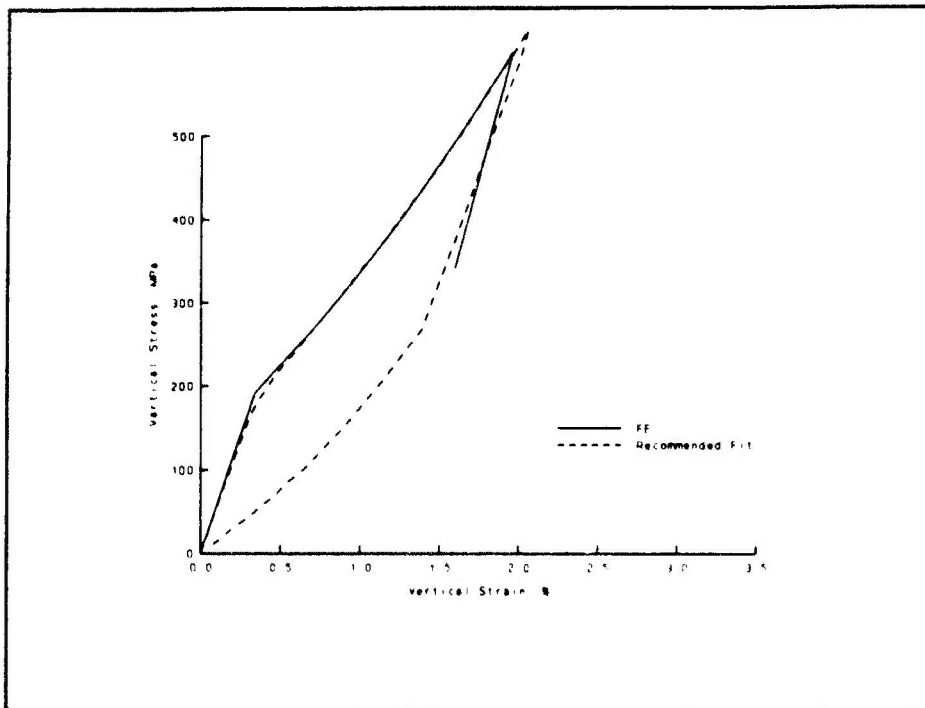


Figure 6.7. Undrained K_0 stress-strain comparison

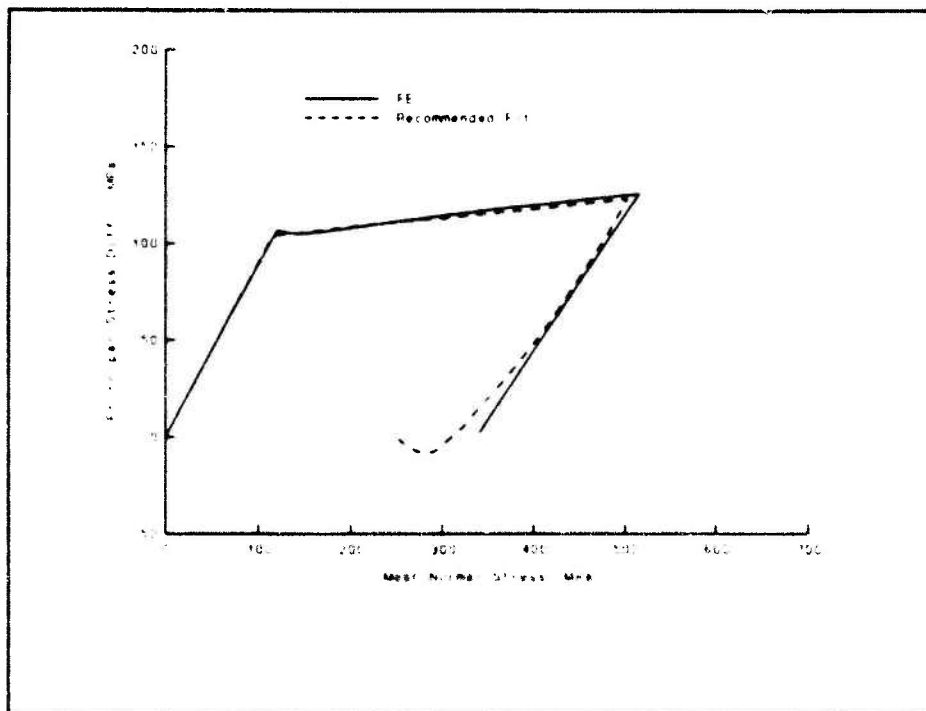


Figure 6.8. Undrained K_0 stress path comparison

stress-strain response perfectly during the loading phase, while the unloading is slightly stiffer. The calculated and recommended stress paths are compared in a plot of principal stress difference versus total mean normal stress

(Figure 6.8). The correlation between the calculated and the recommended stress paths is excellent.

The total (solid), effective (short dash) and pore fluid stresses (long dash) for the simulated undrained K_0 test are presented in Figure 6.9 in the format

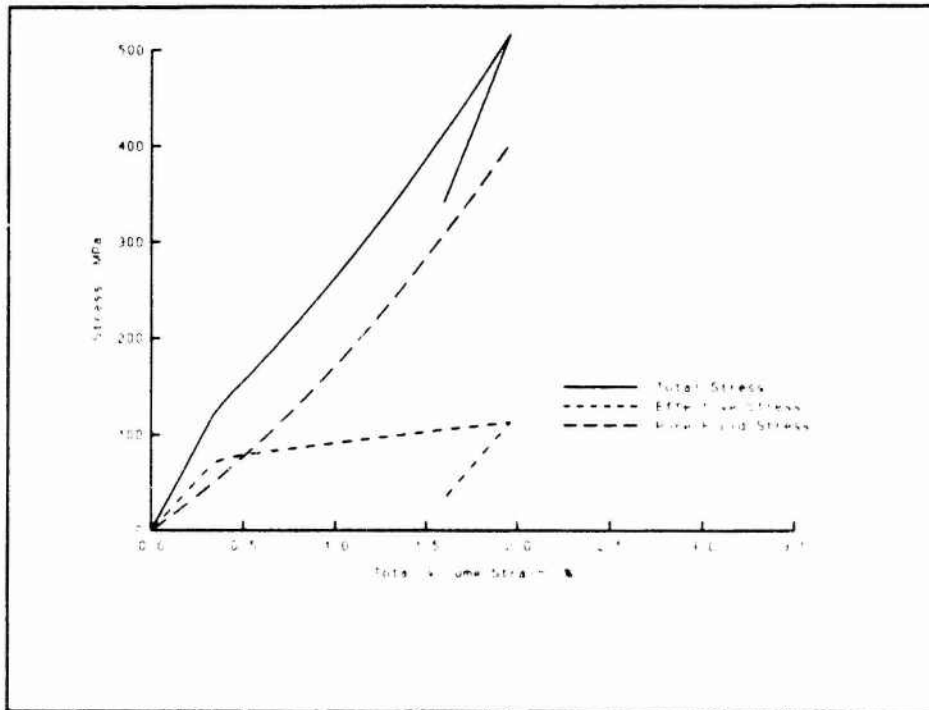


Figure 6.9. Stresses in a simulated undrained K_0 test

of stress versus total volume strain. This figure illustrates that, even in a competent rock such as limestone, a significant portion of the total applied stress is carried by the pore fluid, and the peak effective stress is only 20% of the peak total applied stress.

In "conventional" soil mechanics, water and the grain solids are often assumed to be incompressible. These assumptions have significant implications with regard to the response of materials during undrained loading. Under undrained or zero volume change boundary conditions, the undrained strength at failure and the undrained effective stress path are unique for a given material with prescribed initial conditions (Lambe and Whitman 1969). This means that the effective stress path is independent of the applied total stress path. A path of zero volume change in an elastic-plastic material implies that the elastic and plastic volume strains are of equal magnitude and opposite sign. To demonstrate that a unique effective stress path is developed, an undrained triaxial compression (TXC) test, i.e., constant radial stress during shear, and an undrained constant mean normal stress (CP) test, i.e., constant mean normal stress during shear, were numerically simulated. The following conditions existed prior to the undrained loading in both simulations: (1) the compressibilities of the water and the grain solids were zero;

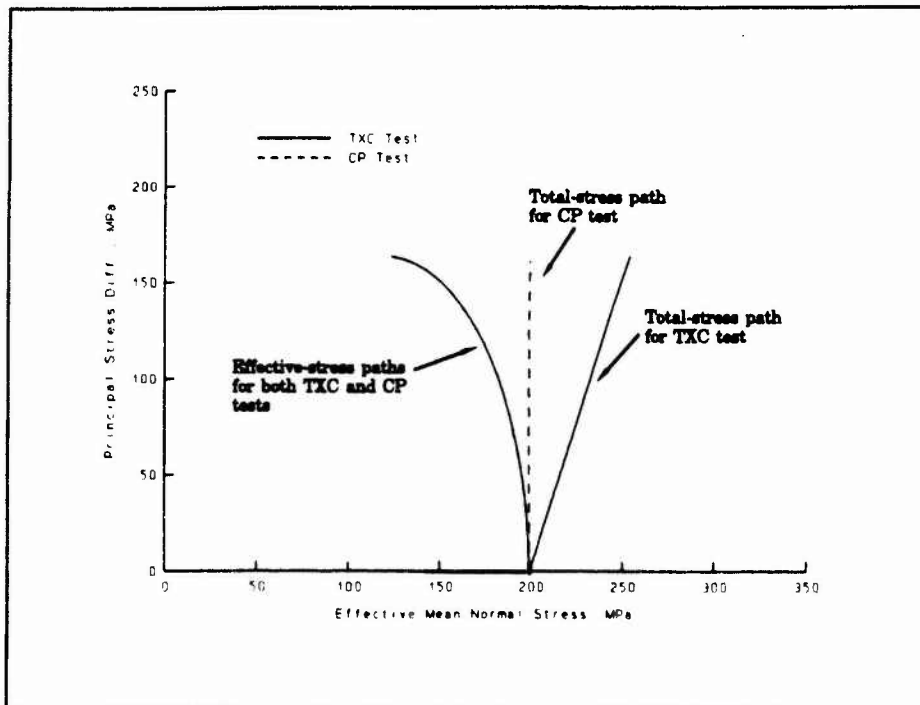


Figure 6.10. Total and effective stress paths from TXC and CP tests

(2) the nominal effective confining stress in the specimens was 200 MPa, which was generated by a drained hydrostatic loading; and (3) the initial pore fluid pressure was zero. The stresses during the shear loading were applied incrementally until the calculation would not converge under a convergence tolerance of 0.5 percent. The calculated total and effective stress paths for the TXC test (solid line) and the CP test (dashed line) are presented in Figure 6.10. The calculated effective stress paths from the TXC and CP tests are identical.

Additional undrained calculations were performed to prove that the undrained effective stress paths are not unique when the water and grain solids are compressible. Three undrained TXC tests with the following initial conditions were simulated: the nominal effective confining stress was 200 MPa and the applied back pressures (initial pore fluid pressures) were 0, 100, and 300 MPa. The calculated effective stress paths are presented in Figure 6.11. These calculations indicate that as the applied back pressure increased from 0 to 300 MPa, the corresponding effective stress paths moved to lower values of effective mean normal stress. This response can be explained with the following logic. As the water becomes stiffer with increasing levels of back pressure, equal strain increments within the specimen generate larger increments of pore fluid pressure. Thus, the effective stress paths move to the left in Figure 6.11.

The previous sections show that the FE code can accurately simulate both drained and undrained responses of Salem limestone under ideal laboratory test boundary condition. In the following sections, non-ideal boundary

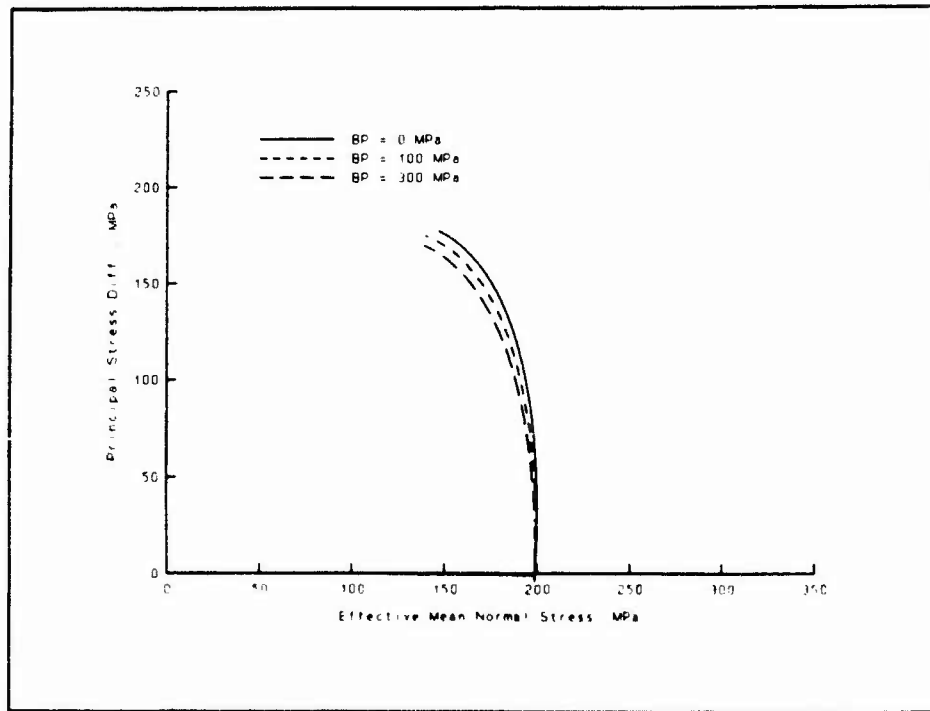


Figure 6.11. Effective stress paths from tests with different back pressures

conditions that actually exist in the laboratory tests will be simulated.

Test Specimen Simulations

FE grid

Cylindrical test specimens were simulated with the axisymmetric FE grid depicted in Figure 6.12. A quarter grid, consisting of 144 elements and 483 nodes, was used in the simulation due to the symmetric nature of the problem. The specimen end caps were included in the simulation to investigate the effects of end cap restraint upon both the stress and strain conditions within the test specimen. A worst case situation was simulated, i.e., one in which no sliding was permitted between the specimen and the steel end caps.

The simulated specimen is 11.43 cm (4.5 in.) in length with a diameter of 5.04 cm (2 in.). The permeability of the limestone was $1.03 \times 10^{-9} \text{ m}^2$, which is a value that insures a uniform pore pressure field throughout the mesh during both the drained and undrained simulations.

Simulation of drained triaxial compression test

A drained triaxial compression test at a confining stress of 200 MPa was simulated in the following manner. First, equal increments of vertical and

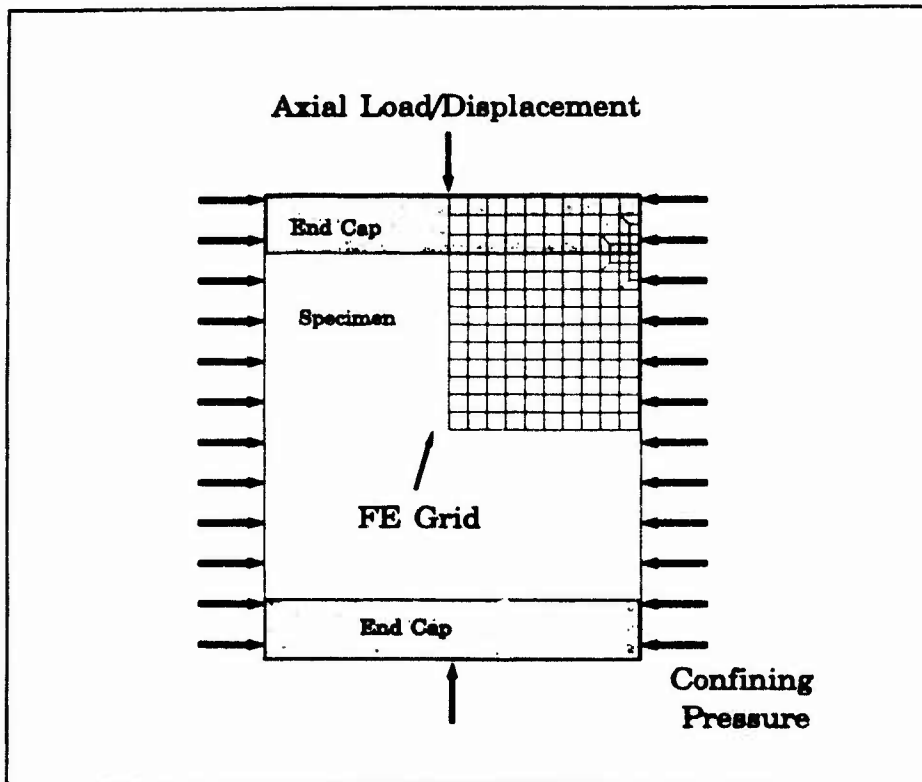


Figure 6.12. Finite element grid for specimen simulation

radial normal stresses were applied to the boundaries of the grid until the stresses equaled 200 MPa. Second, increments of vertical stress were applied until the total vertical stress reached 550 MPa. Finally, increments of vertical stress were removed until a hydrostatic state of total stress was obtained.

The output from this calculation is plotted in the form of contour plots of several stress or strain parameters, i.e., $\sqrt{J_{2D}}$, plastic volume strain, axial strain and radial strain (Figures 6.13 and 6.14). The contour plots present the state of stress or strain in the specimen at the time of peak total vertical stress (Note: the end cap is not included in these contour plots). With the exception of the upper 15 to 20 percent of the specimen, i.e., near the interface of the specimen and end cap, the state of stress within the specimen is relatively uniform (Figure 6.13). This is also true of the plastic volume strains within the specimen (Figure 6.13). However, both the axial and radial strains (Figure 6.14) exhibit significant gradients throughout the specimen. The smallest axial strains (0.03 m/m) are at the top of the specimen; the largest (0.20 m/m) develop at the center of the specimen. The

Table 6.1.
Laboratory Calculated Stress and Strain Values

Axial Strain	15.8%
Radial Strain	-6.2%
Principal Stress Difference	310 MPa
$\sqrt{J_{2D}}$	179 MPa

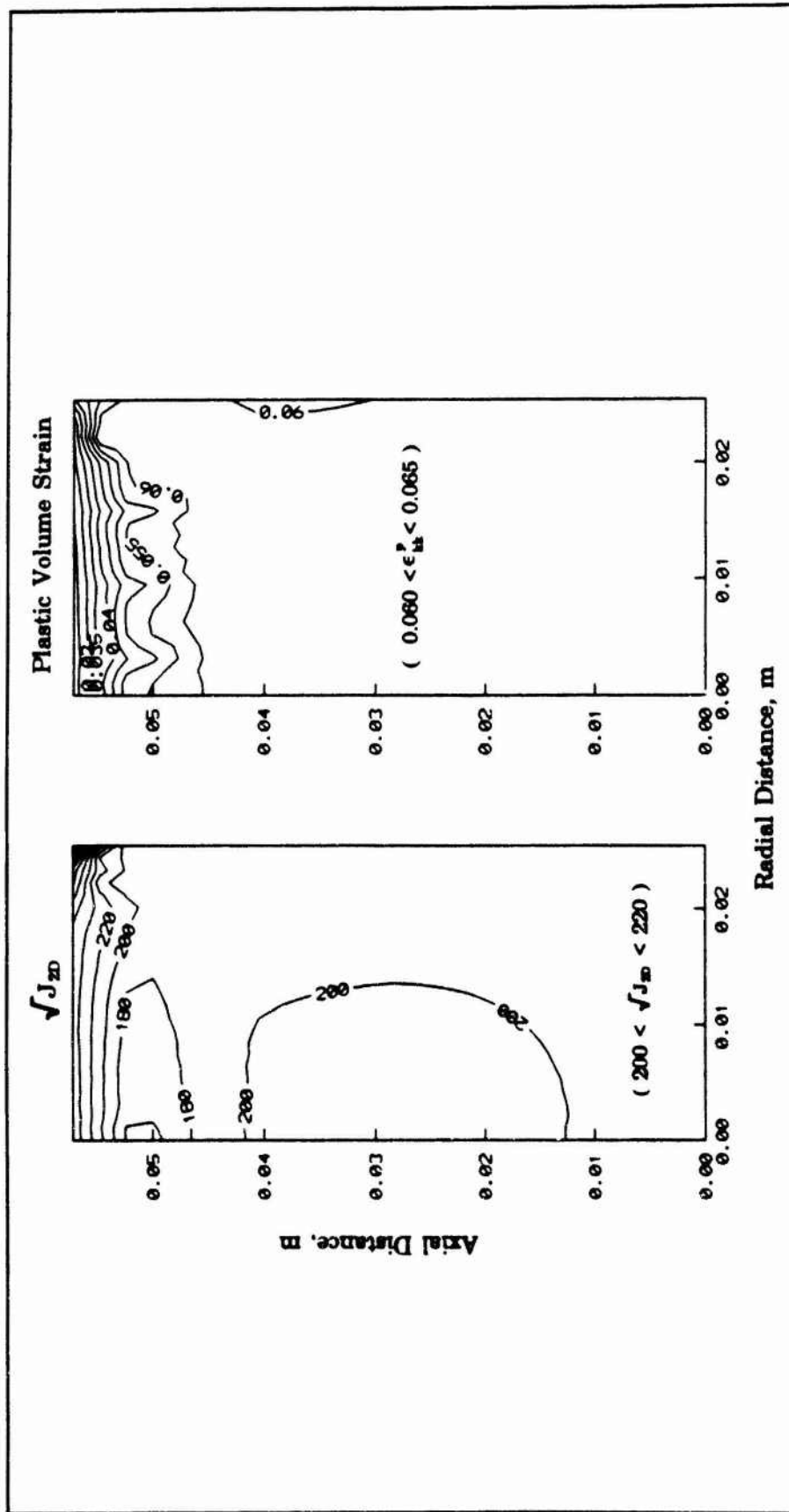


Figure 6.13. Contour plots of stress and plastic volume strain for a drained TXC test

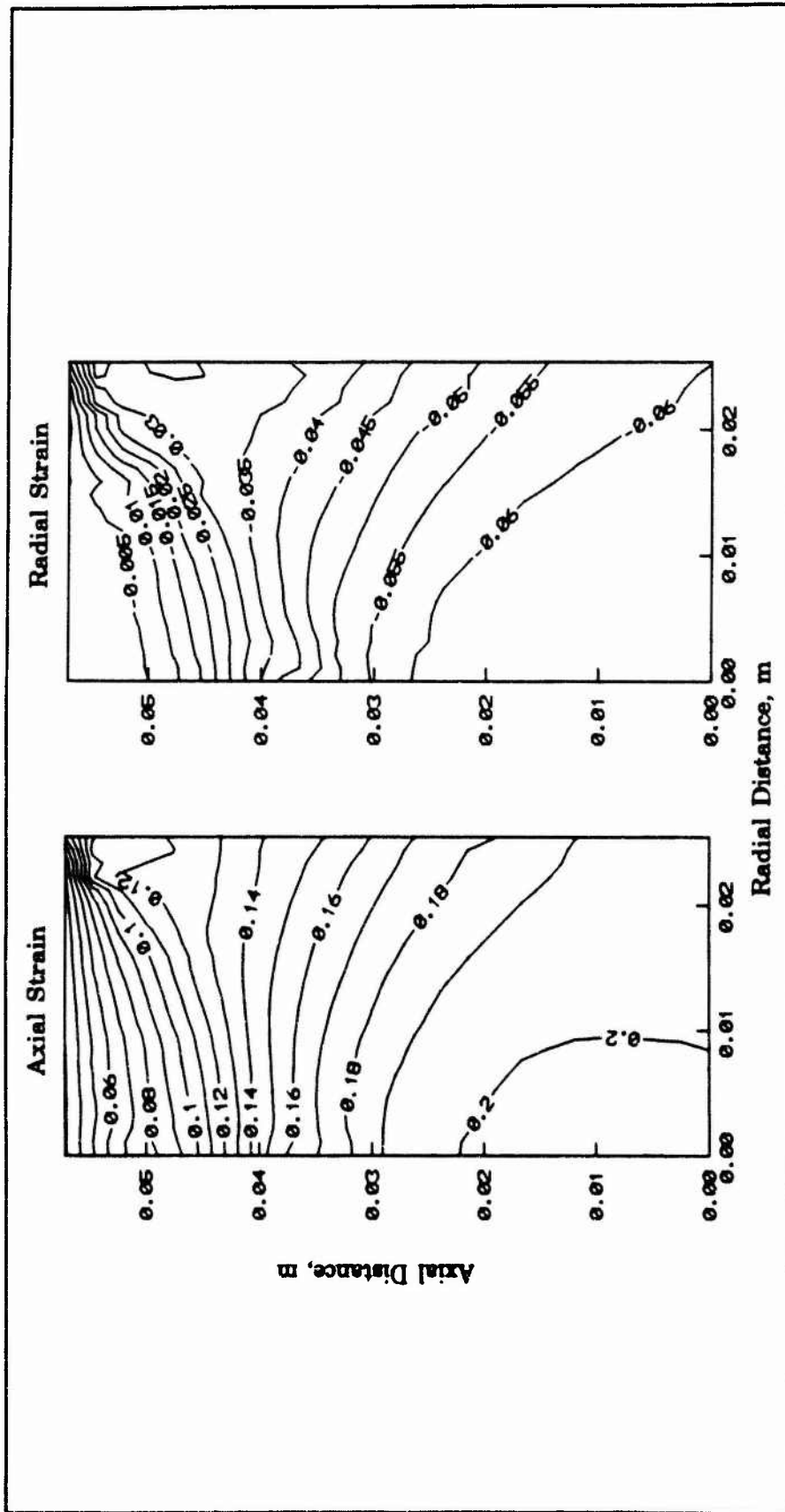


Figure 6.14. Contour plots of axial and radial strain for a drained TXC test

radial strains vary from approximately zero at the specimen-end cap interface to as much as -0.065 m/m at the center of the specimen.

Table 6.1 contains values of stress and strain that would be calculated from laboratory measured load and deformation measurements. Stresses, e.g., principal stress difference, were corrected for the changing cross-sectional area of the test specimen. The stress values underestimate the strength of the test specimen by approximately 5 percent, 179 MPa (from above table) versus 190 MPa (average stress throughout specimen). The axial strain of 15.8 percent represents only a small portion of the calculated axial strain within the test specimen, while the radial strain of -6.2 percent is representative of the radial strains in the central portion of the test specimen.

This calculation implies that the state of stress within the test specimen is not significantly effected by end cap restraints. Uniform stresses occur throughout major portions of the specimen. In contrast, large axial and radial strain gradients were developed in the test specimen. This implies that some type of end-cap lubrication should be used if uniform states of strain are desired.

Simulation of consolidated undrained triaxial compression test

A consolidated undrained triaxial compression test at a confining stress of 200 MPa was simulated with the FE code JAM. To begin the calculation, equal increments of vertical and radial normal stresses were applied to the boundaries of the grid until a hydrostatic stress of 200 MPa was achieved. During this hydrostatic loading, pore fluid was allowed to drain from the specimen. The boundary conditions were then changed so that no pore fluid could drain from the specimen. Finally, increments of vertical stress were applied until the solution would not converge, which implied that the specimen had failed. Failure occurred at a total axial strain of approximately 4.7 percent. A uniform pore fluid pressure existed throughout the specimen.

The output from this calculation is plotted in the form of contour plots of $\sqrt{J_{2D}}$, volume strain, axial strain, and radial strain (Figures 6.15 and 6.16). The contour plots present the state of stress or strain in the specimen at the time of specimen failure (Note: The end cap is again not included in these contour plots). The

Table 6.2. Laboratory Calculated Stress and Strain Values for Undrained TXC Test

$\sqrt{J_{2D}}$ contours (Figure 6.15) illustrate that a uniform state of stress exists within a majority of the test specimen; significant gradients only exist near the specimen-end cap interface. The same is true of the volume strain

Axial Strain	4.7%
Radial Strain	-0.4%
Volume Strain	3.8%
Principal Stress Difference	216 MPa
$\sqrt{J_{2D}}$	124 MPa

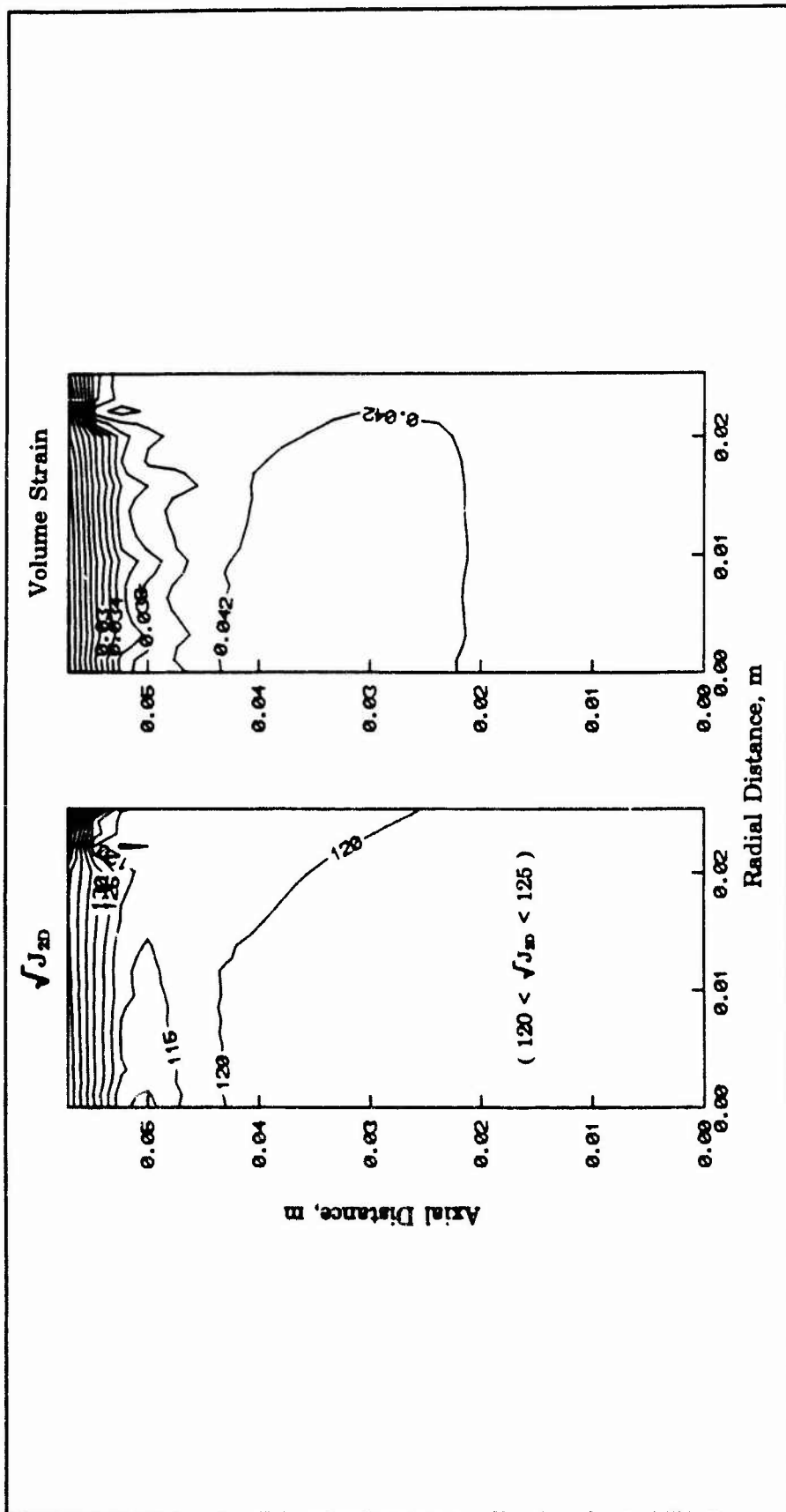


Figure 6.15. Contour plots of stress and volume strain

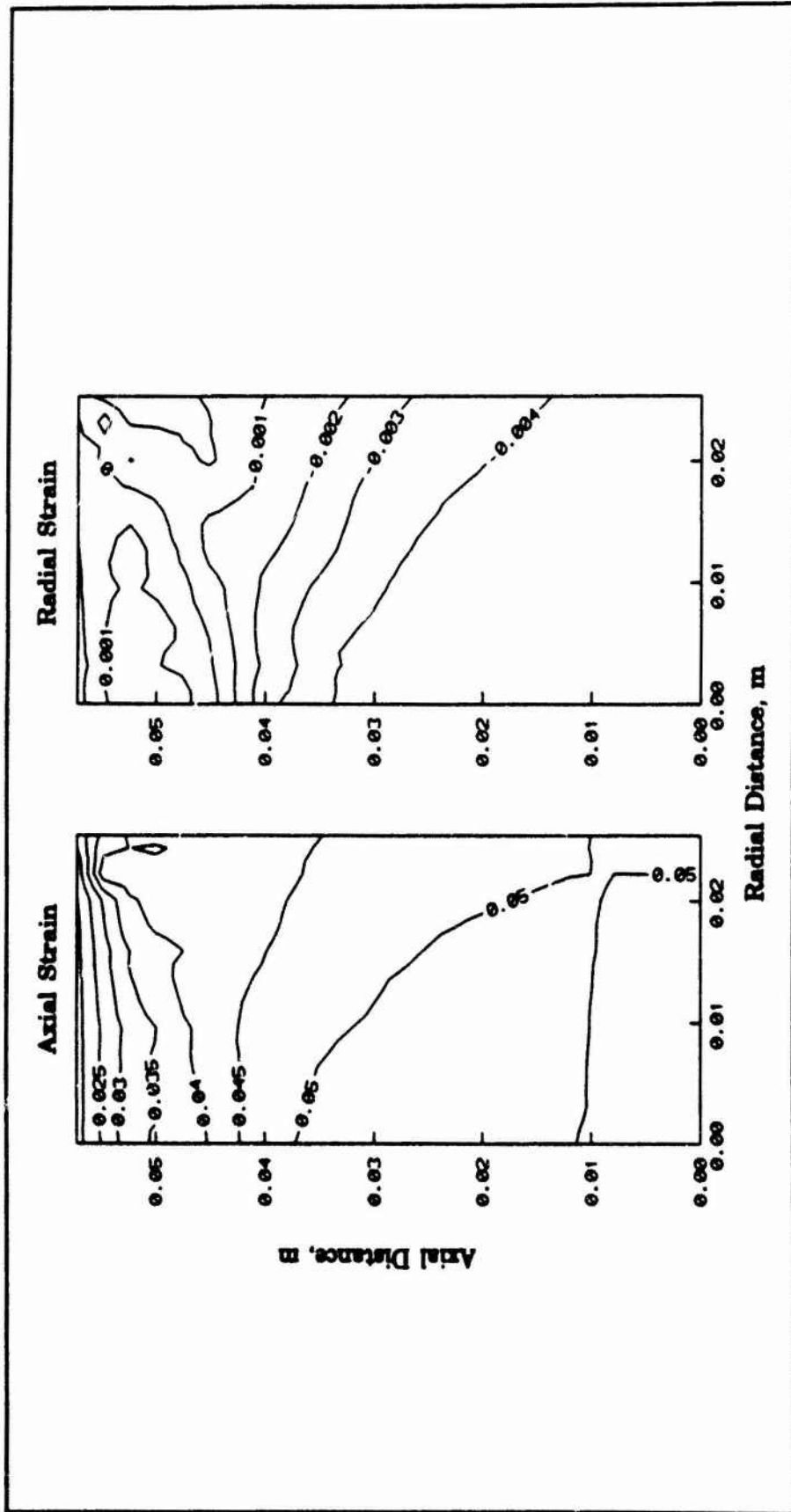


Figure 6.16. Contour plots of axial and radial strain

contours. The calculated volume strains indicate that the specimen was compacting. The calculated pore pressures confirm this observation, i.e., they increase continuously until specimen failure occurs. Due to the small axial strain level at which specimen failure occurs, significant gradients of axial and radial strain were not developed in the test specimen (Figure 6.16). Axial strains vary from 0.02 m/m at the top of the specimen to less than 0.055 m/m in the center of the specimen. Radial strains range from approximately zero at the specimen-end cap interface to -0.004 m/m at the center of the specimen.

Table 6.2 contains values of stress and strain that would be calculated from laboratory measured load and deformation measurements. As in the drained simulation, stresses were corrected for the changing cross-sectional area of the test specimen. The laboratory calculated stress values correspond with the values from the test specimen simulation, i.e., 124 MPa (from above table) versus 123 MPa (average stress throughout specimen). The laboratory calculated volume strain of 3.8 percent underestimates the simulated volume strains that vary between 4 and 4.4 percent throughout most of the test specimen. The axial strain of 4.7 percent agrees with the calculated axial strain throughout a major portion of the test specimen. The radial strain of -0.4% is representative of the simulated radial strains in the central portion of the test specimen.

This calculation demonstrates that significant stress and strain gradients are not developed in the limestone when the specimen fails at small axial strains, despite the introduction of end cap restraint. In addition, the stresses and strains calculated from laboratory measurements correlate well with the actual stress and strain states within the test specimen.

Summary

Numerical simulations of limestone behavior under drained and undrained boundary conditions were presented in this chapter. The ability of the 14-parameter cap model to simulate the drained behavior of the limestone was demonstrated by comparing calculated responses of hydrostatic, uniaxial strain, and triaxial compression loadings with measured or recommended limestone responses. The ability of the FE code to calculate the undrained behavior of the limestone was demonstrated by comparing calculated responses of uniaxial strain loadings with recommended limestone responses. Finally, both drained and undrained TXC test simulations were documented which demonstrate the utility of the FE code in analyzing laboratory test specimen conditions.

7 Summary

This report documents the features and algorithms implemented into the FE code JAM. The FE code JAM is a numerical tool with the capability to:

- calculate strains, total and effective stresses, and pore fluid pressures for fully- and partially-saturated porous media,
- calculate the time dependent flow of pore fluids in porous media,
- model nonlinear irreversible stress-strain behavior, including coupled shear-induced volume change, and
- simulate the effect of nonlinear pore fluid compressibility and the contribution of the compressibility of the grain solids for stresses up to several hundred megapascals.

In this report, the FE model implemented into JAM was described, and equations were developed for the residual forces. The features of the cap model and the relevant equations were documented, and the steps required to implement the cap model into the FE code were summarized. Other constitutive models available in the code were also reviewed.

The equations of state for air, water, and the grain solids were documented, and the equations for the compressibility of an air-water mixture were developed. Several documented verification problems demonstrated that the program works correctly. These problems included one- and two-dimensional consolidation problems, Cryer's problem of a consolidating sphere of soil, and a thick-walled cylinder problem.

Numerical simulations of limestone behavior under drained and undrained boundary conditions were presented. A 14-parameter cap model modelled the skeletal properties of the limestone. Single element calculations demonstrated the ability of the FE code to simulate both the drained and undrained responses of the limestone under several different load and unload boundary conditions. The utility of the FE code was demonstrated by the simulation of drained and undrained triaxial compression tests, and the influence end cap restraint had on the stress and strain states in the test specimen.

References

- Alonso, E.E., and Lloret, A. (1982). "Behavior of partially saturated soil in undrained loading and step by step embankment construction." *IUTAM Conference on Deformation and Failure of Granular Materials*.
- Baladi, G.Y. (1978). "An elastic-plastic constitutive relation for transverse-isotropic three-phase earth materials," Miscellaneous Paper S-78-14, U.S. Army Engineer Waterways Experiment Station, Vicksburg, MS.
- Baladi, G.Y. (1979). "An effective stress model for ground motion calculations," Technical Report SL-79-7, U.S. Army Engineer Waterways Experiment Station, Vicksburg, MS.
- Baladi, G.Y. (1986). "Development of a theoretically sound cap model for fitting ISST-type material behavior," Technical Report SL-86-34, U.S. Army Engineer Waterways Experiment Station, Vicksburg, MS.
- Baladi, G.Y., and Akers, S.A. (1981). "Constitutive properties and material model development for marine sediments in support of the Subseabed Disposal Program," Annual Progress Report, January to December 1980, to the Department of Energy, U.S. Army Engineer Waterways Experiment Station, Vicksburg, MS.
- Baladi, G.Y., and Rohani, B. (1977). "Liquefaction potential of dams and foundations: Report 3, Development of an elastic-plastic constitutive relationship for saturated sand," Research Report S-76-2, U.S. Army Engineer Waterways Experiment Station, Vicksburg, MS.
- Baladi, G.Y., and Rohani, B. (1978). "Liquefaction potential of dams and foundations: Report 5, Development of a constitutive relationship for simulating the response of saturated cohesionless soil," Research Report S-76-2, U.S. Army Engineer Waterways Experiment Station, Vicksburg, MS.
- Baladi, G.Y., and Rohani, B. (1979). "Elastic-plastic model for saturated sand," *ASCE, Journal of the Geotechnical Engineering Division* 105(4), 465-480.

- Baladi, G.Y., and Rohani, B. (1982). "An elastic-viscoplastic constitutive model for earth materials." Technical Report SL-82-10, U.S. Army Engineer Waterways Experiment Station, Vicksburg, MS.
- Bathe, K-J. (1982). *Finite element procedures in engineering analysis*. Prentice-Hall, Englewood Cliffs, NJ.
- Biot, M.A., and Willis, D.G. (1957). "The elastic coefficients of the theory of consolidation," *Journal of Applied Mechanics* 24.
- Biot, M.A. (1941). "General theory of three-dimensional consolidation," *Journal of Applied Physics* 12.
- Biot, M.A. (1955). "Theory of elasticity and consolidation for a porous anisotropic solid," *Journal of Applied Physics* 26(2).
- Biot, M.A. (1962). "Mechanics of deformation and acoustic propagation in porous media," *Journal of Applied Physics* 33(4).
- Biot, M.A. (1963). "Theory of stability and consolidation of a porous medium under initial stress," *Journal of Mathematics and Mechanics* 12(4).
- Bishop, A.W. (1973). "The influence of an undrained change in stress on the pore pressure in porous media of low compressibility," *Geotechnique* 23(3).
- Bishop, A.W., and Eldin, G. (1950). "Undrained triaxial tests on saturated sands and their significance in the general theory of shear strength," *Geotechnique* 2(1).
- Blouin, S., and Chitty, D. (1988a). "Strength and deformation properties of Salem limestone," viewgraph briefing, DNA HTK Materials Testing Meeting, 19 July 1988, Applied Research Associates, Inc., South Royalton, VT.
- Blouin, S., and Chitty, D. (1988b). "Project summary: strength and deformation properties of Salem limestone," viewgraph briefing, DNA Materials Modeling Meeting, 16 November 1988, Applied Research Associates, Inc., South Royalton, VT.
- Chang, C.S., and Durcan, J.M. (1977). "Analysis of consolidation of earth and rockfill dams; Main text and Appendices A and B," Contract Report S-77-4, U.S. Army Engineer Waterways Experiment Station, Vicksburg, MS.
- Chang, C.S., and Duncan, J.M. (1983). "Consolidation analysis for partly saturated clay by using an elastic-plastic effective stress-strain model," *International Journal For Numerical and Analytical Methods In Geomechanics* 7.

- Chen, W.F., and Baladi, G.Y. (1985). *Soil plasticity: theory and implementation*. Elsevier Science Publishing Co., New York.
- CRC Handbook of Chemistry and Physics. (1980). R.C. Weast, ed., 60th ed., CRC Press, Inc., Boca Raton, Florida.
- Cryer, C. W. (1963). "A comparison of the three-dimensional consolidation theories of Biot and Terzaghi," *Quarterly Journal of Mechanics and Applied Mathematics*, 16(3), 401-412.
- DiMaggio, F.L., and Sandler, I. (1971). "Material model for granular soils," *ASCE, Journal of the Engineering Mechanics Division*, 97(3).
- Drucker, D.C. (1951). "A more fundamental approach to plastic stress-strain relations." *ASME, Proc. First US National Congress of Applied Mechanics*.
- Drucker, D.C. (1950). "Some implications of work hardening and ideal plasticity," *Quarterly Journal of Applied Mathematics* 7(4).
- Fredlund, D.G. (1976). "Density and compressibility characteristics of air-water mixtures," *Canadian Geotechnical Journal* 13(4).
- Ghaboussi, J., and Wilson, E.L. (1972). "Variational formulation of dynamics of fluid-saturated porous elastic solids," *ASCE, Journal of the Engineering Mechanics Division* 98(4).
- Ghaboussi, J., and Wilson, E.L. (1973). "Flow of compressible fluid in porous elastic media," *International Journal for Numerical Methods in Engineering* 5.
- Gibson, R.E., Knight, K., and Taylor, P.W. (1963). "A critical experiment to examine theories of three-dimensional consolidation." *European Conference on Soil Mechanics and Foundation Engineering, Wiesbaden* 1.
- Hibbitt, Karlsson and Sorensen (1989). *ABAQUS: Verification manual, version 4.8*, Pawtucket, RI.
- Hinton, E., and Campbell, J.S. (1974). "Local and global smoothing of discontinuous finite element functions using a least squares method," *International Journal for Numerical Methods in Engineering* 8.
- Hinton, E., Scott, F.C., and Ricketts, R.E. (1975). "Local least squares stress smoothing for parabolic isoparametric elements," *International Journal for Numerical Methods in Engineering* 9.
- Hodge, P.G., and White, G.N. (1950). "A quantitative comparison of flow and deformation theories of plasticity," *Journal of Applied Mechanics* 17(2).

- Lambe, T.W., and Whitman, R.V. (1969). *Soil Mechanics*. John Wiley & Sons, New York.
- Lewis, R.W., Roberts, G.K., and Zienkiewicz, O.C. (1976). "A non-linear flow and deformation analysis of consolidated problems," *Numerical Methods In Geomechanics 2*, 1106-1118.
- Lewis, R.W., and Schrefler, B.A. (1987). *The finite element method in the deformation and consolidation of porous media*. John Wiley & Sons, Chichester.
- Meier, R. W. (1986). "Results of plane one-dimensional ground shock calculations for a baseline clay/clay shale geology," Technical Report SL-86-22, U.S. Army Engineer Waterways Experiment Station, Vicksburg, MS.
- Meier, R. W. (1989). "Cap model notes," Personal communication.
- Oka, F., Adachi, T., and Okano, Y. (1986). "Two-dimensional consolidation analysis using an elasto-viscoplastic constitutive equation," *International Journal for Numerical and Analytical Methods in Geomechanics 10*, 1-16.
- Owen, D.R.J., and Hinton, E. (1980). *Finite elements in plasticity: theory and practice*. Pineridge Press Limited, Swansea, U.K.
- Prager, W., and Hodge, P.G. (1951). "Plane strain: problems with axial symmetry." *Theory of perfectly plastic solids*. John Wiley & Sons, New York, 95-103.
- Rohani, B. (1977). "Mechanical constitutive models for engineering materials," Technical Report S-77-19, U.S. Army Engineer Waterways Experiment Station, Vicksburg, MS.
- Rubin, D., and Sandler, I. (1977). "Development of a high pressure cap model for use in computations of ground shock from subsurface explosions," Contract Report S-77-2, U.S. Army Engineer Waterways Experiment Station, Vicksburg, MS.
- Sandhu, R.S., and Wilson, E.L. (1969). "Finite-element analysis of seepage in elastic media," *ASCE, Journal of the Engineering Mechanics Division 95*(3), 641-652.
- Sandler, I., DiMaggio, F.L., and Baladi, G.Y. (1976). "Generalized cap model for geologic materials," *ASCE, Journal of the Geotechnical Engineering Division 102*(7), 683-699.
- Sandler, I., and Rubin, D. (1979). "An algorithm and a modular subroutine for the cap model," *International Journal of Numerical and Analytical Methods in Geomechanics 3*, 173-186.

- Schuurman, I.E. (1966). "The compressibility of an air/water mixture and a theoretical relation between the air and water pressures," *Geotechnique* 16(4).
- Simon, B.R., Wu, J.S.-S., and Zienkiewicz, O.C. (1986a). "Evaluation of u-w and u- π finite element methods for the dynamic response of saturated porous media using one-dimension," *International Journal for Numerical and Analytical Methods in Geomechanics* 10, 461-482.
- Simon, B.R., Wu, J.S.-S., and Zienkiewicz, O.C. (1986b). "Evaluation of higher order mixed and hermitean finite element procedures for dynamic analysis of saturated porous media," *International Journal* 10, 483-499.
- Skempton, A.W. (1960). "Effective stress in soils, concrete, and rocks." *Proceedings of Conference on Pore Pressure and Suction in Soils*. Butterworth, London, 4-16.
- Walker, W.A., and Sternberg, H.M. (1965). "The Chapman-Jouguet isentropic and the underwater shockwave performance of pentolite." *Proceedings Fourth Symposium on Detonation*. U.S. Naval Ordnance Laboratory, White Oak, Maryland, 27-38.
- Zelasko, J.S. (1991). "Total-stress material properties for 13.5-percent-porous limestone," Memorandum dated 21 May 1991, U.S. Army Engineer Waterways Experiment Station, Vicksburg, MS.
- Zienkiewicz, O.C. (1985a). "Transient analysis - some recent developments." *Proc. of the Intl. Conference on Numerical Methods in Engineering: Theory and Applications* 1, 3-8.
- Zienkiewicz, O.C. (1985b). "The coupled problems of soil-pore fluid-external fluid interaction basis for a general geomechanics code." *Fifth International Conference On Numerical Methods In Geomechanics*.
- Zienkiewicz, O.C., Chang, C.T., and Bettess, P. (1980). "Drained, undrained, consolidating and dynamic behavior assumptions in soils," *Geotechnique* 30(4), 385-395.
- Zienkiewicz, O.C., Leung, K.H., Hinton, E., and Chang, C.T. (1982). "Liquefaction and permanent deformation under dynamic conditions - numerical solution and constitutive relations" *Soil mechanics - transient and cyclic loads*. John Wiley & Sons Ltd., Chichester, 71-103.
- Zienkiewicz, O.C., and Shiomi, T. (1984). "Dynamic behavior of saturated porous media; the generalized Biot formulation and its numerical solution," *International Journal for Numerical and Analytical Methods in Geomechanics* 8, 71-96.

DISTRIBUTION LIST

DEPARTMENT OF DEFENSE

Director
Defense Nuclear Agency
ATTN: SPWE (Dr. E. L. Tremba)
Technical Library
6801 Telegraph Road
Alexandria, VA 22310-3398

Director
Defense Nuclear Agency
New Mexico Operations Office
ATTN: FCT (Mr. J. W. LaComb)
FALS (Dr. G. Y. Baladi)
FCIP (Dr. E. J. Rinehart)
FCTP (Ms. Audrey Martinez)
FCTT (Dr. B. L. Ristvet)
1680 Texas St., SE
Kirtland AFB, NM 87117-5669

Director
Advanced Research Project Agency
ATTN: Library
3701 N. Fairfax Drive
Arlington, VA 22203-1714

Defense Technical Information Center
ATTN: TC (2 cys)
Cameron Station
Alexandria, VA 22314

DEPARTMENT OF THE ARMY

Commander
US Army Corps of Engineers
ATTN: CEIM-SL (2 cys)
Washington, DC 20314-1000

Commander & Director
US Army Construction Engineering Research
Laboratory
ATTN: Technical Library
P.O. Box 9005
Champaign, IL 61826-9005

Commander
US Army Engineer District, Omaha
ATTN: CEMRO-ED-SH (Mr. Bruce Walton)
215 North 17th Street
Omaha, NE 68102-4978

DEPARTMENT OF THE ARMY (CONTINUED)

Director
US Army Cold Regions Research and
Engineering Laboratory
ATTN: Technical Library
72 Lyme Road
Hanover, NH 03755-1290

Commander
US Army Research Laboratory
ATTN: Technical Library
2800 Powder Mill Road
Adelphi, MD 20783-1145

Director
US Army Research Office
ATTN: SLCRO-IP-L (Ms. Brenda Mann)
P.O. Box 12211
Research Triangle Park, NC 27709-2211

DEPARTMENT OF THE NAVY

Naval Civil Engineering Laboratory
ATTN: Technical Library
560 Laboratory Drive
Port Hueneme, CA 93043-4328

Naval Facilities Engineering Command
200 Stovall Street
ATTN: Technical Library
Alexandria, VA 22332-2300

DEPARTMENT OF THE AIR FORCE

Air Force Office of Scientific Research
ATTN: Technical Library
Bolling AFB, DC 20332

Phillips Laboratory
ATTN: Technical Library
Kirtland AFB, NH 87117-6008

Wright Laboratory
Airbase Survivability Branch
ATTN: Technical Library
139 Barnes Drive, Suite 2
Tyndall AFB, FL 32403-5323

DEPARTMENT OF THE AIR FORCE (CONTINUED)

Commander
Wright Laboratory
Armament Directorate
ATTN: Technical Library
101 W. Eglin Blvd., Ste 251
Eglin AFB, FL 32542-6810

DEPARTMENT OF ENERGY

Lawrence Livermore National Laboratory
ATTN: L-200 (Dr. John Rambo)
P.O. Box 808
Livermore, CA 94550-0622

Los Alamos National Laboratory
ATTN: M/S F659 (Dr. Fred App)
P.O. Box 1663
Los Alamos, NM 87545

Sandia National Laboratories
ATTN: Dept 9311 (Dr. Al Chabai)
Dept 9311 (Mr. Carl Smith)
Dept 9311 (Dr. R.C. Bass)
P.O. Box 5800
Albuquerque, NM 87185-5800

DEPARTMENT OF DEFENSE CONTRACTORS

Mr. S. E. Blouin
Applied Research Associates, Inc.
Box 120A, Waterman Road
South Royalton, VT 05068

Dr. Dusan Krajcinovic
Mechanical and Aerospace Engineering
Arizona State University
Tempe, AZ 85287-6106

Mr. K. N. Kreyenhagen
Mr. H. D. Zimmerman
California Research & Technology Division
The Titan Corporation
20943 Devonshire Street
Chatsworth, CA 91311-2376

Dr. I. S. Sandler
Weidlinger Associates
333 Seventh Avenue
New York, NY 10001

DEPARTMENT OF DEFENSE CONTRACTORS (CONT.)

Dr. Poul V. Lade
School of Engineering and Applied Science
University of California
Los Angeles, CA 90024

Dr. Wayne A. Charlie
Department of Civil Engineering
Colorado State University
Ft. Collins, CO 80523

Dr. J. G. Jackson, Jr.
5024 Nailor Road
Vicksburg, MS 39180

Dr. Martin Ostoja-Starzewski
Department of Metallurgy, Mechanics and
Materials Science
Michigan State University
East Lansing, MI 48824-1226

Dr. J. W. Ju
Department of Civil Engineering and
Operations Research
Princeton University
Princeton, NJ 08544

Dr. D. F. Patch
Science Applications International
Corporation
10260 Campus Pt. Dr., M/S C2
San Diego, CA 92121

Dr. Norton Rimer
S-CUBED
A Division of Maxwell Labs, Inc.
P.O. Box 1620
La Jolla, CA 92038-1620

Dr. G. Wayne Clough
Dr. J. Michael Duncan
Dr. Tom L. Brandon
Dr. T. Kuppusamy
Dept. of Civil Engineering
Patton Hall
Virginia Tech
Blacksburg, VA 24061

REPORT DOCUMENTATION PAGE

Form Approved
OMB No. 0704-0188

Public reporting burden for this collection of information is estimated to average 1 hour per response, including the time for reviewing instructions, searching existing data sources, gathering and maintaining the data needed, and completing and reviewing the collection of information. Send comments regarding this burden estimate or any other aspect of this collection of information, including suggestions for reducing this burden, to Washington Headquarters Services, Directorate for Information Operations and Reports, 1215 Jefferson Davis Highway, Suite 1204, Arlington, VA 22202-4304, and to the Office of Management and Budget, Paperwork Reduction Project (0704-0188), Washington, DC 20503

1. AGENCY USE ONLY (Leave blank)	2. REPORT DATE September 1993	3. REPORT TYPE AND DATES COVERED Final Report
----------------------------------	----------------------------------	--

4. TITLE AND SUBTITLE Two-Dimensional Finite Element Analysis of Porous Media at Multikilobar Stress Levels	5. FUNDING NUMBERS
--	--------------------

6. AUTHOR(S) Stephen A. Akers	
----------------------------------	--

7. PERFORMING ORGANIZATION NAME(S) AND ADDRESS(ES) U.S. Army Engineer Waterways Experiment Station Structures Laboratory 3909 Halls Ferry Road Vicksburg, MS 39180-6199	8. PERFORMING ORGANIZATION REPORT NUMBER Technical Report SL-93-16
---	--

9. SPONSORING/MONITORING AGENCY NAME(S) AND ADDRESS(ES) Laboratory Discretionary Research and Development Program Assistant Secretary of the Army (R&D) Washington, DC 20315	10. SPONSORING/MONITORING AGENCY REPORT NUMBER
---	--

11. SUPPLEMENTARY NOTES

12a. DISTRIBUTION/AVAILABILITY STATEMENT Approved for Public Release; Distribution is Unlimited	12b. DISTRIBUTION CODE
--	------------------------

13. ABSTRACT (Maximum 200 words)

A finite element (FE) code was developed to verify laboratory test results or to predict unavailable laboratory test data for porous media loaded to multikilobar stress levels. The FE code simulates quasi-static, axisymmetric, laboratory mechanical property tests, i.e., the laboratory tests are analyzed as boundary value problems. The code calculates strains, total and effective stresses, and pore fluid pressures for fully and partially saturated porous media. The time-dependent flow of the pore fluid is also calculated. An elastic-plastic strain-hardening cap model calculates the time-independent skeletal responses of the porous solids. This enables the code to model nonlinear irreversible stress-strain behavior and shear-induced volume changes. Fluid and solid compressibilities were incorporated into the code, and partially saturated materials were simulated with a "homogenized" compressible pore fluid. Solutions for several verification problems are given as proof that the program works correctly, and numerical simulations of limestone behavior under drained and undrained boundary conditions are also presented.

14. SUBJECT TERMS Cap model Finite element	Compressibility Limestone	Effective stress Porous media	15. NUMBER OF PAGES 105
			16. PRICE CODE

17. SECURITY CLASSIFICATION OF REPORT UNCLASSIFIED	18. SECURITY CLASSIFICATION OF THIS PAGE UNCLASSIFIED	19. SECURITY CLASSIFICATION OF ABSTRACT UNCLASSIFIED	20. LIMITATION OF ABSTRACT
---	--	---	----------------------------